Generation of immune responses within lymph nodes during type-I inflammation

Jessica Huang

A dissertation submitted in partial fulfillment of the
requirements for the degree of
Doctor of Philosophy

University of Washington
2025

Reading Committee:
Michael Gerner, Chair
Jessica Hamerman
Steven Ziegler

Program Authorized to Offer Degree:
Immunology

University of Washington

Abstract

Generation of immune responses within lymph nodes during type-I inflammation

Jessica Huang

Chair of the Supervisory Committee:
Michael Gerner
Department of Immunology

Immune responses must be rapid, tightly orchestrated, and tailored to the encountered stimulus. Lymphatic vessels facilitate this process by continuously collecting immunological information (i.e., antigens, immune cells, and soluble mediators) about the current state of peripheral tissues, and transporting these via the lymph across the lymphatic system. Lymph nodes (LNs), which are critical meeting points for innate and adaptive immune cells, are strategically located along the lymphatic network to intercept this information. Within LNs, immune cells are spatially organized, allowing them to efficiently respond to information delivered by the lymph, and to either promote immune homeostasis or mount protective immune responses. These responses involve the activation and functional cooperation of multiple distinct cell types, and are tailored to the specific inflammatory conditions. The natural patterns of lymph flow can also generate spatial gradients of antigens and agonists within draining LNs, which can in turn further regulate innate cell function and localization, as well as the downstream generation of adaptive immunity. In this dissertation, we explore how information transmitted by the lymph shapes the spatiotemporal organization of innate and adaptive immune responses in LNs, with particular focus on type-I inflammation.

Table of Contents

Acknowledgments

Thank you to my family for giving me the freedom to pursue my passions. I can only do so because I know you will always be there for me.

To the past and present members of the Gerner lab, thank you for your friendship and all the fun conversations. I am also grateful to the many people in the department who have encouraged and supported me throughout the years.

Finally, thank you, Michael, for inspiring me, teaching me, and taking me to the finish line. You are a fantastic mentor. This dissertation is dedicated to the incredible journey that we have shared.

Chapter 1: Introduction

This chapter is adapted from the following manuscript:

Huang JY, Lyons-Cohen MR, Gerner MY. Information flow in the spatiotemporal organization of immune responses. *Immunol Rev*. Mar 2022;306(1):93-107.doi:10.1111/imr.13046

1.1 Role of lymph and lymph nodes in the immune response

The primary function of the vertebrate cardiovascular system is the regulation of body homeostasis. Blood vasculature supplies oxygen and nutrients to cells and tissues as well as removes waste products for elimination, while the lymphatic system maintains tissue balance by returning interstitial fluids via lymph back into the circulation[1]. In addition to these essential functions, the cardiovascular system is also integrally connected to the organization and function of the immune system[2,3]. Most adaptive lymphocytes and many innate cell types continuously recirculate via the blood, and this promotes rapid trafficking to lymphoid and non-lymphoid organs for surveillance and host defense. The lymphatics, on the other hand, carry information pertaining to the state of peripheral tissues, such as antigens, immune cells, inflammatory mediators, and other soluble molecules[2-7]. The lymphatic vasculature originates within the tissues as a network of blind-ended, thin-walled lymphatic capillaries, which are highly permeable and specialized in fluid uptake[1,3,8]. The lymphatic capillaries within the tissues coalesce into larger collecting lymphatic vessels that facilitate lymph transport, and these vessels eventually converge onto the thoracic duct, which empties the lymph into the subclavian veins to return this fluid back into the blood circulation[1].

Located along the path of lymph return are specialized lymphoid organs, called lymph nodes (LNs), which coordinate the information derived from adjacent peripheral tissues via the lymphatics, as well as promote surveillance of this information by the recirculating lymphocytes.

Indeed, the formation of LNs themselves is intimately tied to both the blood and lymphatic vascular networks, as blood vessels supply the first lymphoid tissue inducer cells to drive early LN anlagen, while interstitial flow within the lymphatic vessels provides the spatial and mechanical cues to form the subcapsular sinus and promote LN expansion[9]. Critically, LNs are strategically positioned along the lymphatic network to intercept information transported by the lymph, in order to contain pathogens and limit dissemination, as well as to present this antigenic information to the recirculating T and B cells[10]. Lymph-borne proteins are further concentrated within LNs via the reticular conduit network, which transports fluids and small molecules back into the blood circulation, while retaining larger particulate proteins or pathogens for sampling by the LN innate sentinel cells[11-14]. These innate cells are localized in a highly organized manner within LNs, and this allows for an extraordinary level of efficiency in sampling of antigens, detection of dangerous insults and pathogens, transmission of signals among responding innate immune cells and cognate lymphocytes, and the generation of robust antigen-specific adaptive responses specifically tailored to the nature of the stimulus[15-17]. Together, this intersection of information gathering via the lymphatic system, adaptive lymphocyte recirculation via blood vessels, and local cellular organization makes LNs ideal hubs for the induction and regulation of immunity, based on the specific organismal needs.

1.2 Lymph node organization and function at steady state

At both steady state and during inflammation, lymph formed in upstream tissues enters LNs via the afferent lymphatic vessels, passes through the subcapsular and cortical lymphatic sinuses, and then exits via the efferent lymphatic vessels located in the LN medulla to eventually return to the blood circulation. Most LN macrophages, including subcapsular sinus macrophages lining the B cell follicles as well as medullary macrophages, are localized directly within the

lymphatic sinuses. This enables efficient surveillance of draining lymph, and promotes rapid capture of pathogens that arrive via the lymphatics[18,19]. Strategically prepositioned close to the subcapsular sinus macrophages are multiple innate lymphoid cells, including NK cells, gamma-delta T cells, NKT cells, and innate-like CD8 T cells[20-22]. These cells are poised to immediately respond to macrophage-derived signals upon inflammation and help initiate early immune responses[21]. Central memory CD8 T cells are also localized nearby, and survey neighboring innate cells for cognate antigens presented on MHC molecules[23-25]. Together, these cells serve to patrol the outer periphery of the LN and defend the site against invading pathogens that disseminate from the lymphatics[10].

In addition, our quantitative 2-dimensional (2D) and 3D imaging studies have revealed that LN resident conventional dendritic cells (cDCs), and in particular resident cDC2s, also preferentially localize near or directly within the lymphatic sinuses[26,27]. This enables robust sampling of draining antigens and allows these cells to induce T cell responses during inflammation[13,27,28]. While some resident cDC1s also reside within these lymphatic sinus regions, most cDC1s are found more evenly distributed throughout the T cell zone and in close association with LN blood vessels[26,29]. Although this reduces their efficiency in sampling of lymph-borne antigens[13,27], more centralized positioning may enhance information exchange with migratory cDCs, which localize there, and allow the interception of potentially infected or dying cells during viral infections and cancer[30-32]. Close associations of resident cDC1s with blood vessels may also promote homeostatic maintenance of high endothelial venules to support normal lymphocyte recirculation[29,33]. These differences in cDC subset positioning have been recapitulated in human LNs, thus revealing the conservation of cDC subset patterning across species and suggesting likely functional importance for maintenance of homeostasis or host defense[34].

cDCs residing directly within peripheral tissues also constitutively sample local antigens. In the steady state, tonic signaling within tissues induces a fraction of these cells to undergo homeostatic maturation[35-38], and this induces their migration via the lymphatics into the nearest LNs in a CCR7-dependent manner[6,39-41]. Within LNs, different migratory cDC subsets segregate into distinct spatial compartments, and this is observed both at steady state and during inflammation[16]. Specifically, work by our group and others on cutaneous LNs (the focus of this dissertation) has demonstrated that migratory cDC1s and Langerhans cells (ontogenically closely related to macrophages) preferentially migrate into the deep T cell zone, while migratory cDC2s generally localize to the interfollicular regions and outer LN paracortex[26,29,42,43]. Further segregation of mpmigratory cDC2 subpopulations is seen based on CD301b and SIPRα marker expression. CD301b+ cDC2s are primarily found at the upper paracortex bordering the B cell follicles, while SIRPα- migratory cDC2s (also described as "triple negative" cDC2s) predominantly accumulate in the lower cortical ridge bordering the medulla[29,44-46].

At steady state, lymph supplies a large repertoire of tissue-derived self-antigens, including byproducts from apoptotic cells and catabolized extracellular matrix components[4,7]. The dominant role of these steady state cDC populations in LNs is to present captured peripheral self-antigens on MHC molecules to T cells in a non-immunogenic fashion. This is essential for inducing peripheral tolerance to potential self-reactive T cells, which may have escaped central thymic selection and entered the circulation[35,37,38,47]. While cDCs are critical for this process, we have found that they can also aberrantly activate self-reactive T cells[48,49]. In these instances, local regulatory T cells help maintain immune quiescence by forming discrete clusters around the autoreactive cells and quickly constraining self-reactive responses[48-52].

1.3 Stromal cells in the organization of lymph node innate immune cells

Such intricate compartmentalization of immune cells in LNs is thought to be at least in part mediated by the signals provided by the underlying stroma. Recent single-cell RNA sequencing studies have revealed the existence of multiple subsets of LN stromal cells with divergent properties, such as expression of distinct chemokines and adhesion molecules, as well as preferential production of survival factors to support immune cell homeostasis[53-59]. In brief, lymphatic endothelial cells (LECs) and marginal reticular cells line the subcapsular sinus and promote the homeostatic maintenance of subcapsular sinus macrophages[60,61], as well as express chemokine scavenging receptors to establish CCL21 chemokine gradients that help guide migratory cDCs from the sinuses into the LN parenchyma[62]. Follicular dendritic cells, located within the B cell follicles, secrete abundant amounts of CXCL13 to recruit and position CXCR5+ naïve B cells, T follicular helper (TfH) cells, as well as CXCR5-expressing migratory cDCs in certain inflammatory settings[58,63-66]. In the paracortex, multiple populations of T-zone reticular cells (TRCs) can be found, which secrete the chemokines CCL19 and CCL21 to promote homing of CCR7-expressing T cells and activated cDCs to the deep T cell zone[63,67-70]. A unique population of CCL19-low TRCs are found along the T-B border and the interfollicular regions, and these stromal cells preferentially generate the chemotactic ligands for Ebi2 receptor-expressing immune cells[54].

With regard to innate cell positioning, Ebi2 is preferentially expressed on resident and migratory cDC2 populations and is thought to promote their localization and maintenance within the marginal zone bridging channels of the spleen, as well as within the outer paracortical regions of the T cell zone[71-73]. Nevertheless, our quantitative imaging studies have demonstrated that disruption of the Ebi2 chemotactic axis has minimal effects on cDC distribution within cutaneous

LNs[74], suggesting that additional mechanisms can contribute[72]. Our group's findings on the preferential localization of resident cDC1s, and to a lesser degree cDC2s, near LN blood vessels also suggest existence of additional guidance cues emanating either directly from the blood endothelial cells or the surrounding pericytes[29]. Of note, the discrete spatial patterning of resident cDC1 and cDC2 populations results in preferential coating of distinct vascular trees, with little intermixing between subsets, and this could be related to the substantial heterogeneity seen in the LN blood endothelial cells[75,76]. Alternatively, preferential cDC coating of vasculature may also result from local recruitment of pre-cDC1 vs. pre-cDC2 precursors via distinct blood vessels and their spatially segregated proliferation to repopulate the mature cDC subsets[77-79]. In this regard, a recently identified subset of Grem1+ TRCs has been shown to localize within the outer LN paracortex, a region highly enriched in high endothelial venules[57,80]. This stromal cell population expresses several genes related to cDC recruitment and survival, and plays a crucial role in resident cDC homeostasis. It must also be noted that reciprocal crosstalk of cDCs with both LN fibroblastic reticular cells and blood endothelial cells via lymphotoxin beta and Clec2a signaling has been shown to be critical for promoting the survival and function of LN stromal cells themselves, during both steady state and inflammation[33,81-85]. Thus, while the exact mechanisms remain to be worked out, the extensive stromal cell heterogeneity within LNs is thought to establish the appropriate spatial patterning and survival of various cDC subsets, and in return these cDCs support normal stromal cell homeostasis.

1.5 Dissertation objectives

For this dissertation, we examine how information transmitted by the lymph shapes the spatiotemporal organization of innate and adaptive immune responses in LNs, with particular focus on type-I inflammation associated with rapidly draining pathogens or vaccines.

Chapter 2: Innate cell microenvironments in lymph nodes shape the generation of T cell responses during type I inflammation

This chapter is adapted from the following manuscript:

Leal JM, Huang JY, Kohli K, et al. Innate cell microenvironments in lymph nodes shape the generation of T cell responses during type I inflammation. *Sci Immunol*. Feb 12 2021;6(56)doi:10.1126/sciimmunol.abb9435

2.1 Introduction

Spatiotemporal coordination and cross-talk between various innate and adaptive immune cells are critical for timely generation of protective immunity[15]. During infection or vaccination, conventional dendritic cells (cDCs) migrate from peripheral tissues to draining lymph nodes (dLNs) in a C-C chemokine receptor type 7 (CCR7)–dependent manner to present captured antigens on major histocompatibility complex (MHC) molecules to induce T cell responses[41,86-88]. In addition, much faster transport of microbes, vaccine components and soluble antigens into dLNs occurs via lymphatic transport[13,27,89,90]. Within LNs, steady-state LN-resident cDCs (Res cDCs) and, in particular, Res cDC2s localize near lymphatic sinuses[26]. This promotes robust sampling of draining antigens and, in combination with the enhanced capacity of cDC2s for MHC-II presentation, allows efficient induction of CD4 T cell responses[13,27,89]. Res cDC1s, cells specialized in MHC-I cross-presentation, are more homogeneously distributed throughout the T cell zone (TZ)[26,43,91]. This reduces efficiency of antigen capture after subunit vaccination[13,27] and instead promotes the interception of infected migratory cDCs and dying cells, leading to enhanced CD8 T cell responses during viral infections or cancer[30-32].

In response to Toll-like receptor (TLR) stimulation, cDCs increase expression of costimulatory molecules and produce various inflammatory cytokines, such as interleukin-12 (IL-12), to elicit the differentiation of effector T cells[86]. Current models propose that a single cDC delivers all three signals (peptide-MHC, costimulation, and polarizing cytokines) to cognate T lymphocytes to induce their programming[86]. However, T cells can also integrate signals from serial interactions with multiple cDCs or other innate cell populations[30,31,92]. In particular, inflammatory monocytes (MOs) can migrate to dLNs after infection or vaccination to modulate T cell responses[93-95]. Detailed mechanisms of whether MOs transport antigens from peripheral tissues or directly traffic into LNs via high endothelial venules (HEVs) and whether they present antigens or promote cytokine-driven T cell responses are less clear[93-99].

Even at steady state, myeloid cells generate intricate spatial patterns within LNs[16,26,29]. During inflammation, they can undergo further reorganization and together with influx of new myeloid cells are likely to generate additional microenvironments[91,100,101]. T cells activated within different microenvironments may thus receive distinct stimuli and undergo divergent programs of activation. This is supported by substantial heterogeneity in clonal expansion and effector differentiation observed for individual T cells bearing identical T cell receptors (TCRs)[102-105]. However, studying how local tissue microenvironments influence T cell priming has been challenging, as this requires the use of advanced in situ imaging approaches capable of simultaneously mapping multiple myeloid and lymphoid cell populations, as well as their activation, differentiation, and functional states.

Here, we used advanced analytical imaging to characterize the spatial organization of innate and adaptive responses in dLNs during type I or type II inflammation elicited with distinct vaccine adjuvants or infections[106-109]. We found that type I inflammation was associated with a

signature of myeloid cell organization in dLNs, with rapid repositioning of Res cDCs from the LN periphery into the deep TZ, as well as robust infiltration of the TZ by inflammatory MOs. These changes were not observed during type II inflammation, suggesting specificity in myeloid cell patterning based on inflammatory conditions. Within the TZ, spatially juxtaposed Res cDCs and MOs functionally cooperated with one another, providing complementary stimuli to T cells to promote optimization of cellular responses. Moreover, MO infiltration was nonuniform across the LNs, leading to the formation of MO-rich versus cDC-dominated microenvironments. Priming of T cells within these different microenvironments led to generation of distinct early effector populations, allowing for formation of effector heterogeneity. Thus, our findings reveal a signature of myeloid cell organization during type I inflammation, as well as demonstrate that innate cell microenvironments influence the magnitude, quality and heterogeneity of adaptive responses.

2.2 Results

DC relocalization and MO influx in LNs during type I inflammation

We previously reported that preferential localization of Res cDC2s in lymphatics-proximal regions promoted robust T cell responses to subunit vaccination[13,27,74]. However, naïve T cells primarily reside in the TZ, and how efficient T cell activation was achieved remained unclear. One possibility is that during inflammation, innate cells are spatially reorganized to promote physical interactions with T cells. To investigate how intranodal positioning of myeloid cells changes during inflammation, we injected mice with a broad array of vaccine adjuvants, including type I inflammatory TLR agonists: Cytosine-phosphorothioate-guanine oligodeoxynucleotides (CpG; TLR9), R848 (TLR7/8), flagellin (TLR5), lipopolysaccharide (LPS; TLR4), and polyinosinic:polycytidylic acid (p(I:C); TLR3); type II adjuvants: Alhydrogel (Alum) and Addavax (MF59 analog), as well as the protease allergen, papain. Adjuvants were initially used as

they are clinically relevant and have well-defined drainage and inflammatory properties. One day after immunization (subcutaneous, footpad, or intradermal), dLNs were isolated, and the localization of myeloid cell subsets was visualized with multiparameter confocal imaging and analyzed with histocytometry. Multiplexed staining for CD11c, MHC-II, CD169, CD64, SIRPα (CD172α), C-type lectin domain containing 9A (Clec9A), and other myeloid markers allowed clear discrimination of migratory and Res cDC populations as well as other myeloid cell types (fig. S1A and table S1).

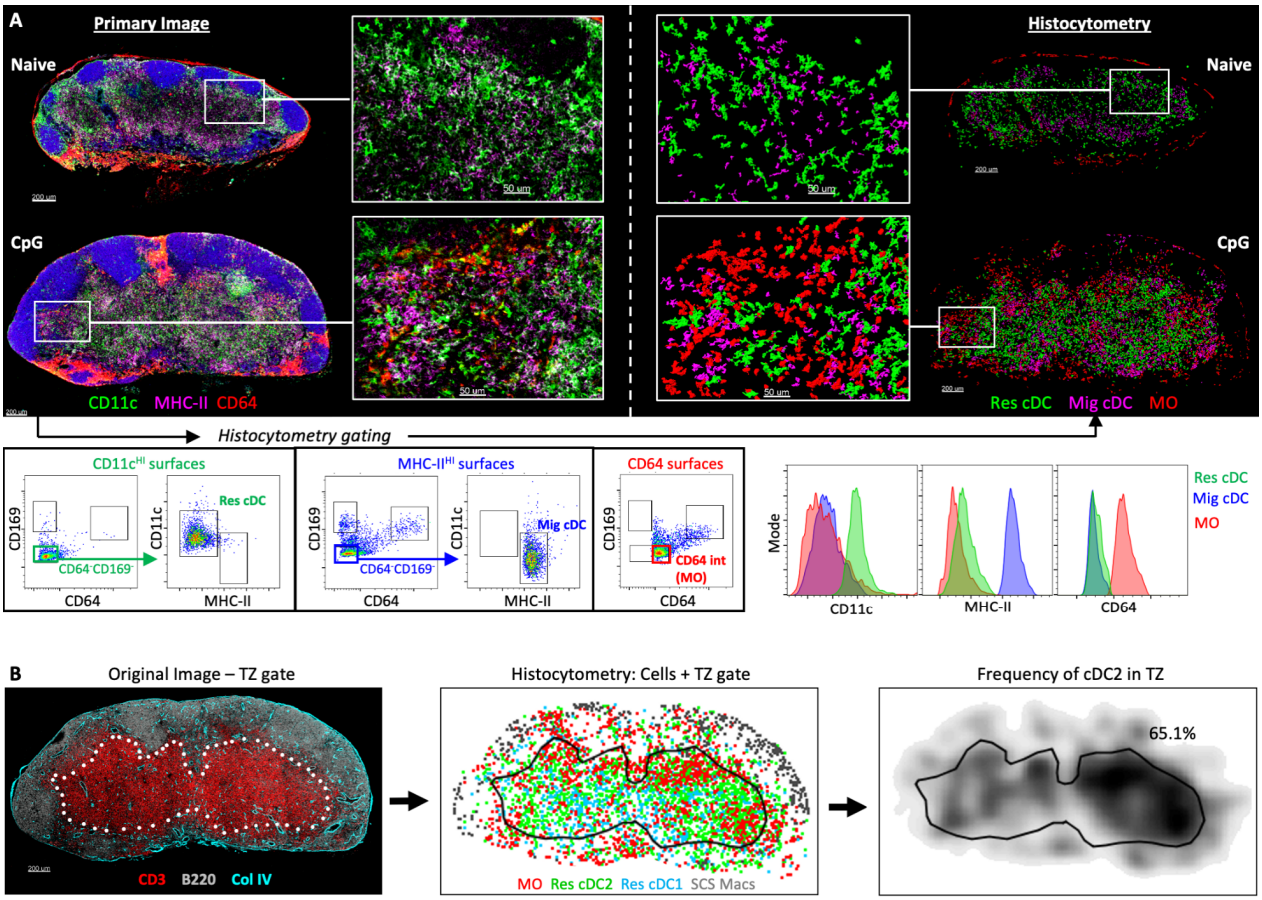

Figure S1: Histocytometry analysis of myeloid cell positioning.
(**A**) B6 mice were injected in the ears with CpG and dLNs were harvested 24 hours later for imaging. Representative staining for the indicated cell markers is shown (top left). Surface objects were next created using CD11c, MHC-II, and CD64 channels and exported for histocytometry analysis. Histocytometry gating scheme demonstrates identification of Res cDCs, migratory cDCs (Mig cDC), and MOs (bottom dot plots), as well as analysis of indicated marker expression (bottom histograms). These populations were next positionally mapped to visualize cell distribution (top right). Zoom-in panels demonstrate congruency

between the original image (top left) and histocytometry data (top right). (**B**) Representative TZ gating scheme. Both CD3 and B220 markers were used to identify the border of the TZ within the primary image, and the positional data of this TZ boundary was exported to FlowJo for spatial gating of the myeloid cell populations via histocytometry. SCS Macs, subcapsular sinus macrophages.

FLOW CYTOMETRY

	CCR2-RFP	CD11b	CD11c	CD26	CD64	CD88	CD103	CD301b	EpCAM	Ly-6B.2	Ly6C	MAR-1	MHC-II	SIRPα	XCR1ł
Res cDC1	- / INT	-	HI	+	-	-	-	-	-	-	LO	-	INT*	-	+
Res cDC2	- / INT	+	HI	+	-	-	-	-	-	-	LO	-	INT*	+	-
Mig cDC1	- / INT	-	INT	+	-	-	+	-	LO	-	LO	-	HI	-	+
Mig cDC2	- / INT	+	INT	+	-	-	-	+ / -	LO	-	LO	-	HI	+	-
MO	HI	+	+ / -	-	+	+	-	-	-	+	+	+	+ / -	+	-

Dump = B220, CD3, CD19, Ly6G, NK1.1

HISTOCYTOMETRY

	CCR2-RFP	CD11b	CD11c	CD64	CD169	Clec9ał	MHC-II	SIRPα
Res cDC1	- / INT	-	HI	-	-	+	LO*	-
Res cDC2	- / INT	+	HI	-	-	-	LO*	+
Mig cDC1	- / INT	-	LO	-	-	+/-	HI	-
Mig cDC2	- / INT	+	LO	-	-	-	HI	+
MO	HI	+	+ / -	INT	-	-	+ / -	+
Macs	-	+	- / INT	HI	+	-	- / INT	+

* Upregulated during inflammation
ł Downregulated during inflammation

Table S1: Description of cellular phenotypes for flow and imaging studies.
Summary of the molecular profiles for the indicated myeloid cell populations, examined by both flow cytometry and histocytometry.

We observed that all tested TLR agonists elicited marked repositioning of Res cDC2s from the peripheral LN regions into the deep TZ (Fig. 1, A and B, and figs. S1B and S2, A and B). This was quantified using a positional TZ gate generated with CD3 and B220 staining delineating the B cell follicles and TZ, respectively (Fig. 1B, and figs. S1B and S2B). Although Res cDC1s were less abundant in the lymphatic proximal regions as compared with cDC2, these cells also relocalized to the deep TZ after TLR agonist immunization (Fig. 1, A and B). cDC repositioning was similarly detected by calculating the distance of cells from the deep TZ (fig. S2A). As expected, after repositioning, Res cDC1s and cDC2s did not occupy the same regions within the TZ (Fig. 1A and fig. S2A), supporting previous observations of Epstein-Barr virus-induced G-protein coupled receptor 2 (Ebi2)–mediated compartmentalization[72,73]. None of the tested type II stimuli elicited Res cDC repositioning, suggesting that this response is specific to type I inflammatory

conditions (Fig. 1, A and B, and fig. S2C). Kinetics studies revealed that Res cDC relocalization began by 9 hours after immunization (Fig. 1C and fig. S2D), indicating that this was a relatively rapid phenomenon likely associated with the drainage of soluble TLR agonists into the dLNs[110].

In addition, TLR agonist immunization elicited the appearance of large numbers of $CD64^{+}SIRPa^{+}CD169^{-}$ cells, markers associated with inflammatory MOs[111,112], within the deep TZ of dLNs (Fig. 1, A and B, and fig. S2, A and B). This was confirmed by flow cytometry, which demonstrated robust influx of $Ly6C^{+}CD64^{+}CD11b^{+}Ly6G^{-}CD3^{-}CD19^{-}NK1.1^{-}$ MOs into immunized dLNs (fig. S2, E to G, and table S1), beginning as early as 8 hours, and peaking at 12 to 16 hours after immunization (Fig. 1, C and D, and fig. S2D). Some differences in MO recruitment between the different TLR agonists were noted, with LPS inducing comparably lower responses. Minor increases in MO number were also seen after papain administration, albeit these cells did not efficiently penetrate the deep TZ (Fig. 1, A and B). Both the centralization of Res cDCs and the presence of MOs within the TZ were observed on day 2 after immunization (see below), suggesting that type I inflammation is associated with lasting changes in the composition and organization of innate cells within the dLNs. Immunization also led to increased number of migratory cDCs, and as expected these cells were localized within the TZ (fig. S2, A and H).

We next investigated whether these phenomena also applied to the type I inflammatory settings seen during infection. Robust Res cDC relocalization and MO recruitment were seen after administration of heat-killed *Escherichia coli* (fig. S2I) and after West Nile virus infection (Fig. 1, E and F). In contrast, infection with *Nippostrongylus brasiliensis*, which is associated with type II inflammation, did not elicit these effects in skin dLNs (fig. S2J). Together, these data demonstrated that type I inflammation induced by TLR agonist administration, bacterial inoculation, and West

Nile virus infection induced the redistribution of Res cDCs into the deep TZ and robust recruitment of MOs into the dLN.

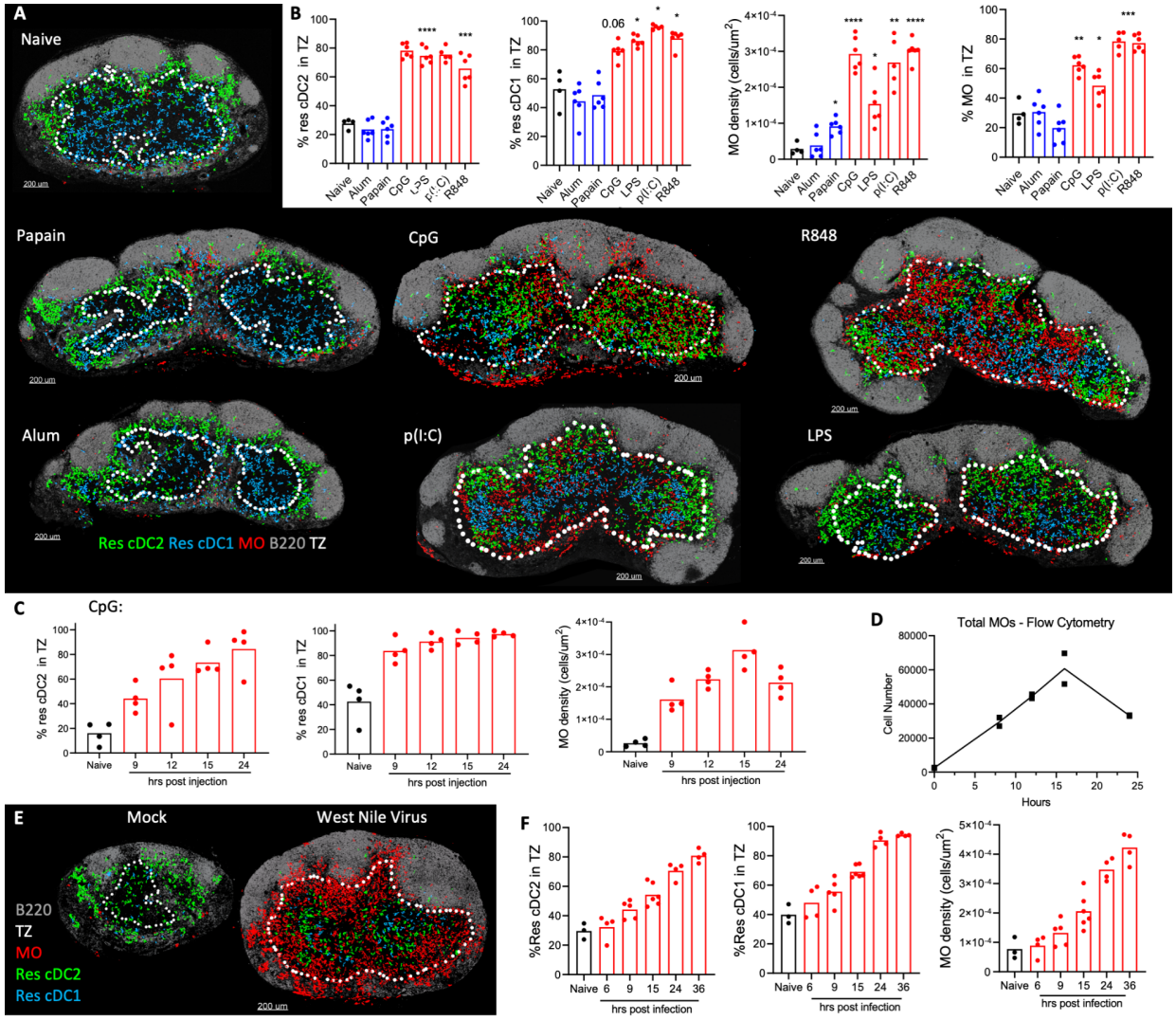

Fig. 1. MO influx and Res cDC TZ relocalization during type 1 inflammation.
(**A** and **B**) B6 mice were injected in the ears with the indicated adjuvants and dLNs were analyzed 24 hours later by histocytometry. (A) Representative images depicting Imaris 3D surfaces for indicated cell types, overlayed with B220 staining. White circles denote the TZ boundary (see fig. S1A for gating). (B) Frequency of Res cDCs and MOs within the TZ, as well as MO density. Data analyzed using Brown-Forsythe and Welch ANOVA tests with Dunnett's multiple comparison. (**C** and **D**) B6 mice were immunized with CpG in both ears, and dLNs were analyzed at indicated time points. (C) Histocytometry for Res cDC localization and MO density. (D) MOs in dLNs enumerated by flow cytometry. Data representative of five independent experiments. (**E** and **F**) B6 mice were infected in the footpad with 100 PFU of West Nile virus TX and dLNs were analyzed by histocytometry. (E) Representative images from mock infected and 36 hours after infection. (F) Localization of Res cDCs and MO density at the indicated time points. Scale bars, 200 μm. Data represent at least two independent experiments.

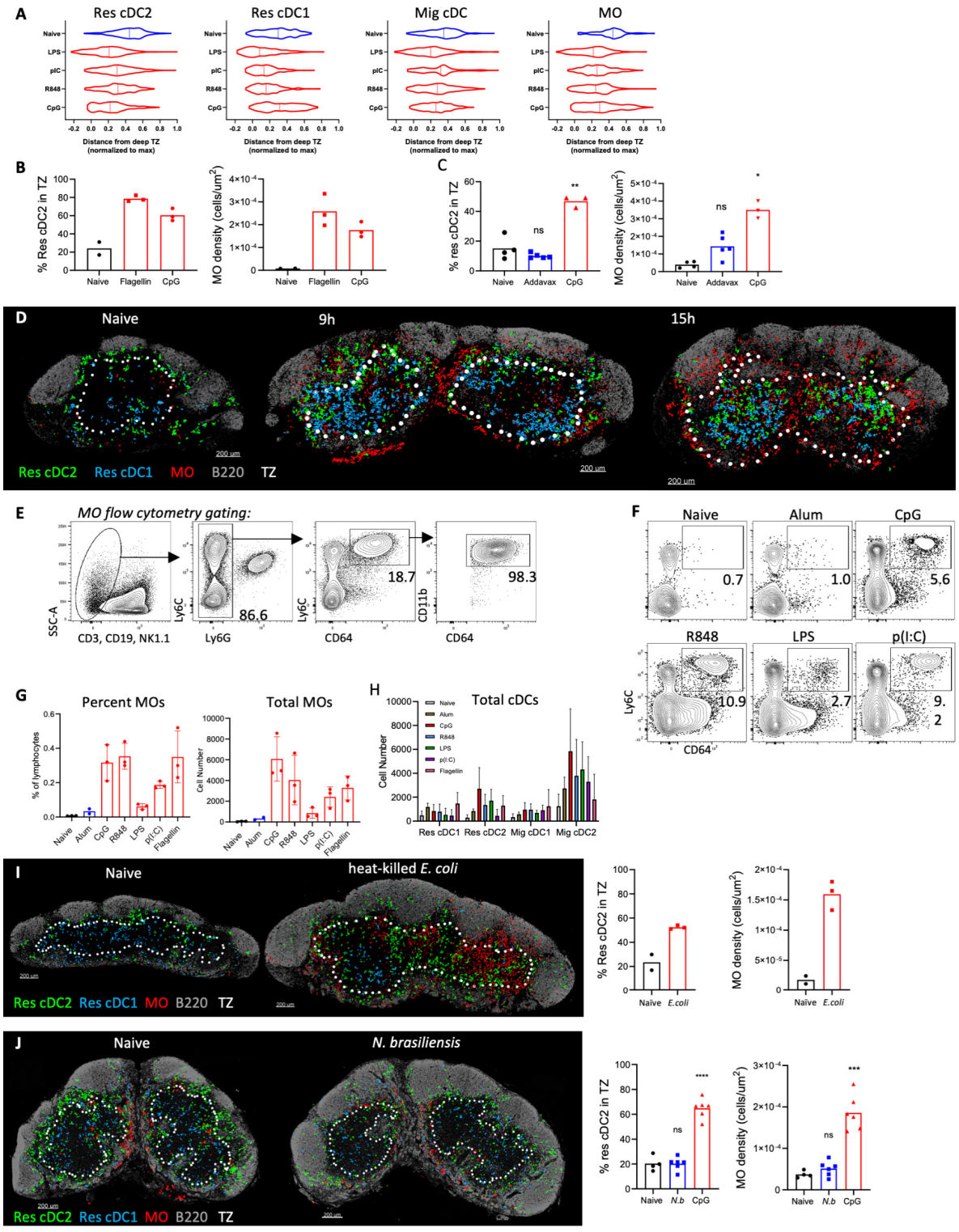

Fig. S2. Analysis of myeloid cell recruitment and localization within LNs in response to various stimuli.

(**A**) Positional data for histocytometry-gated cell populations were imported into CytoMAP and cell distances from the deep TZ center were calculated. Violin plots demonstrate the distribution of different

cell types in representative LNs (images shown in Fig. 1A) after injection with the indicated adjuvants. For comparison of LNs of varying sizes, cell distances were normalized to the maximum possible distance for each tissue. Positive values represent cells outside of the deep TZ boundary; negative values represent cells within the deep TZ boundary. (**B**) B6 mice were administered flagellin or CpG in the ears. Frequency of Res cDC2s within the TZ and MO density in dLNs was quantified by histocytometry 1 day later. (**C**) B6 mice were immunized with Addavax or CpG in the ears and footpads. Percentage of Res cDC2s in the TZ and MO density in dLNs was assessed by histocytometry 1.75 days later. ns, not significant. (**D**) Additional imaging data for the experiment presented in Fig. 1C, showing representative dLNs after CpG immunization at the indicated time points. (**E**) Representative flow cytometry gating scheme for MOs 1 day after CpG injection. (**F** to **H**) B6 mice were immunized with the indicated adjuvants in the ears and footpads and dLNs were harvested for flow cytometry 1 day later. (F) Representative flow cytometry plots of MOs, as well as (G) quantification of the frequency and total number of MOs per dLN. Cells in flow plots were first pre-gated on $CD3^{-}CD19^{-}NK1.1^{-}Ly6G^{-}CD11b^{+}$ populations. (H) Total number of Res and Mig cDC subsets in dLNs. For each group, n = 3 to 4. (**I**) B6 mice were injected in the ears with heat-killed *Escherichia coli* (*E. coli*). Res cDC localization and MO density in dLNs was quantified by histocytometry 1 day later. (**J**) B6 mice were infected with 500 *Nippostrongylus brasiliensis* (*N.b.*) worms, or injected with 40 μg of CpG, subcutaneously in the tail base. Inguinal dLNs were assessed by histocytometry 36 hours later for Res cDC localization and MO density. In (C) and (J), data analyzed by Brown-Forsythe and Welch ANOVA tests with Dunnett's multiple comparison. In (D), (I), and (J), Imaris-generated 3D surfaces are shown depicting the indicated cell types. Each point represents an independent LN. All data represent at least two independent experiments.

CCR7-mediated Res cDC intranodal repositioning during inflammation

We hypothesized that intranodal Res cDC repositioning was driven by chemotaxis[113]. Peripheral tissue cDCs up-regulate CCR7 expression for migration into the dLNs[114,115]. Splenic cDCs also use CCR7 to relocalize into the white pulp during systemic inflammation[72,73,116-118]. We thus examined CCR7 expression on Res cDCs after immunization. We found that after type I, but not type II, adjuvant administration CCR7 expression was markedly increased on both Res cDC subsets (Fig. 2, A and B, and fig. S3A). This was also associated with higher surface expression of MHC-II, indicative of Res cDC maturation (Fig. 2A and fig. S3A). Both CCR7 and MHC-II expression increased as early as 4 hours after immunization, and rapidly approached levels found on migratory cDCs (Fig. 2A). In contrast, expression of Ebi2, which can also influence cDC localization, was not substantially changed with immunization (fig. S3B).

To test the role of CCR7 in intranodal relocalization of Res cDCs, we generated mixed bone marrow chimeras (BMCs) consisting of a 50:50 mix of CCR7.KO, or control wild type (WT),

and BM from mice in which diphtheria toxin receptor is expressed under the cDC-lineage specific *Zbtb46* promoter (*Zbtb46*-DTR) (fig. S3C). This allowed specific depletion of *Zbtb46*-DTR donor cDCs using diphtheria toxin (DT), while leaving the CCR7.KO (DC-CCR7.KO) or control WT (DC-WT) cDCs intact[119,120]. This setup maintains normal LN architecture (fig. S3D), which is otherwise disrupted in CCR7 deficient animals[114]. No notable changes in the total number of Res cDCs or the size of the LNs were detected between DC-CCR7.KO and DC-WT BMCs after DT administration, although, as expected, migratory cDCs were absent in the DC-CCR7.KO LNs (fig. S3D). The DC-CCR7.KO and DC-WT mice were treated with DT and, 1 day later, immunized with CpG (fig. S3C). Disruption of CCR7 upregulation after immunization in DC-CCR7.KO was verified by flow cytometry (fig. S3E). As expected, Res cDCs in the control DC-WT BMCs efficiently relocalized into the deep TZ. In contrast, Res cDCs in DC-CCR7.KO BMCs were largely excluded from the TZ, and instead were frequently observed proximal to B cell follicles and medullary sinuses (Fig. 2, C and D, and fig. S3F). In contrast to cDCs, MOs still efficiently infiltrated the TZ in DC-CCR7.KO dLNs (fig. S3G), indicating that MO trafficking to and localization within dLNs was not interdependent with Res cDC repositioning. Mixed BMCs, consisting of a 50:50 mix of CCR7.KO and WT BM, also showed that CCR7.KO MOs did not display major defects in TZ infiltration (fig. S3H), confirming previous reports that MOs do not require CCR7 for migration into LNs[93,96]. Collectively, these data demonstrated that during type I inflammation, upregulation of CCR7 expression by Res cDCs leads to intranodal relocalization from the LN periphery into the deep TZ.

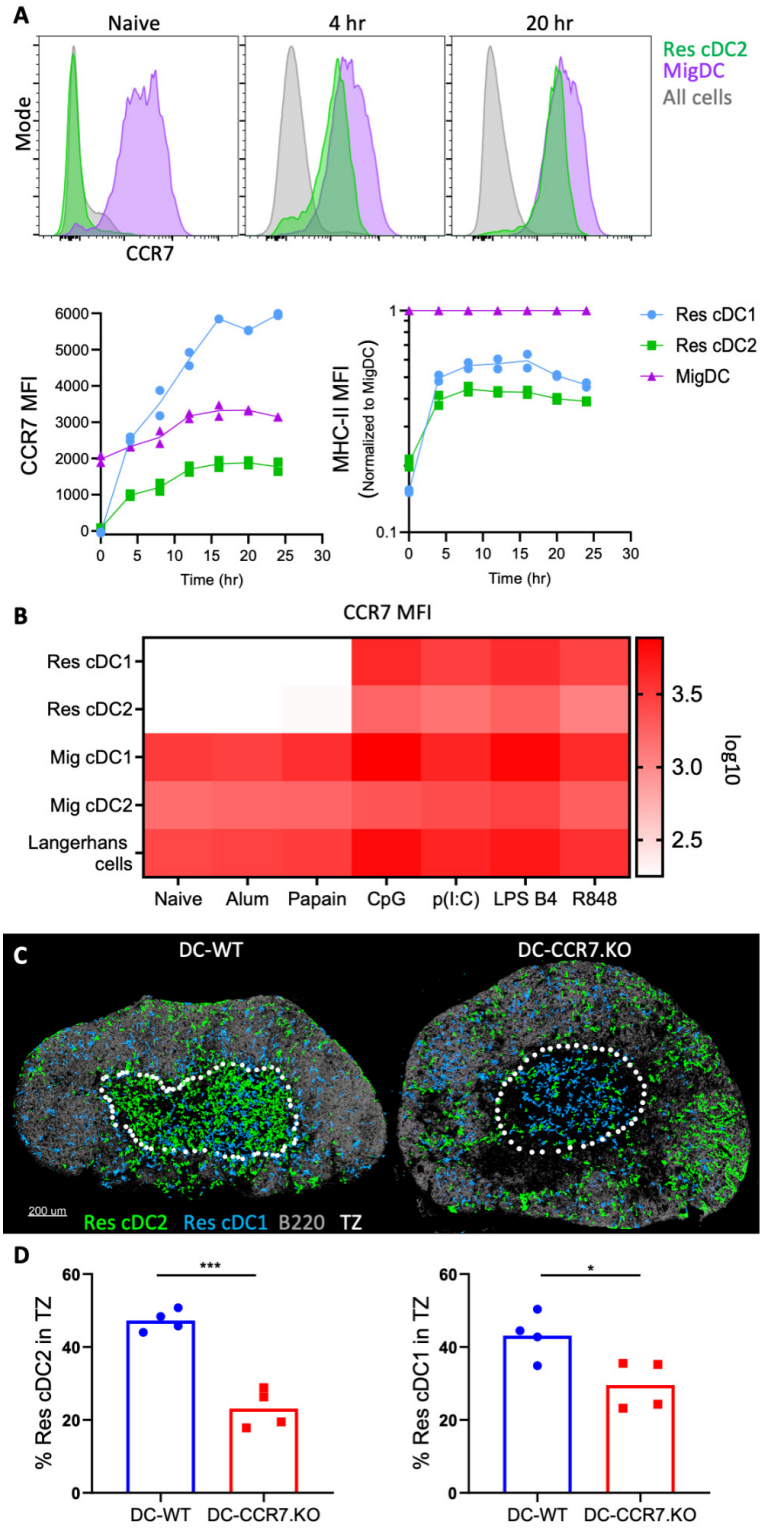

Fig. 2. CCR7-mediated Res cDC intranodal relocalization after immunization.

(**A**) B6 mice were injected in the ears with CpG, and dLNs were analyzed for cDC expression of MHC-II and CCR7 by flow cytometry (see fig. S3A for gating scheme). MHC-II geometric mean fluorescence intensity (MFI) was normalized to MHC-II on migratory cDCs (Mig cDC). (**B**) Heatmap depicting CCR7 geometric MFI on cDCs 24 hours after immunization with indicated adjuvants. Each square represents mean of n=4. (**C** and **D**) DC-CCR7.KO and DC-WT mixed BMCs were administered DT and injected with CpG 1 day later in the footpad. Histocytometry of popliteal dLNs 1.5 days later. Data analyzed by unpaired *t* test with Welch's correction. Data represent at least two independent experiments.

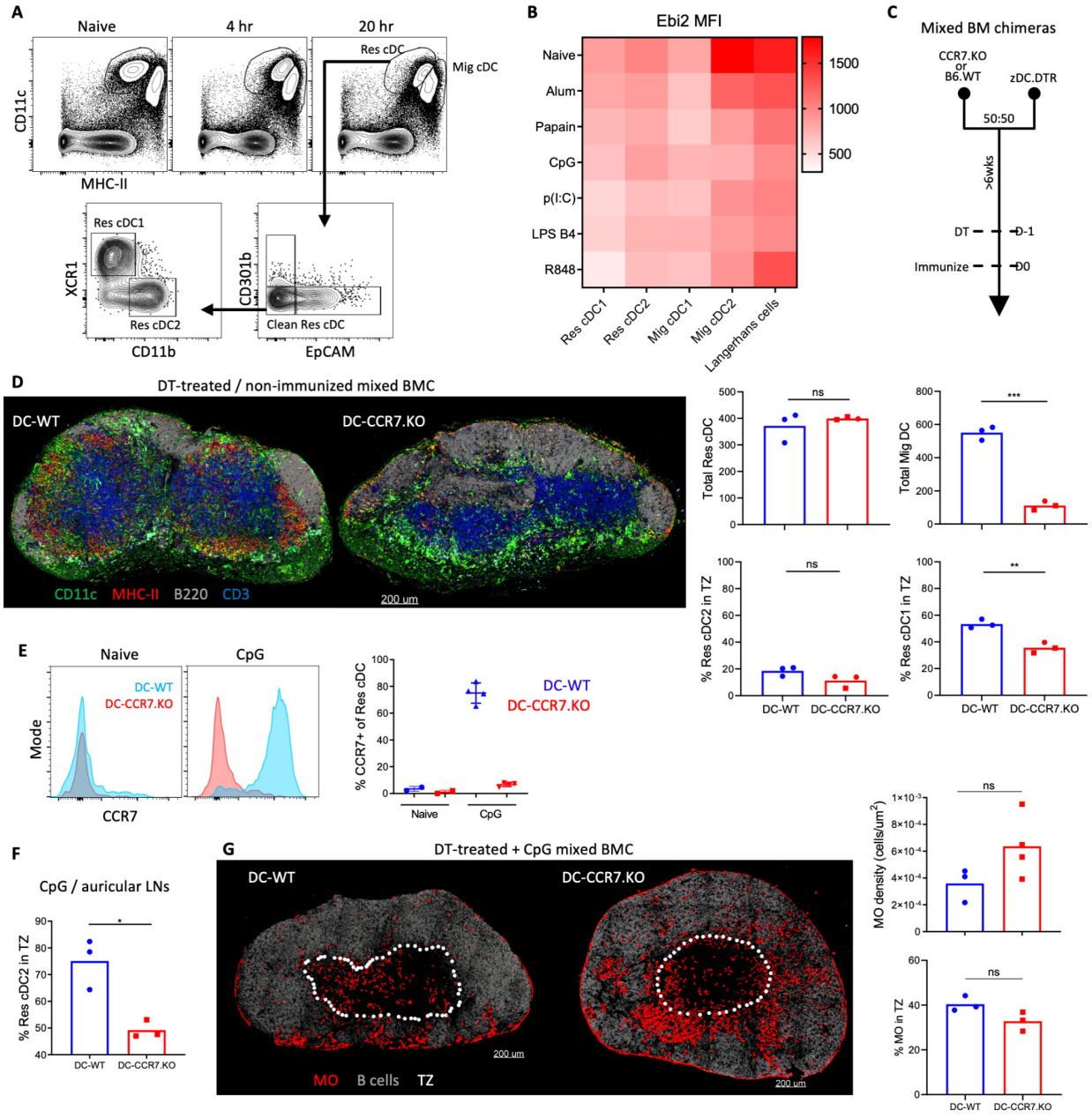

Fig. S3. Chemokine receptors expressed by cDCs and validation of DC-CCR7.KO BMC system. (**A**) Flow cytometry gating scheme used to identify cDC populations in LNs from the experiment described in Fig. 2A. To improve subset discrimination, cells staining positive for migratory cDC markers, EpCAM and CD301b, were excluded from Res cDC gating. (**B**) B6 mice were injected in the ears with the indicated adjuvants and cDC populations within dLNs were analyzed for the expression of Ebi2 by geometric mean fluorescence intensity (MFI) 24 hours later. Each square represents mean of n = 4. (**C**) Experimental schematic for the creation of DC-CCR7.KO and DC-WT mixed BMCs and subsequent immunization. (**D**) Representative primary images of auricular LNs from non-immunized DC-WT and DC-CCR7.KO mixed BMCs (left), as well as histocytometry analysis of cDC cellularity and frequency within the TZ (right). (**E** and **F**) DC-CCR7.KO and DC-WT mixed BMCs were treated with DT and then injected in the ears with CpG 1 day later. dLNs were harvested 1.5 days later. (E) Flow cytometry analysis verifying lack of CCR7 expression on Res cDCs in DC-CCR7.KO mice after CpG immunization. (F) Histocytometry analysis of

the percent of Res cDC2 found within the TZ of auricular dLNs. (**G**) Supplementary material for Fig. 2, C and D. DT-treated DC-CCR7.KO and DC-WT mixed BMCs were injected with CpG in the footpads. MO cellularity and localization was analyzed 1.5 days later. (**H**) B6 mice were irradiated and reconstituted with a 50:50 ratio of congenically marked CCR7.KO BM and B6 (WT) BM. Six weeks after BM transplant, mice were immunized in the footpads with the indicated adjuvants. dLNs were analyzed by histocytometry 1 day later. The ratio of total CCR7.KO MO to WT MO as normalized to MO reconstitution ratio in the BM (left), and the percentage of MOs in the TZ (right) was quantified. (D and F to H) Data analyzed by unpaired *t* test with Welch's correction. Each point represents an independent LN. In (H), data is representative of one independent flow cytometry experiment and one independent histocytometry experiment. All other data represent at least two independent experiments.

HEV-mediated recruitment of MOs into the dLNs

We next studied the mechanisms of MO recruitment during type I inflammation. MOs enter the circulation from the BM in a CCR2-dependent manner[99]. Consistent with this, blockade of CCR2 using an anti-CCR2 antibody significantly reduced MO recruitment into dLNs after immunization (Fig. 3A), without affecting the total numbers and localization of Res cDCs (fig. S4A). Further trafficking of MOs into dLNs could have occurred via two distinct routes: (i) initial MO recruitment into inflamed peripheral sites of immunization, followed by continued migration into dLNs via the afferent lymphatics or (ii) direct MO entry into dLNs from blood via HEVs[99]. To investigate the former possibility, mice were administered CpG in the ear, and the site of immunization was surgically removed 1 to 2 hours later. This allows for drainage of administered TLR agonists to dLNs during the initial hour after immunization, whereas the site removal precludes the subsequent migration of cells from the immunization site. This is especially true for MOs, which require additional time to traffic to the inflamed skin[121,122]. We observed similar numbers of MOs in both site-intact and site-removed dLNs 24 hours after immunization, suggesting that peripheral tissue trafficking was not the primary mechanism of early MO recruitment (Fig. 3B). Nevertheless, surgical trauma associated with site removal could independently promote MO mobilization and confound the results. We thus injected mice with a blocking antibody against P-selectin glycoprotein ligand-1 (PSGL-1), an adhesion molecule

predominantly involved in trafficking to inflamed peripheral tissues[123], and again immunized the animals in the ear, as well as performed site removal in some of the mice (Fig. 3B). PSGL-1 blockade, with or without site removal, led to a modest, but non-significant decrease in MO numbers in the dLNs, corroborating that early MO trafficking into dLNs was not predominantly occurring via the peripheral tissues. To test the possibility of direct migration of MOs via the HEVs, mice were treated with an anti-CD62L blocking antibody at the time of immunization, as CD62L is essential for HEV-mediated trafficking[124]. CD62L blockade led to a marked loss in MO cellularity (Fig. 3B). Combined anti-PSGL-1 and anti-CD62L blockade caused more minor additional decreases (Fig. 3B). This indicated that although minor trafficking of MOs via the afferent lymphatics may occur[96], HEV-mediated entry was the dominant pathway of early MO recruitment into the dLNs during type I inflammation.

To directly visualize the dynamics of MO trafficking, we performed two-photon intravital microscopy of dual-reporter CCR2–red fluorescent protein (RFP) × CD11c–yellow fluorescent protein (YFP) mice, which allowed concurrent visualization of both MOs and cDCs, respectively. LN vasculature was also intravenously labeled with fluorescently labeled anti-CD31 antibody or dextran, which does not alter cellular trafficking[125]. As anticipated, unimmunized mice exhibited very few MOs (RFP^+YFP^-) in the vasculature, and the few detected cells rapidly moved through the vessels (movie S1). In contrast, markedly increased numbers of RFP^+ MOs were observed in the dLN blood vessels starting 6 hours after immunization, and many cells exhibited slow rolling-type behavior and frequently extravasated into the parenchyma (Fig. 3, C and D, and movie S1). CCR2 can also be expressed by cDCs or effector T cells[126]. However, the rolling and extravasating RFP^+ cells were CD11c-YFP negative. Additional intravenous labeling for CD90, a T cell–specific molecule, also did not label most RFP^+ cells (fig. S4B). Moreover, the timing of MO detection

within the HEVs with intravital microscopy correlated with the kinetics data obtained by confocal imaging and flow cytometry (Fig. 1, C and D, and fig. S2D), collectively suggesting that type I inflammation elicits rapid MO recruitment into the dLNs via HEVs.

We next analyzed MO morphology and expression of CD11c and MHC-II, markers associated with MO differentiation. At early time points after immunization, MOs within the LN parenchyma exhibited a round morphology (fig. S4C), similar to cells within the HEV lumen (Fig. 3, C and D, and fig. S4B). Moreover, these recently arrived MOs were CD11c and MHC-II negative and were mainly localized in the TZ periphery (fig. S4C). Over time, MOs progressively displayed reduced sphericity, acquired a dendritic-like appearance, expressed CD11c, and migrated into the deeper LN paracortex (fig. S4, C and D). Flow cytometry confirmed that the early infiltrating MOs phenocopied intravenously labeled blood MOs, displaying minimal surface levels of CD11c and MHC-II (fig. S4E), and that with time, they gradually increased expression of both markers (fig. S4, F to H). Together, these data indicated that MOs were recruited into dLNs via local vasculature and underwent differentiation over time.

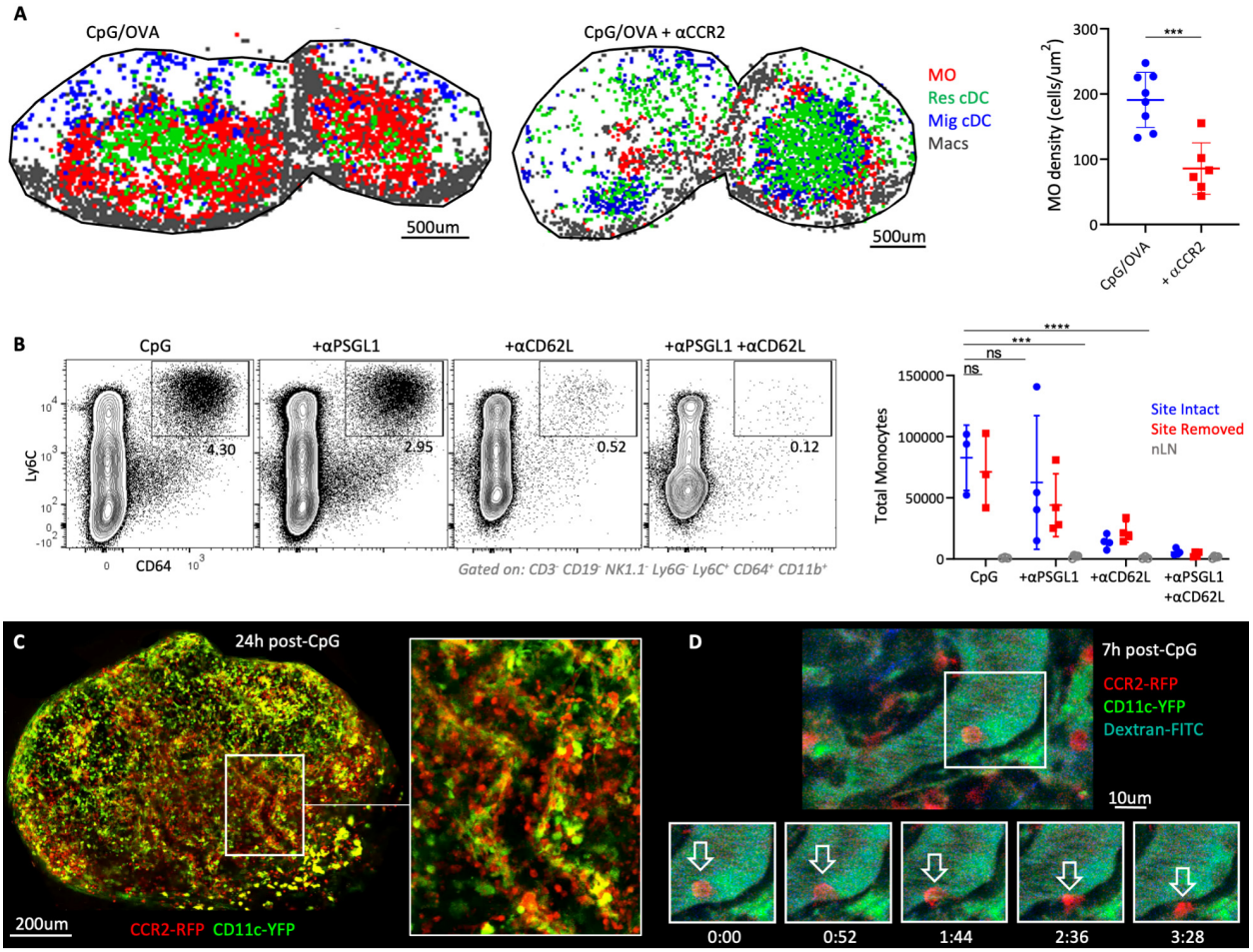

Fig. 3. HEV-mediated recruitment of MOs into the dLNs.
(**A**) OT-II–transferred B6 mice were immunized with CpG plus OVA in ears and footpads. Some animals were treated with αCCR2. Myeloid cell localization (left) and MO density (right) in dLNs were assessed by histocytometry 1.75 days later. Data analyzed by unpaired *t* test with Welch's correction. Macs, macrophages. (**B**) B6 mice were immunized with CpG in the ears. Some mice had the immunization site surgically removed 1 to 2 hours later, and/or were treated with αPSGL-1 and/or αCD62L. Total MOs in dLNs and nondraining LNs (nLN) were quantified 1 day later by flow cytometry. Data analyzed via one-way ANOVA with Dunnett's multiple comparisons test. ns, not significant. (**C** and **D**) CCR2-RFP × CD11c-YFP mice were administered CpG in the footpad and popliteal LNs were imaged by two-photon intravital microscopy (C) 24 hours or (D) 7 hours after immunization. Representative time-lapse images demonstrate MO extravasation. Data represent at least two independent experiments.

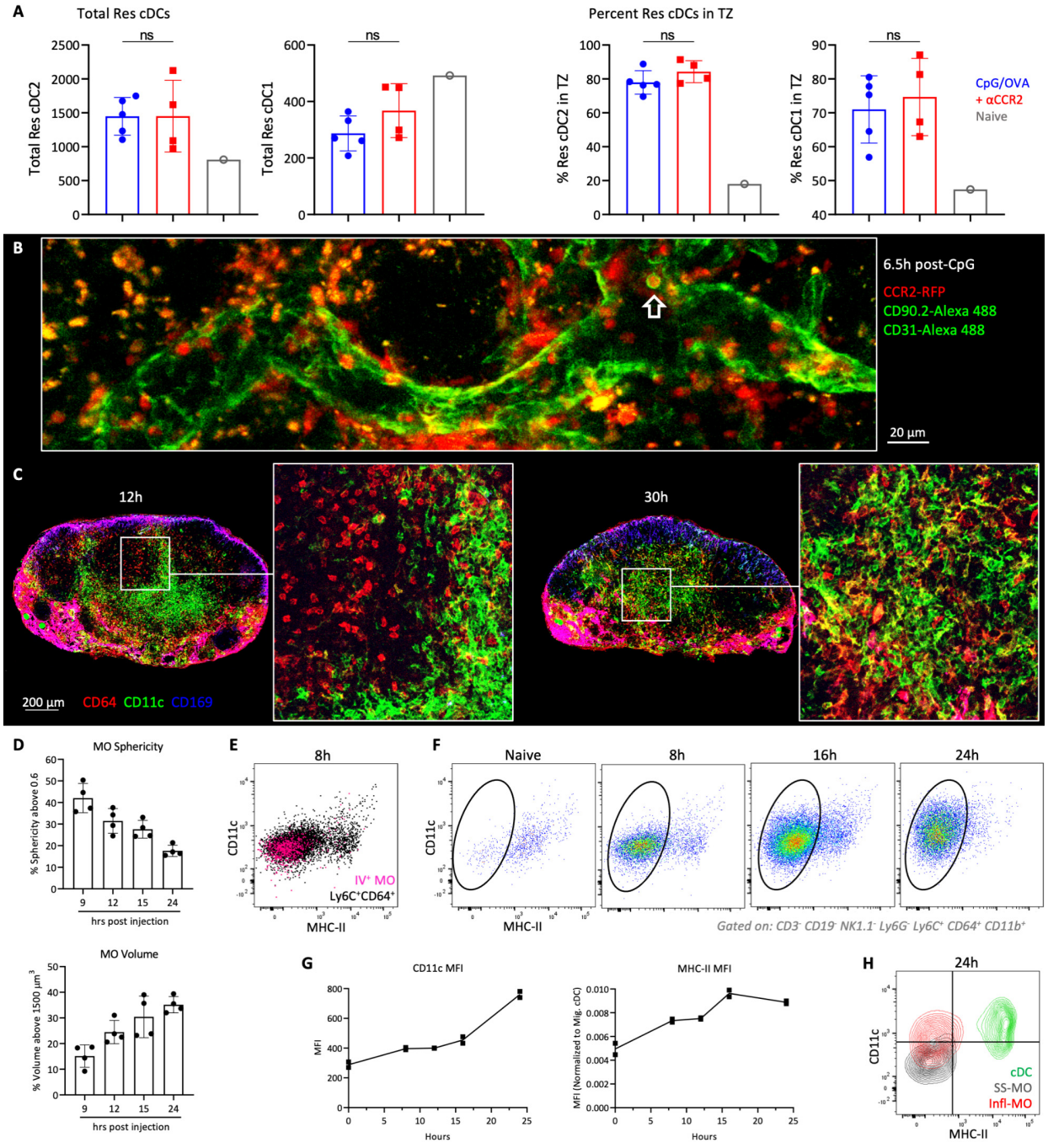

Fig. S4. HEV-mediated recruitment of MOs in the dLNs.

(**A**) Extended analysis for Fig. 3A, showing total Res cDCs (left) and percent of Res cDCs in the TZ (right) after CpG plus OVA immunization, with or without αCCR2 treatment. Data analyzed by unpaired *t* test with Welch's correction. (**B**) CCR2-RFP x CD11c-YFP mice were injected with CpG in the footpad and popliteal dLNs were imaged by two-photon intravital microscopy 6.5 hours later. 1.5 hours prior to imaging, mice were also intravenously administered both anti-CD31-Alexa 488 and anti-CD90.2-Alexa 488 to visualize the vasculature and to label T cells, respectively. Arrow shows a single RFP$^+$ cell labeled with the anti-CD90.2 antibody within the vasculature. Remaining CCR2$^+$ cells within the vasculature in this representative image are negative for CD90.2 staining. (**C** and **D**) B6 mice were injected with CpG in the

ears and dLNs were examined by imaging and histocytometry at the indicated time points. (C) Representative images demonstrating a change in morphology of $CD64^{+}CD169^{-}$ MOs, and their change in expression of CD11c at 12 versus 30 hours. (D) Histocytometry quantification of the percent MOs with spherical morphology (sphericity above 0.6) or with enlarged cell volume (volume above 1500 μm^3) at the indicated time points. (**E** to **H**) B6 mice were injected with CpG in the ears and dLNs were assessed at the indicated time points by flow cytometry. 10 minutes prior to harvest, mice were administered anti-CD45.2-PE intravenously (IV) to label cells within the vasculature. (E) Representative flow plot comparing CD11c and MHC-II expression on IV^{+} MOs (pink) overlaid on top of all $Ly6C^{+}CD64^{+}$ ($CD3^{-}CD19^{-}NK1.1^{-}Ly6G^{-}CD11b^{+}$) cells in the dLN (black), 8 hours after CpG injection. (F) Representative flow plots demonstrating CD11c and MHC-II expression on MOs at the indicated time points. Gated cells ($CD3^{-}CD19^{-}NK1.1^{-}Ly6G^{-}Ly6C^{+}CD64^{+}CD11b^{+}MHC\text{-}II^{-/INT}$) indicate proposed inflammatory MOs recruited into dLNs. (G) CD11c and MHC-II geometric MFI on inflammatory MOs at the indicated time points. MHC-II geometric MFI was normalized to migratory cDCs. Line connects means at each time point. Data is representative of five independent experiments. (H) Representative flow plot comparing CD11c and MHC-II expression on MOs from steady-state LNs (SS-MO, gray) to that on inflammatory MOs (Infl-MO, red) and cDCs (green) in dLNs 24 hours after CpG administration. Each point represents an independent LN. All data represent at least two independent experiments.

Antigen presentation and initiation of T cell priming by repositioned Res cDCs

We next studied the functional roles of Res cDCs and MOs in the generation of adaptive immunity. Considering that Res cDC2s specialize in MHC-II presentation and MOs have delayed kinetics of MHC-II expression (fig. S4, F to H), we hypothesized that early antigen presentation was not equivalent between these populations. To test this, mice were immunized with CpG plus a fusion protein composed of green fluorescent protein and amino acids of the I-$E^{d}\alpha$ MHC II subunit (EαGFP), which allows detection of antigen uptake via GFP fluorescence and Eα peptide–MHC-II complex using the YAe antibody[121]. One day after immunization, Res cDC2s and migratory cDC2s were the dominant cell types that captured and presented antigen (Fig. 4A). Although some MOs had detectable GFP fluorescence, they did not stain positive with the YAe antibody, indicating minimal MHC-II antigen processing (Fig. 4A). Similar results were seen 2 days after immunization (fig. S5A). A minor fraction of $CD64^{+}$ $GFP^{+}YAe^{+}$ cells was observed (fig. S5A), albeit these cells were phenotypically distinct from inflammatory MOs, expressing lower levels of Ly6C and higher levels of MHC-II (fig. S5A). A similar population was found in steady-state LNs, and their numbers demonstrated a much more modest increase after vaccination as

compared with the Ly6C^{HI} MOs (fig. S5B), indicating that they are distinct from inflammatory MOs and may represent tissue-derived cells or inflammatory cDCs[96,99,127,128]. These results indicated that cDCs, but not the early-recruited inflammatory MOs, were the dominant antigen presenting cells in dLNs after type I agonist immunization.

To test how the repositioning of antigen-presenting Res cDCs influences T cell activation, we adoptively transferred 1×10^6 naïve, ovalbumin (OVA)–specific CD4 OT-II T cells into DC-WT or DC-CCR7.KO mixed BMCs and immunized these mice with OVA plus CpG. dLNs were analyzed 1.5 to 1.75 days after, just before extensive T cell proliferation. Although migratory cDCs presented antigens on MHC (Fig. 4A and fig. S5A), removal of the immunization site 1 to 2 hours after vaccination recapitulated previous findings that migratory cDCs were largely dispensable for CD4 T cell responses (Fig. 4B). Nevertheless, we performed site removal in all animals, as this restricted effects of CCR7 deficiency to intranodal Res cDC repositioning and minimized additional changes in migratory cDC trafficking. As expected, OT-II T cells in DC-WT animals were robustly activated, as demonstrated by T cell clustering, enlarged cell volume, as well as interferon regulatory factor 4 (IRF4) and Ki67 expression, indicating TCR engagement and proliferation, respectively (Fig. 4, C to E)[129,130]. In contrast, early OT-II T cell activation was drastically impaired in the DC-CCR7.KO mice (Fig. 4, C to E). DC-CCR7.KO mice also elicited substantially reduced clonal expansion of OT-II T cells 4 days after immunization, when using a more physiological (10^5) cell transfer number (Fig. 4F). Although the numbers of expanded T cells were markedly different between DC-WT and DC-CCR7.KO mice, there were no major differences in their expression of T-box transcription factor (Tbet) or B cell lymphoma 6 (BCL6) or in their ability to produce interferon-γ (IFNγ) after restimulation (Fig. 4G and fig. S5C). This indicated that the few CD4 T cells that were activated in the DC-CCR7.KO settings underwent

relatively normal effector differentiation, albeit additional differences cannot be ruled out. We also examined polyclonal CD4 T cell responses by immunizing mice with lymphocytic choriomeningitis virus (LCMV)–derived recombinant glycoprotein complex (GPC) and CpG. Seven days after immunization and site removal, large numbers of GPC MHC-II tetramer positive $CD44^+$ CD4 T cells were detected in DC-WT but not DC-CCR7.KO mice (Fig. 4H). T cells in both expressed equivalent levels of Tbet and Gata binding protein 3 (Gata3) proteins (Fig. 4I).

Given that the Res cDC1 also up-regulated CCR7 to move into the deep TZ (Figs. 1 and 2), and these cells specialize in cross-presentation, we also examined CD8 T cell priming using OVA-specific CD8 OT-I T cells. Site removal again did not affect CD8 T cell expansion, indicating minimal contribution of migratory cDCs (fig. S5D). Similar to CD4 T cells, we observed a drastic reduction in OT-I T cell clustering and expression of activation markers in DC-CCR7.KO animals 1.5 days after immunization (fig. S5, E and F). A significant reduction in OT-I T cell expansion in DC-CCR7.KOs was also observed 4 days after immunization (fig. S5G). The few responding OT-I T cells in DC-CCR7.KO mice again displayed no major differences in expression of Tbet and T cell factor 1 (TCF1) nor in their ability to produce IFNγ after restimulation (fig. S5H). Together, these data demonstrated that CCR7-mediated relocalization of both Res cDC2s and cDC1s into the TZ during type I inflammation controls the activation and clonal expansion of both CD4 and CD8 T cells.

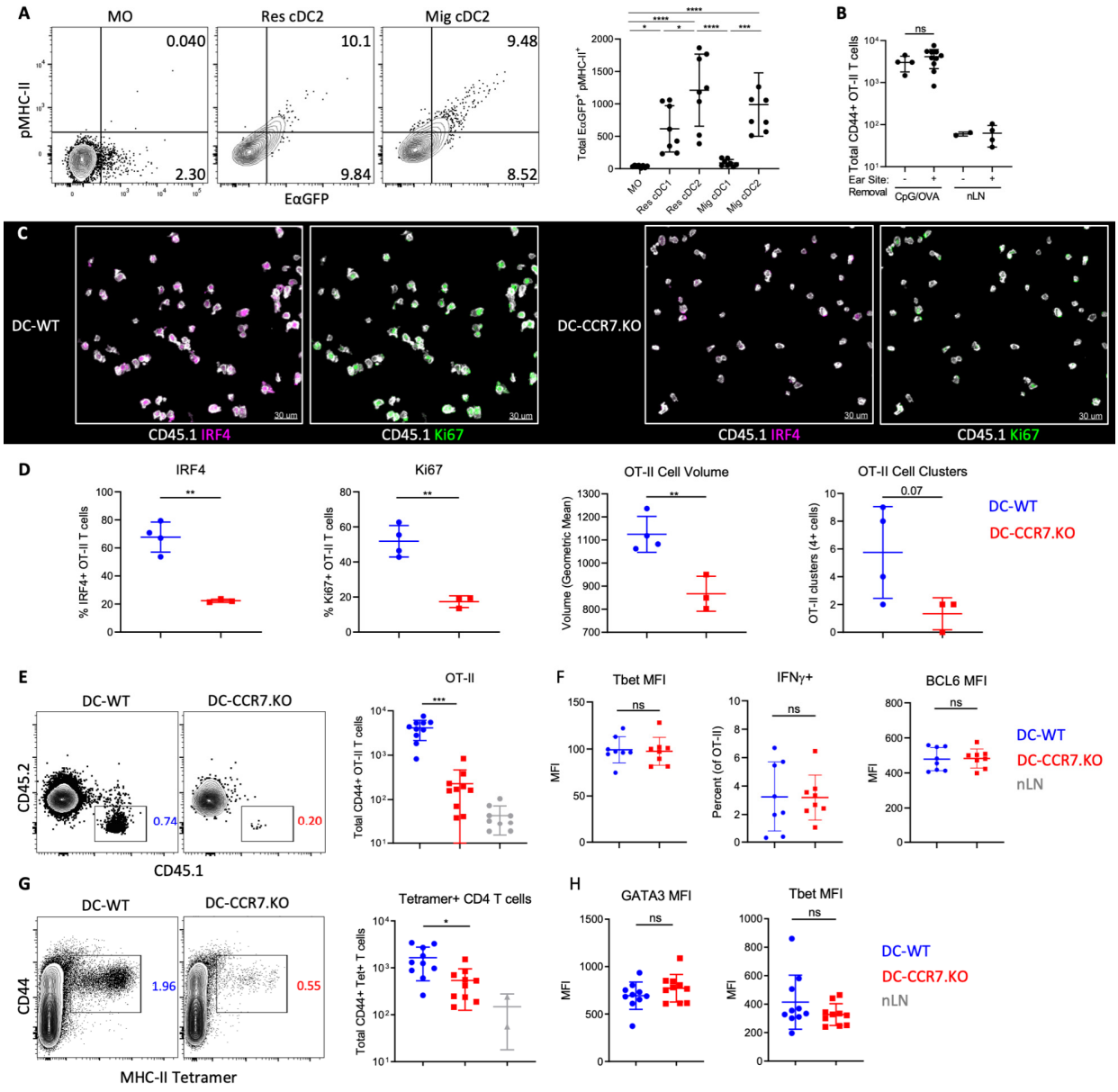

Fig. 4. Induction of T cell priming and clonal expansion via Res cDC repositioning.
(**A**) B6 mice were immunized with CpG plus EαGFP in both ears and analyzed by flow cytometry for GFP fluorescence and peptide–MHC-II staining (YAe) 1 day later. Data analyzed by one-way ANOVA with Tukey's multiple comparison test. (**B**) DC-WT mixed BMCs were transferred with 10^5 OT-II T cells and 1 day later, ears were immunized with OVA plus CpG. Some mice also had site removal 1 to 2 hours later. Four days after immunization, LNs were analyzed by flow cytometry for T cell cellularity. (**C** to **G**) DC-WT and DC-CCR7.KO mixed BMCs were transferred with (C to E) 10^6 or (F and G) 10^5 OT-II T cells, treated with DT, immunized with OVA plus CpG in both ears, and had site removal. dLNs were assessed (C to E) 1.5 days later by histocytometry or (F and G) 4 days later by flow cytometry. (C) Representative areas in the TZ, with the presented IRF4 and Ki67 signal masked outside of CD45.1$^+$ OT-II T cells for visual clarity. (D) Representative gating and (E) quantification of OT-II T cell expression of IRF4 and Ki67, as well as average T cell volume and number of OT-II clusters (>4 cells in direct contact) per section. (F) Total CD44$^+$ OT-II T cells and (G) Tbet and Bcl6 geometric MFI and percentage of IFNγ$^+$ after

restimulation. (**H** and **I**) DT-treated DC-CCR7.KO and DC-WT mixed BMCs were immunized with GPC plus CpG in the ear, followed by site removal 2 hours later. (H) Cellularity and (I) differentiation of CD44$^+$ GPC-tetramer binding T cells were quantified in dLNs 7 days after immunization. (B and E to I) Data analyzed by unpaired *t* test with Welch's correction. Data represent at least two independent experiments.

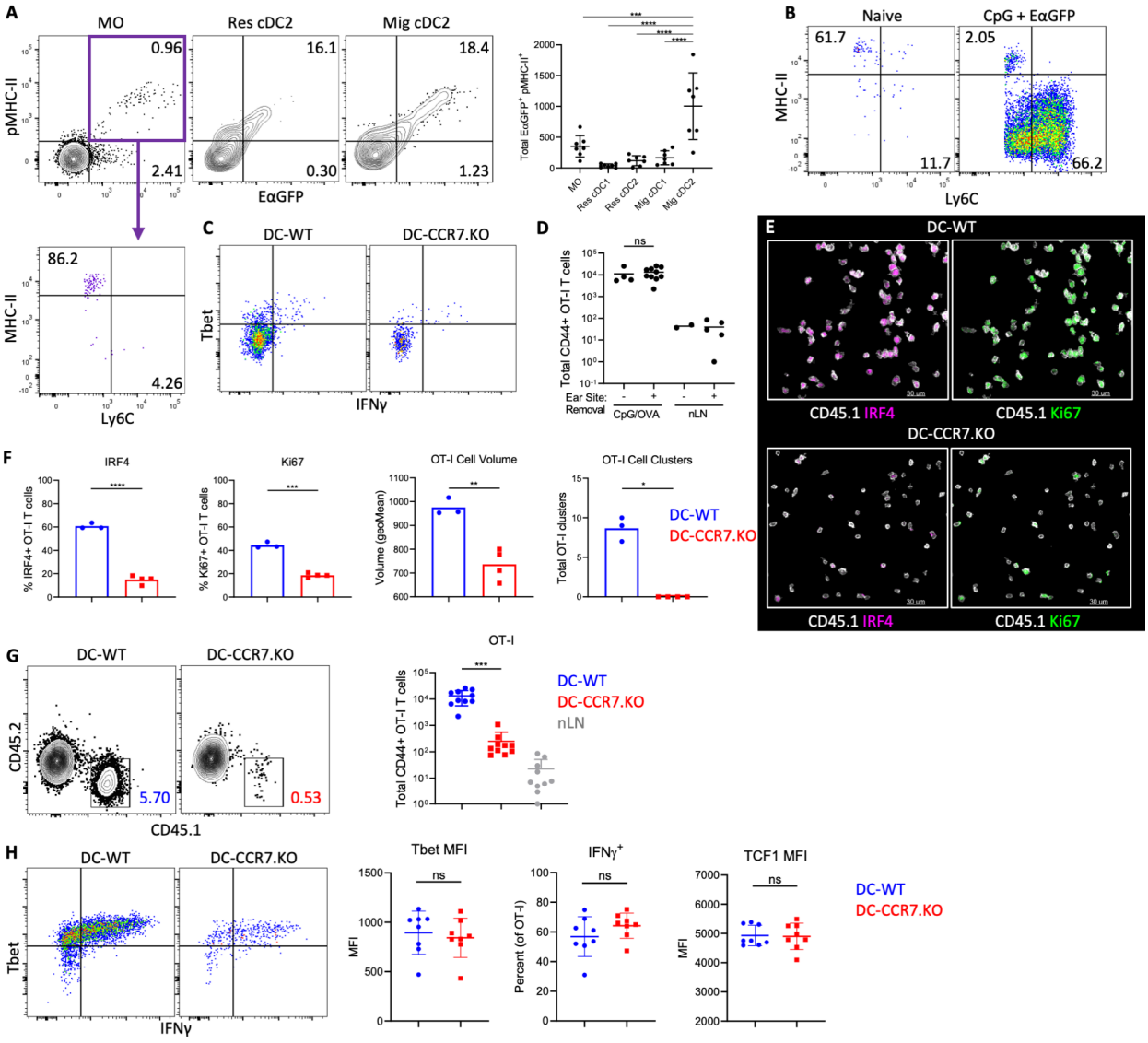

Fig. S5. Res cDC relocalization and antigen presentation in the regulation of CD8 T cell responses. (**A** and **B**) B6 mice were immunized with CpG plus EαGFP in the ears. GFP fluorescence and surface peptide–MHC-II staining (YAe) were analyzed by flow cytometry 2 days later. (A) Representative flow cytometry plots (left) and quantification of total EαGFP$^+$ peptide-MHC-II$^+$ myeloid cells in dLNs (right). Data analyzed by one-way ANOVA with Tukey's multiple comparison test. (B) Representative flow plots demonstrating presence of Ly6C^{LO}MHC-II^{HI} CD64$^+$CD11b$^+$ cells in naïve versus CpG-immunized LNs. MOs were gated on CD3$^-$CD19$^-$NK1.1$^-$Ly6G$^-$Ly6C$^+$CD64$^+$CD11b$^+$ cells. (**C**) Supplementary material for Fig. 4G. Representative flow plots demonstrating staining for Tbet and IFNγ on restimulated OT-II CD4 T cells, 4 days after OVA plus CpG immunization. (**D**) DC-WT mixed BMCs were transferred with 5 x 10^4 OT-I CD8 T cells and immunized with OVA plus CpG in the ears 1 day later. Some mice also had site

removal 1 to 2 hours later. Four days after immunization, dLNs and non-draining LNs (nLN) were analyzed by flow cytometry for T cell cellularity. (**E** to **H**) DC-CCR7.KO and DC-WT mixed BMCs were transferred with (E and F) 10^6 or (G and H) 5 x 10^4 OT-I CD8 T cells, treated with DT, immunized with OVA plus CpG, and had site removal. dLNs were assessed (E and F) 1.5 days later by histocytometry or (G and H) 4 days later by flow cytometry. (E) Representative areas in the TZ are shown, with the presented IRF4 and Ki67 signal first masked outside of CD45.1$^+$ OT-I T cells for visual clarity. (F) Histocytometry quantification of OT-I T cell expression of IRF4 and Ki67, as well as the average T cell volume and the number of detected OT-I clusters (defined as >4 cells in direct contact) per imaged section. (G) Flow cytometry analysis of total CD44$^+$ OT-I T cells, as well as (H) Tbet geometric MFI, percent IFNγ^+, and TCF1 geometric MFI after restimulation. (D and F to H) Data was analyzed by unpaired *t* test with Welch's correction. Each point represents an independent LN. All data represent at least two independent experiments.

Production of IL-12 by TZ-localized MOs during type I inflammation

Activated MOs can express inflammatory cytokines, such as IL-12, although where in LNs MOs generate this cytokine and whether this coincides with early T cell differentiation are not known[93,94,131]. To this end, we first looked for expression of IL-12p40 by various myeloid cell subsets using flow cytometry, as verified using IL-12.KO BMC mice (Fig. S6, A and B). We found that 1 day after CpG immunization, some of the MOs produced copious quantities of IL-12p40 and this became more apparent on day 2 (Fig. 5, A and B, and fig. S6, A to C). As previously described, migratory and Res cDC1 cells also produced large amounts of IL-12p40[132-134]. Although the frequency of IL-12–positive MOs was relatively modest compared with cDCs, due to substantial increases in cellularity, MOs represented the most numerically dominant IL-12–producing cell type within the dLNs.

We next used histocytometry to visualize where IL-12 producing cells were located. IL-12p40 staining, as verified using IL-12.KO BMC mice, was detectable in small quantities in steady-state LNs, primarily associated with migratory cDC1 and some Res cDC1 (fig. S6, D and E), as described[135,136]. A substantial increase in MO-associated IL-12p40 signal was observed in dLNs 1.75 days after CpG immunization and was localized within the TZ (Fig. 5C and D, and fig. S6E). The frequency of IL-12p40–positive cells appeared higher by imaging versus flow

cytometry. This may represent difficulties in cellular extraction, potential cell death, or degranulation during enzymatic tissue digestion for flow cytometry[26,137,138]. Quantification of the imaging data revealed that MOs were a dominant IL-12p40–producing cell population in the TZ after immunization with multiple TLR agonists and after West Nile virus infection (Fig. 5, E to G). Blockade of MO trafficking with anti-CCR2 resulted in substantial loss of MO-derived, but not cDC-derived, IL-12p40 in the TZ (Fig. 5H). In contrast, little MO-associated IL-12p40 signal was seen within the TZ during Type-II inflammation (fig. S6F). Because IL-12p40 does not necessarily reflect the immunologically relevant IL-12p70 (IL-12p40 and IL-12p35 heterodimer), we examined IL-12p70 levels within dLNs in the presence or absence of MOs with enzyme-linked immunosorbent assay (ELISA). IL-12p70 was markedly increased 2 days after CpG immunization, reflective of adjuvant induced inflammation (fig. S6G). Blockade of MO trafficking led to a partial and highly significant decrease in IL-12p70 signal (Fig. 5I and fig. S6G). Collectively, these data indicated that in addition to the conventional contributions by cDCs, MOs provide a substantial source of IL-12p70 in the TZ of dLNs during type I inflammation.

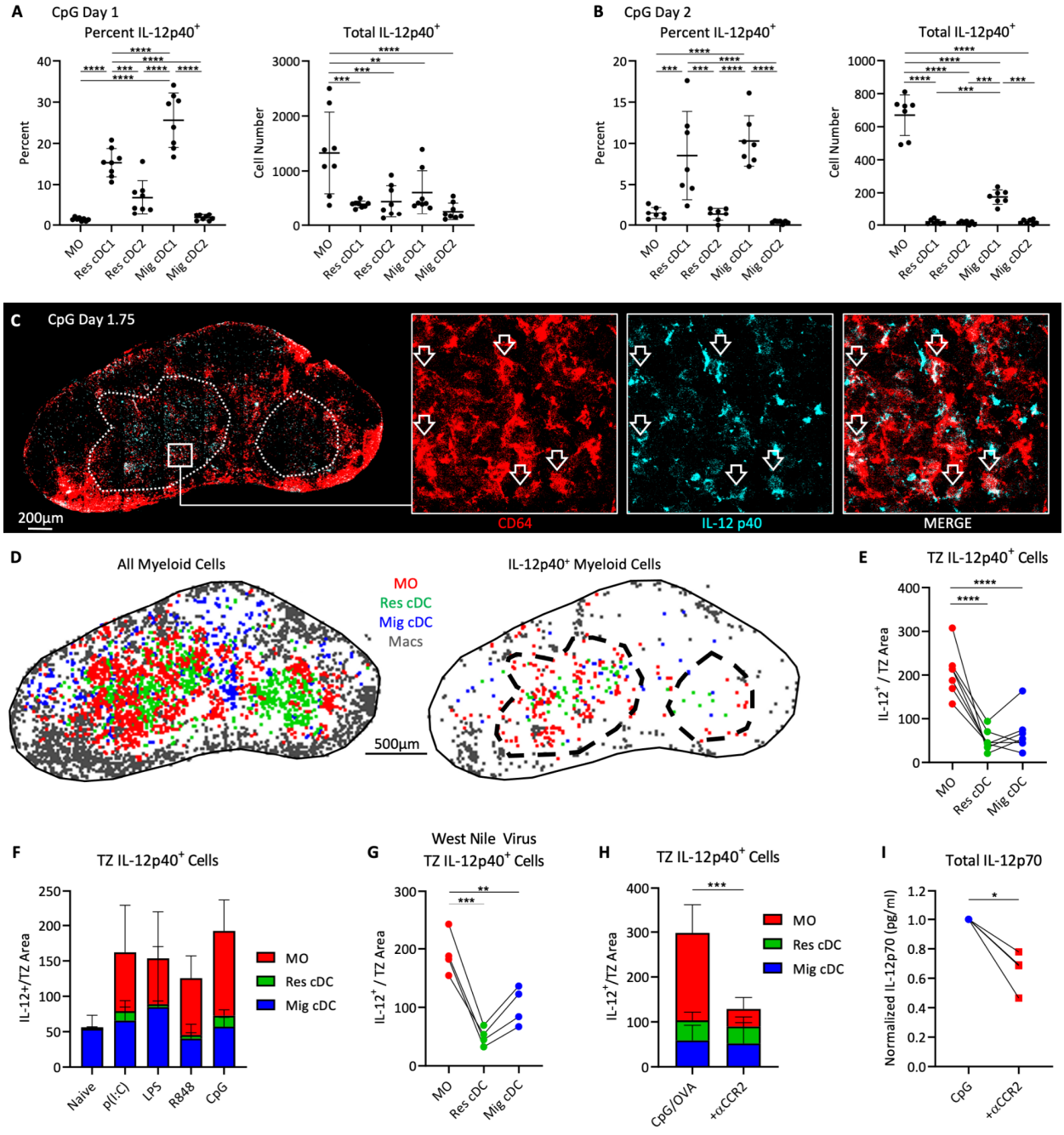

Fig. 5. IL-12 production by TZ-localized inflammatory MOs.
(**A** and **B**) B6 mice were given CpG plus EαGFP in both ears and dLNs were analyzed (A) 1 day or (B) 2 days later by flow cytometry. Percent IL-12p40$^+$ (left) and total IL-12p40$^+$ cells (right) is shown. (**C** to **E**) OT-I–transferred B6 mice were immunized with CpG plus OVA in ears and footpads. dLNs were analyzed by histocytometry 1.75 days later. (C) Representative images demonstrating IL-12p40–expressing CD64$^+$ MOs (arrows) and (D) positional analysis of all myeloid cells (left) and IL-12p40$^+$ myeloid cells (right). Dashed line demarcates the TZ. (E) Quantification of total IL-12p40$^+$ cells within the TZ for the indicated subsets. (**F**) OT-I–transferred B6 mice were immunized with indicated adjuvants plus OVA. dLNs were analyzed 1.5 days later by histocytometry for total IL-12p40$^+$ myeloid cells within the TZ. For each group,

n = 3 to 6. (**G**) B6 mice were infected in the footpad with 100 PFU of West Nile virus-TX. dLNs were analyzed by histocytometry 24 hours later for total IL-12p40^{+} cells within the TZ. (**H**) OT-I–transferred B6 mice were immunized with CpG plus OVA in ears and footpads. Some mice were also treated with αCCR2. Histocytometry analysis of total IL-12p40^{+} cells within the TZ of dLNs 1.75 days after immunization. (I) B6 mice were immunized with CpG in ears and footpads, and dLNs were harvested 2 days later. Some mice were treated with αCCR2. ELISA quantification of total IL-12p70 signal in dLNs. Data analyzed via paired *t* test with Welch's correction. Individual points represent means from four independent experiments. Lines connect experimental means, with the αCCR2 group normalized to the CpG group. Data in (A), (B), (E), and (G) analyzed by one-way ANOVA and Tukey's multiple comparisons test. Linked points in (E) and (G) indicate data from the same LNs. All data represent at least two independent experiments.

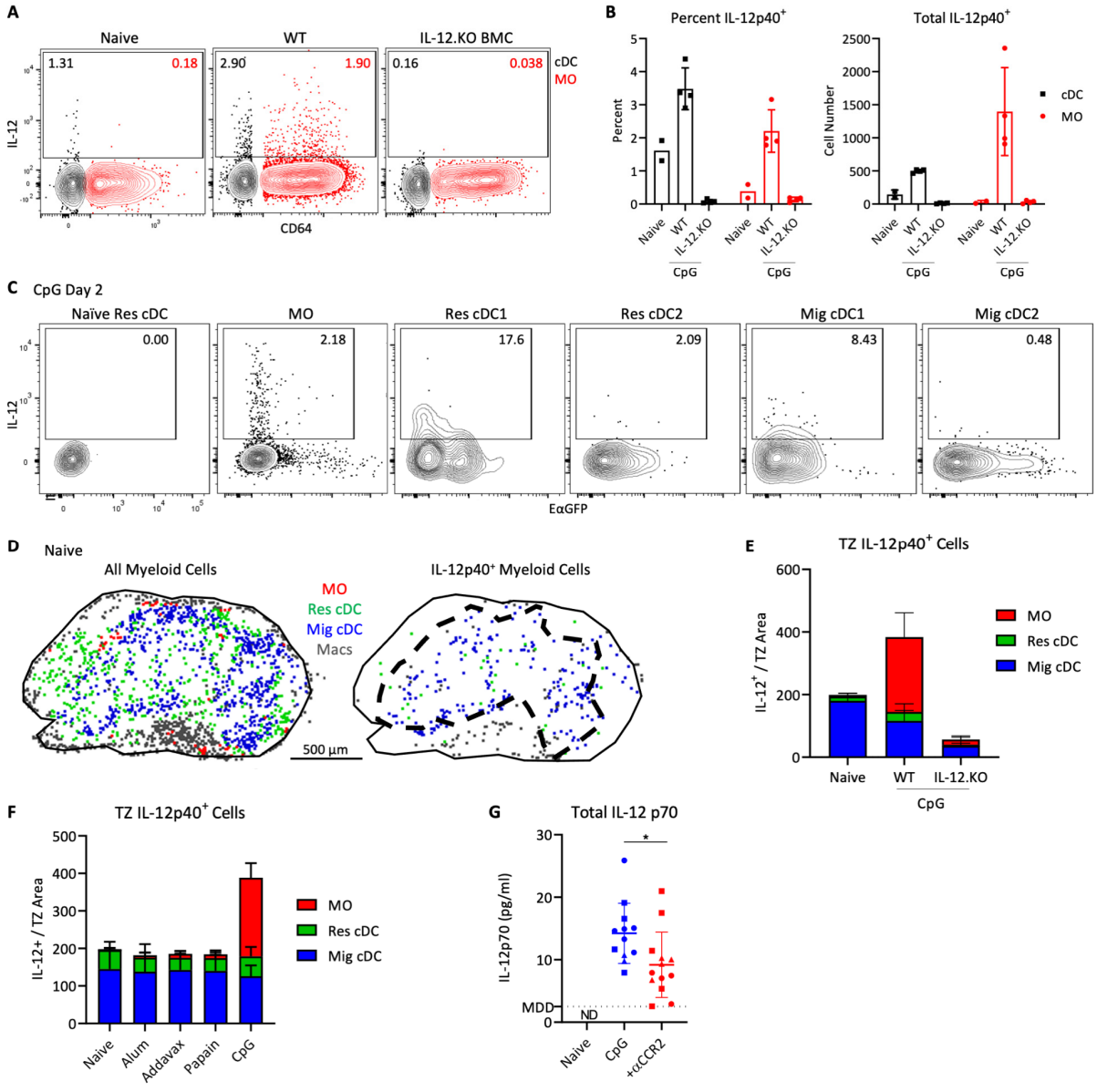

Fig. S6: IL-12 production by TZ-localized inflammatory MOs after immunization.
(**A** and **B**) B6 mice and IL-12p40.KO BMCs were administered CpG in the footpads and 2 days later, dLNs were analyzed by flow cytometry. (A) Representative flow plots and (B) quantification of IL-12p40

expression by MOs and cDCs is shown. (**C**) Representative flow plots for experiment described in Fig. 5B, showing IL-12p40 expression by the indicated myeloid cell subsets 2 days after CpG plus EαGFP immunization. (**D**) Representative histocytometry positional analysis of all myeloid cells (left) and IL-12p40$^+$ myeloid cells (right) within a naïve LN. Macs, macrophages. (**E**) B6 mice and IL-12p40.KO BMCs were injected with CpG in the ears and 2 days later dLNs were analyzed for total IL-12p40$^+$ myeloid cells within the TZ by histocytometry. For each group, n = 4. (**F**) B6 mice were injected with the indicated adjuvants in the ears and footpads. Total IL-12p40$^+$ myeloid cells within the TZ was assessed by histocytometry 1.75 days later. For each group, n = 5 to 7. (**G**) B6 mice were administered CpG in the ears and footpads. Some mice were also treated with αCCR2. Two days later, total IL-12p70 signal in dLNs was measured by ELISA. ELISA data from multiple independent experimental repeats were pooled together, as indicated with different symbols. Data analyzed by unpaired *t* test with Welch's correction. All data represent at least two independent experiments.

Association of early effector T cells with MO-rich LN microenvironments

IL-12 plays a critical role in T cell differentiation[139,140]. Given the spatiotemporal coalescence of antigen-presenting Res cDCs and IL-12 expressing MOs in the TZ of dLNs, we hypothesized that both cell types may functionally cooperate to modulate effector T cell responses. Supporting this notion, 1.5 to 1.75 days after OVA plus CpG immunization, we observed large numbers of activated OT-I and OT-II T cells embedded within a dense, interwoven network of both Res cDCs and CD11c-expressing CD64$^+$ MOs (fig. S7, A and B). To quantify these observations, we calculated the spatial correlation of different immune cells with respect to one another using CytoMAP[29]. Use of 30-μm radius spatial neighborhoods for this also accommodated for potential effects of cellular motility or cytokine diffusion which may occur at these time points[141]. This analysis confirmed that the spatial distribution of activated OT-I and OT-II T cells was positively correlated with the location of both Res cDC and MOs, but not migratory cDCs or macrophages (fig. S7, C and D), indicating preferential cell-cell interactions. The positive spatial correlation of activated T cells with Res cDC was reduced in DC-CCR7.KO mixed BMCs as compared with the DC-WT counterparts, reflective of poor Res cDC repositioning in these settings (fig. S7E). In contrast, OT-I T cells still maintained a positive correlation with MOs in DC-

CCR7.KOs (fig. S7E), corroborating the findings that MOs still efficiently entered the T zone irrespective of Res cDC relocalization (fig. S3G).

A closer examination of dLNs across multiple experiments also revealed a nonuniform, polarized distribution of MOs across the tissues, being particularly noticeable at later time points and in larger, bilobular auricular and brachial dLNs (Figs. 1A, 5, C and D, and 6A, and figs. S2I and S7A). In contrast to MOs, both lobes in these polarized dLNs displayed a more homogeneous centralization of Res cDCs. The polarization of MOs likely corresponds to nonuniform TLR agonist biodistribution and inflammation across the dLNs after afferent drainage[13]. We hypothesized that this myeloid heterogeneity could affect the local signals that T cells encounter during priming. To investigate this, we analyzed the expression of various markers associated with effector differentiation in responding OT-I T cells in relation to the different myeloid populations (Fig. 6A). Considerable heterogeneity in expression of Tbet, TCF1, and CD25 by the activated ($Ki67^+$) OT-I T cells was noted, suggesting early bifurcation of responses (Fig. 6, A and B). We observed distinct spatial distribution patterns for the early effector subpopulations, with the more differentiated $Tbet^+TCF1^-CD25^+$ OT-I T cells preferentially localizing in regions heavily infiltrated by MOs, and with the less differentiated $Tbet^-TCF1^+$ OT-I T cells predominantly distributed in areas with more Res cDCs and fewer MOs (Fig. 6C). Correlation analysis of multiple tissues confirmed these observations, demonstrating that the more differentiated effector OT-I T cells ($Tbet^+TCF1^-$) were spatially correlated with (i.e., more proximal to) MOs, whereas the less differentiated T cells ($Tbet^-TCF1^+$) were correlated with both MOs and Res cDCs (fig. S7F). We examined the relative myeloid cell composition within regions that were dominantly populated by either the $Tbet^+TCF1^-$ or $Tbet^-TCF1^+$ OT-I T cells (fig. S7G). Examination of larger regions also further accommodated for effects of T cell motility across the tissues. Although MOs and Res

cDCs, and in particular cDC1s, were found in relatively equal proportions in Tbet^{-}TCF1^{+} OT-I regions, MOs greatly outnumbered other myeloid cells in regions populated by Tbet^{+}TCF1^{-} early effector T cells (Fig. 6D and fig. S7H). There was no difference between the regions in the frequency of OT-I T cells expressing IRF4 and phosphorylation of the S6 ribosomal protein (pS6), suggesting that early TCR engagement was more homogenous across the compartments (Fig. 6E and fig. S7I). Polarized distribution of Tbet^{+}TCF1^{-} and Tbet^{-}TCF1^{+} OT-I T cells was also observed at later time points, when T cells begin to undergo extensive proliferation and start to leave the tissues (fig. S7J). In addition, we found a similar spatial heterogeneity of OT-I effector cells after administration of OVA plus p(I:C), with marked segregation of Tbet^{HI} and Tbet^{LO} T cells across the polarized dLNs (Fig. 6F). Tbet^{HI} regions were again dominantly populated by MOs, whereas the Tbet^{LO} regions were more equally populated by cDCs and MOs (Fig. 6, G and H). Collectively, these data indicate that distinct myeloid microenvironments in dLNs, as determined by the local density of MOs, are associated with distinct patterns of CD8 T cell effector differentiation.

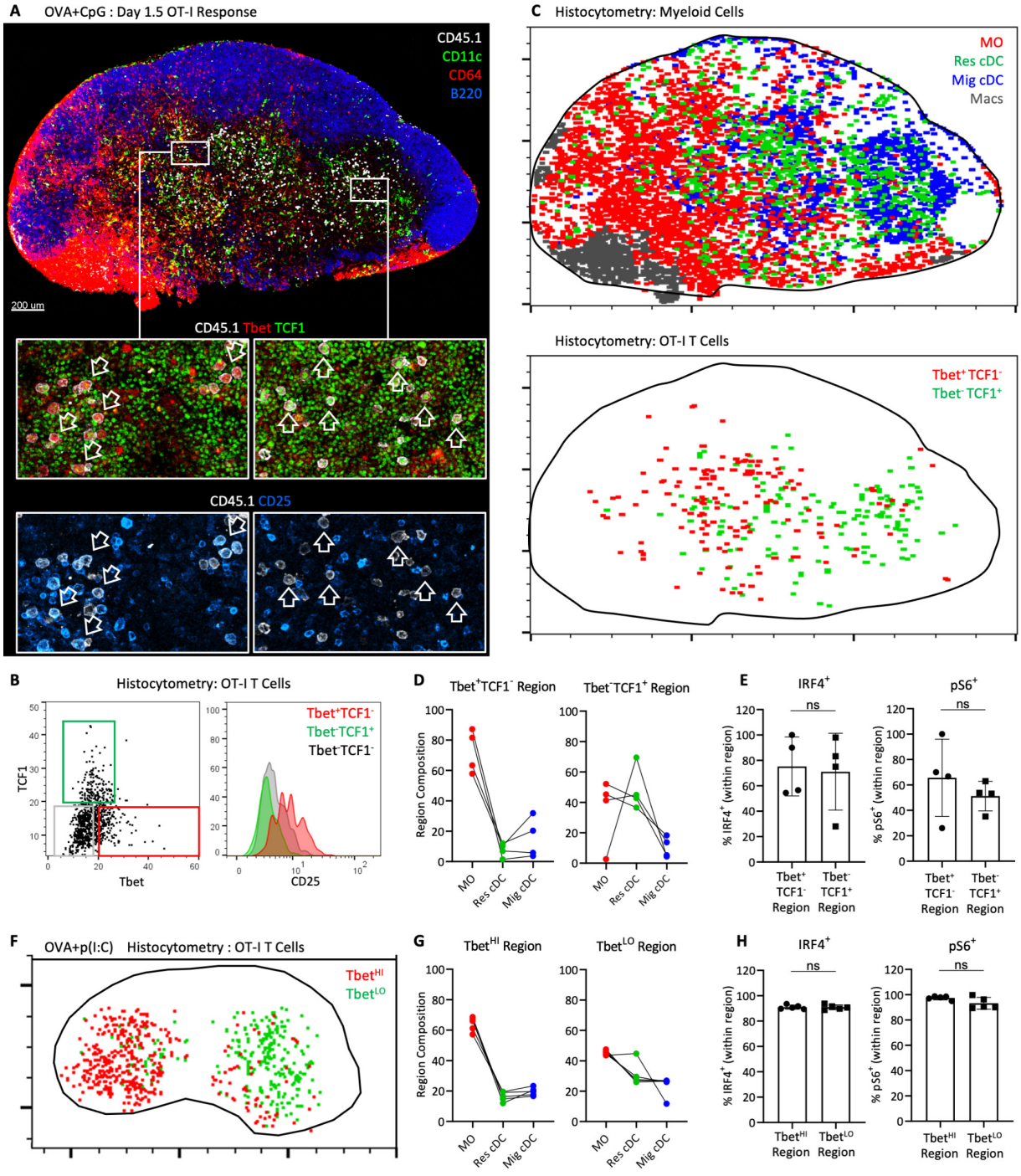

Fig. 6. Regulation of T cell response heterogeneity by myeloid cell microenvironments.
(**A** to **H**) B6 mice were transferred with 10^6 OT-I T cells and immunized with (A to E) OVA plus CpG in ears and footpads or (F to H) OVA plus p(I:C) in ears. Auricular and brachial dLNs were analyzed 1.5 to 1.75 days later by histocytometry. (A) Representative dLN image demonstrating staining for various myeloid cells (top) and markers of T cell differentiation (bottom). Left versus right zoom-in panels demonstrate differential staining of CD45.1$^+$ OT-I cells for Tbet, TCF1, and CD25. (B) Representative histocytometry gating of OT-I cells based on Tbet and TCF1 expression, and the corresponding CD25 expression. (C) Histocytometry analysis of the image from (A), showing the distribution of myeloid cell

populations (top) or OT-I cell subsets (bottom). (D to E) dLNs were subdivided into regions dominantly associated with either Tbet^{+}TCF1^{-} or Tbet^{-}TCF1^{+} Ki67^{+} OT-I T cells (representative spatial gating is shown in fig. S7G). (D) Composition of myeloid cells and (E) percent of IRF4^{+} and pS6^{+} OT-I cells within each region. (F) Representative positional analysis of Tbet^{HI} and Tbet^{LO} Ki67^{+} OT-I cells in dLN after OVA plus p(I:C) immunization. (G to H) dLNs were subdivided into Tbet^{HI} or Tbet^{LO} regions. (G) Composition of myeloid cells and (H) percent of IRF4^{+} and pS6^{+} OT-I cells within each region. Data in (E) and (H) analyzed by unpaired *t* test with Welch's correction. In (D) and (G), linked points indicate data from the same LNs. All data represent at least two independent experiments.

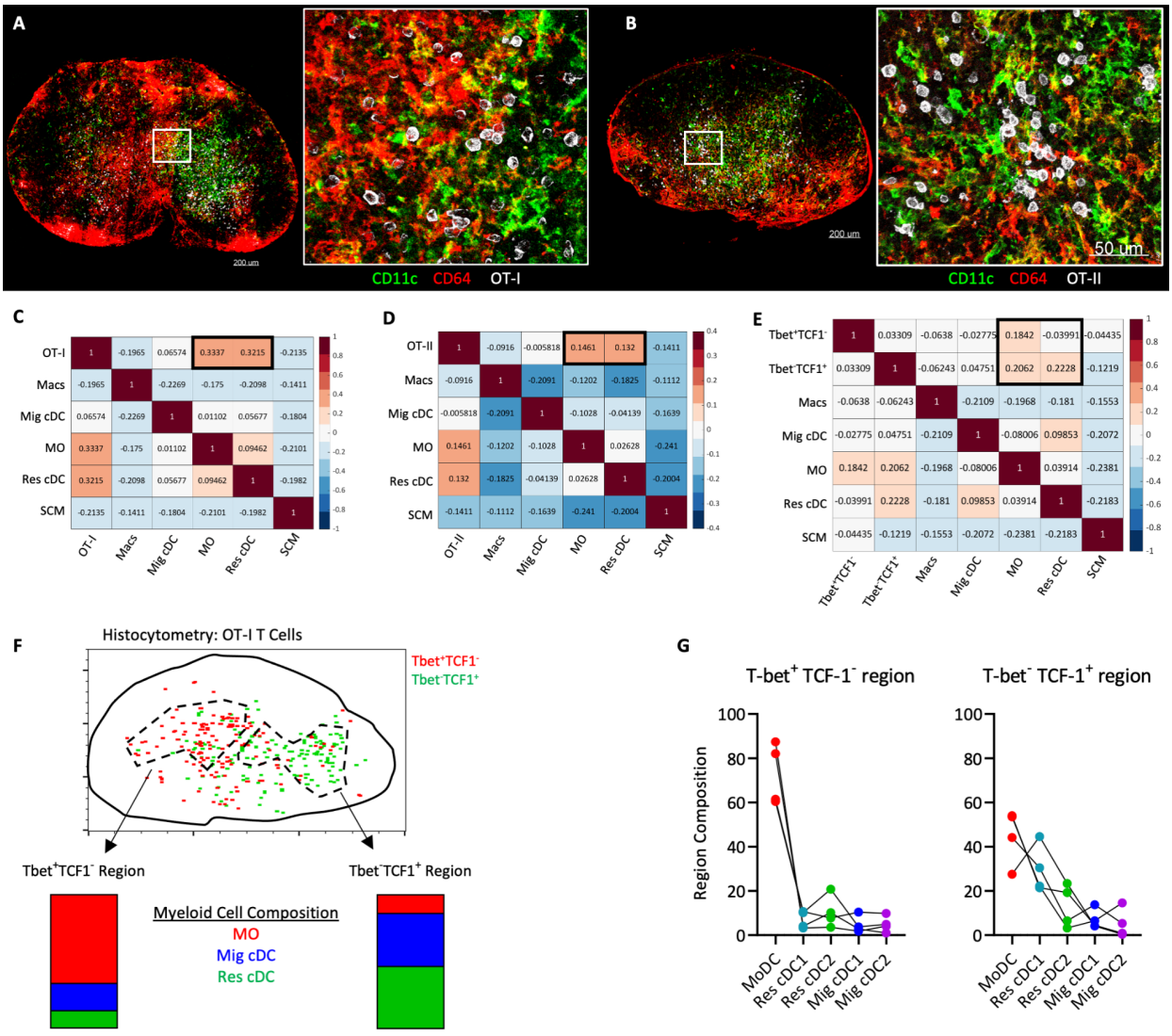

Fig. S7. Myeloid cell microenvironments in the generation of T cell responses.
(**A** to **D**) B6 mice were transferred with (A and C) 10^6 OT-I CD8 T cells or (B and D) 10^6 OT-II CD4 T cells and immunized with OVA plus CpG in ears and footpads 1 day later. Auricular and brachial dLNs were assessed 1.75 days later by imaging and histocytometry. (A and B) Representative image demonstrating the distribution of CD11c and CD64 expressing cells and their proximity to (A) OT-I cells and (B) OT-II cells. (C and D) Heatmaps of the spatial correlations of the indicated myeloid cell populations with respect to (C) OT-I and (D) OT-II T cell positioning. Macs, medullary macrophages; SCM,

subcapsular sinus macrophages. For (C), n = 7 and for (D), n = 8. Positive values indicate spatial colocalization, negative values indicate spatial avoidance. (**E**) Same experimental setup as in fig. S5, E and F. DC-WT and DC-CCR7.KO mixed BMCs were transferred with 10^6 OT-I CD8 T cells, treated with DT, immunized with OVA plus CpG, and had site removal. 1.5 days after immunization, dLNs were analyzed by histocytometry and CytoMAP. Spatial correlations of the indicated cell populations in DC-WT versus DC-CCR7.KO dLNs. Each point represents an independent dLN. (**F**) Same dataset as (C), but with extended analysis of the spatial correlation of $Tbet^+TCF1^-$ versus $Tbet^-TCF1^+$ OT-I T cells with respect to the indicated myeloid cell subsets. (**G**) Representative spatial gating for Fig. 6, demonstrating $Tbet^+TCF1^-$ and $Tbet^-TCF1^+$ OT-I T cell regions for analysis of myeloid cell composition within those respective regions. (**H**) Extended analysis for Fig. 6D, showing the composition of the indicated myeloid cell subsets within the $Tbet^+TCF1^-$ regions and $Tbet^-TCF1^+$ regions. Linked points represent data from the same dLN. (**I**) Supplementary material for Fig 6E, showing representative histocytometry gating of $IRF4^+$ and $pS6^+$ $Ki67^+$ OT-I T cells in $Tbet^+TCF1^-$ and $Tbet^-TCF1^+$ regions. (**J**) B6 mice were transferred with 10^6 OT-I CD8 T cells and immunized with OVA plus CpG in ears and footpads 1 day later. dLNs were analyzed by histocytometry 2 days later. Representative dLN showing the positioning of indicated myeloid cell populations (left) and OT-I subsets (right). All data represent at least two independent experiments.

MO-dependent differentiation of effector T cells

To test the contribution of MOs to CD4 and CD8 T cell responses, we transferred OT-I and OT-II T cells, immunized the mice with OVA plus CpG, and, in some of the animals, also blocked MO recruitment with anti-CCR2. In these experiments, we also injected a higher dose of OVA (10 μg) to provide MOs with maximal opportunity for antigen presentation. Nevertheless, minimal impact of MO blockade was seen on T cell expansion and expression of Ki67, IRF4, or pS6, indicating that MOs play a negligible role in MHC-I and MHC-II antigen presentation (fig. S8, A and B). In contrast, we observed a drastic reduction in the spatial polarization and generation of $Tbet^+TCF1^-$ OT-I cells in dLNs of mice that received CCR2-blocking antibody (Fig. 7A), suggesting a major role for MOs in driving localized effector differentiation of CD8 T cells. Similar decreases in the generation of $Tbet^+$ effector OT-II CD4 T cells were seen after CCR2 blockade (fig. S8B). Reduced CD8 and CD4 T cell differentiation, but not clonal expansion, was also observed on day 4 (Fig. 7, B and C). Similarly, blockade of MO trafficking resulted in marked attenuation in Tbet and CXCR3 expression, as well as IFNγ production upon restimulation by polyclonal GPC-specific CD4 T cells after GPC plus CpG immunization (fig. S8C).

Last, we tested the direct contribution of IL-12 production by MOs using two distinct mixed BMC models. In the former, we reconstituted irradiated B6 recipients with a 50:50 mix of CCR2-DTR BM and either WT or IL-12.KO BM (fig. S8, D and E). Ablation of MOs using DT administration allowed examination of T cell responses in the presence of MOs derived only from either the WT or the IL-12.KO donors. In the latter model, B6 recipients were reconstituted with IL-12.KO BM together with either WT or CCR2.KO BM, which allowed testing the role of MO-derived IL-12 in the absence of DT-mediated cell toxicity or possible off-target effects (Fig. 7, D and E). In both models, no major changes in T cell expansion were observed 4 days after immunization (Fig. 7, D and E, and fig. S8, D and E). In contrast, we observed significantly reduced OT-I and OT-II T cell effector differentiation and IFNγ production upon restimulation, indicating that MO-derived IL-12 directly contributes to effector T cell programming. Similar results were seen for polyclonal T cell responses (fig. S8F), as well as after p(I:C) plus OVA immunization (fig. S8G). Collectively, these findings demonstrated that MOs provided a localized source of IL-12 to T cells to drive optimized effector differentiation during type I inflammation.

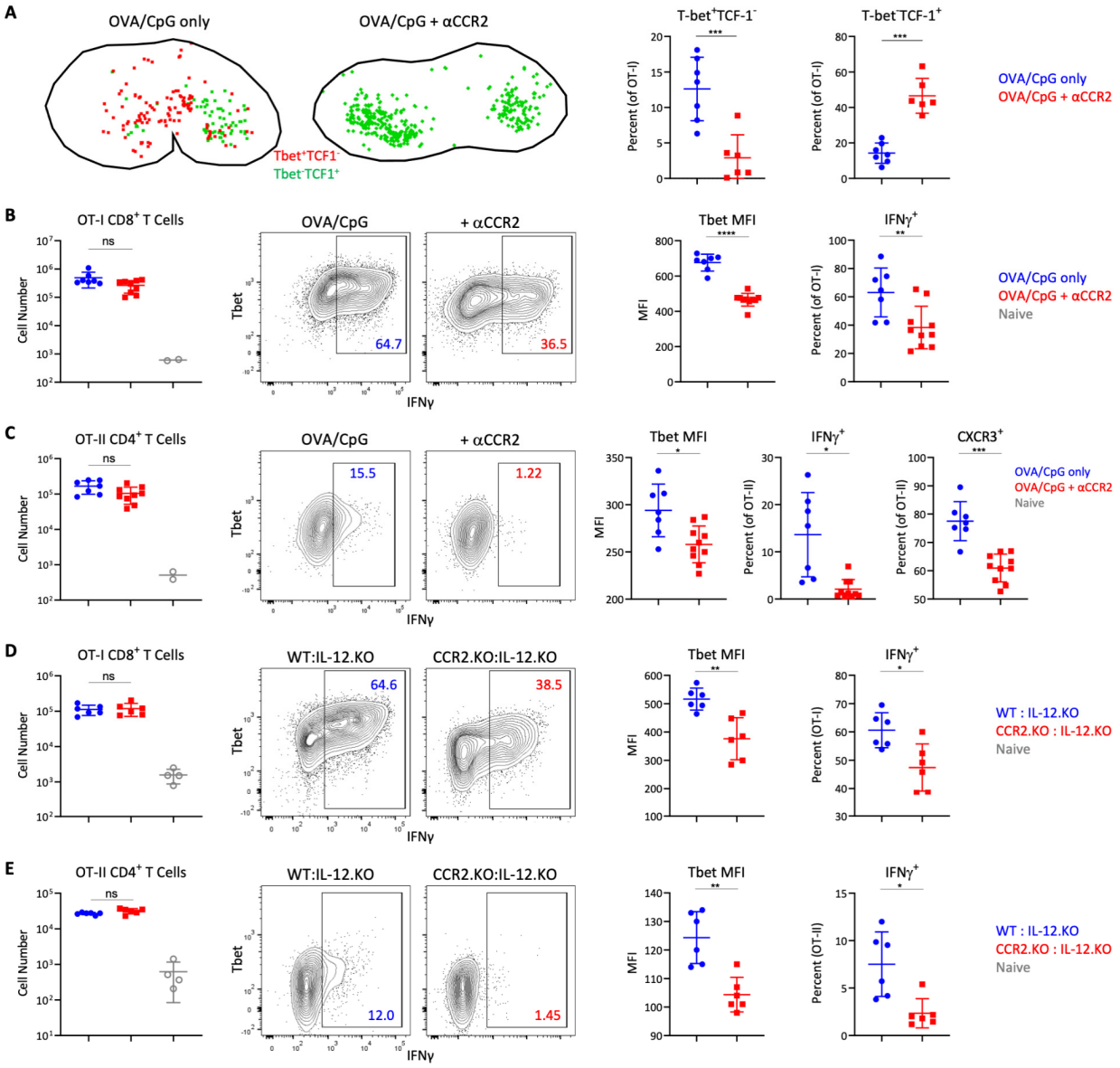

Fig. 7. Optimization of CD4 and CD8 T cell effector differentiation by MOs.
(**A**) B6 mice were transferred with 10^6 OT-I T cells and immunized with OVA plus CpG in ears and footpads. Some animals were treated with αCCR2. dLNs were analyzed 1.75 days later by histocytometry for location (left) and frequency (right) of Tbet$^+$TCF1$^-$ and Tbet$^-$TCF1$^+$ OT-I cells. (**B** and **C**) B6 mice were co-transferred with 10^5 OT-I and OT-II T cells and immunized with OVA plus CpG in the ears. Some mice were treated with αCCR2. dLNs were analyzed 4 days later by flow cytometry. Total CD44$^+$ cells, Tbet geometric MFI, percentage of IFNγ$^+$ T cells after restimulation, and percent CXCR3$^+$ for (B) OT-I and (C) OT-II cells. (**D** and **E**) WT:IL-12p40.KO and CCR2.KO:IL-12p40.KO mixed BMCs were cotransferred with 10^5 OT-I and OT-II T cells and immunized with OVA plus CpG 1 day later. (D) OT-I and (E) OT-II cellularity and differentiation in dLNs was assessed by flow cytometry 4 days later. Data analyzed by unpaired *t* test with Welch's correction. Data represent at least two independent experiments.

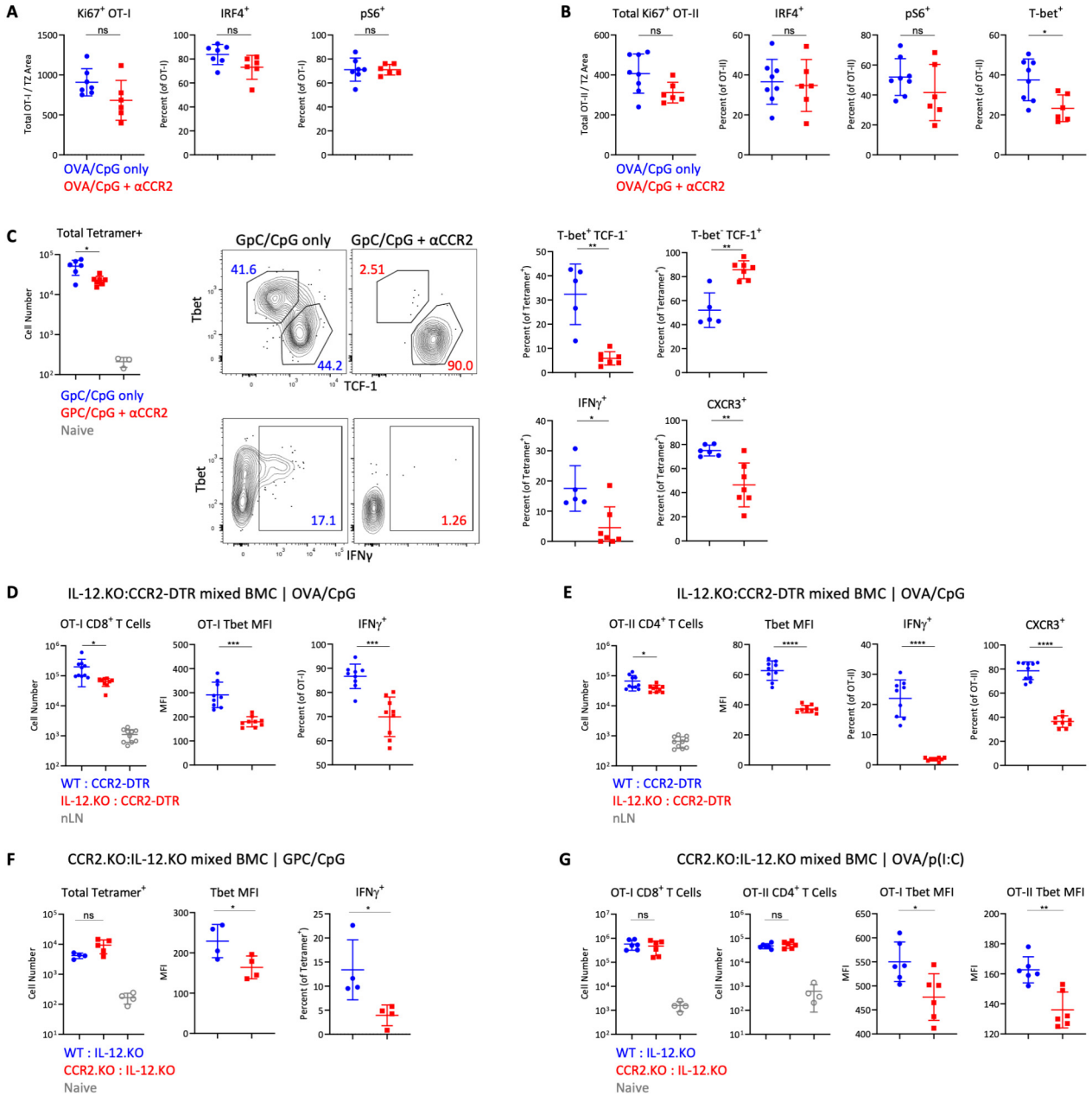

Fig. S8. Regulation of T cell differentiation by inflammatory MOs.
(**A** and **B**) B6 mice were transferred with (A) 10^6 OT-I CD8 T cells or (B) 10^6 OT-II CD4 T cells and immunized with OVA plus CpG in ears and footpads 1 day later. Some mice were also treated with αCCR2. dLNs were analyzed by histocytometry 1.75 days later. Total Ki67$^+$ OT-I or OT-II cells per TZ area, and percent OT-I or OT-II cells expressing the indicated markers is shown. (**C**) B6 mice were immunized with GPC plus OVA in the ear. Some mice were additionally treated with αCCR2. dLNs were assessed by flow cytometry 7 days later. Total number of CD44$^+$ GPC-tetramer$^+$ CD4 T cells was quantified (left). Tbet and TCF1 expression (top), IFNγ production after restimulation (bottom), and percent CXCR3$^+$ (bottom) were also measured. (**D** and **E**) WT:CCR2-DTR and IL-12p40.KO:CCR2-DTR mixed BMCs were cotransferred with 10^5 OT-I CD8 and OT-II CD4 T cells, treated with DT 1 day later, and then immunized with OVA plus CpG the day after. Cellularity and differentiation of CD44$^+$ (D) OT-I and (E) OT-II T cells were analyzed by flow cytometry 4 days later. (**F**) WT:IL-12p40.KO and CCR2.KO:IL-12p40.KO mixed BMCs

were immunized with GPC plus CpG in the ear. Cellularity and differentiation of $CD44^+$ GPC-tetramer$^+$ CD4 T cells was assessed by flow cytometry 7 days later. (**G**) WT:IL-12p40.KO and CCR2.KO:IL-12p40.KO mixed BMCs were cotransferred with 10^5 OT-I CD8 and OT-II CD4 T cells and immunized with OVA plus p(I:C) in the ears. Four days later, dLNs were analyzed by flow cytometry for total number of $CD44^+Ki67^+$ OT-I and OT-II cells, as well as Tbet geometric MFI. All data analyzed by unpaired *t* test with Welch's correction. Each point represents an independent LN. Data represent at least two independent experiments.

2.3 Discussion

Here, we defined several critical features of myeloid cell organization that shape T cell responses during type I but not type II inflammation (fig. S9). We found rapid repositioning of Res cDCs from the LN periphery and concomitant influx of blood-derived inflammatory MOs into the deep TZ of dLNs. The repositioning of Res cDCs allowed for efficient MHC presentation of draining antigens in the appropriate anatomical compartment to elicit early T cell activation and differentiation. MO influx, on the other hand, provided an additional source of signal 3 cytokines to responding T cells, promoting generation of fully differentiated effector responses. Together, these distinct innate cell types functionally cooperated with one another to promote the generation of optimized adaptive immunity. We also found extensive heterogeneity in MO infiltration across the TZ, which generates distinct microenvironments with varied MO and cDC abundance. Priming of T cells within these microenvironments influenced the exposure of T cells to different activating stimuli, such as MO-produced IL-12, and promoted localized generation of different effector subsets. Thus, inflammatory innate microenvironments within dLNs regulated the overall quality and heterogeneity of the resulting T cell responses.

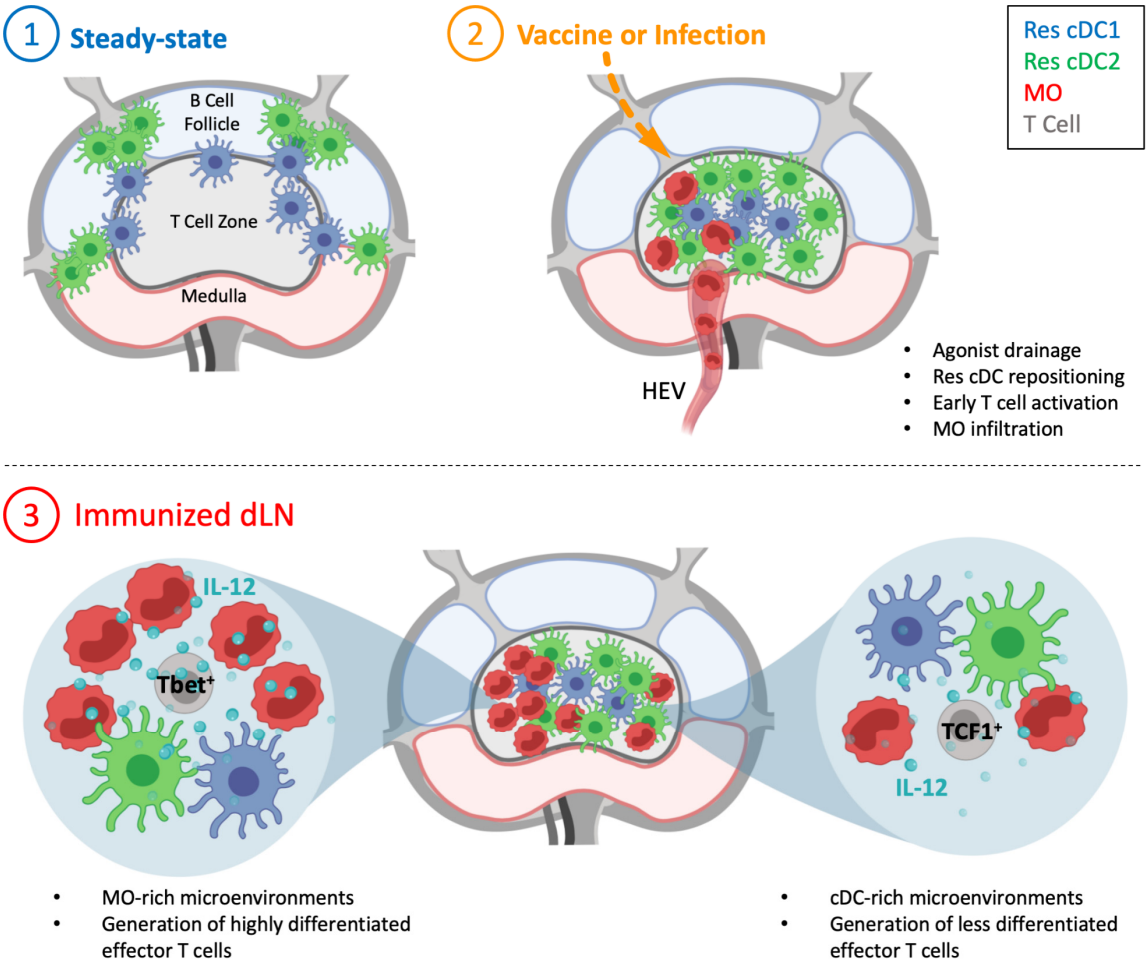

Fig. S9. Model of innate and adaptive immune cell cross-talk during type I inflammation.
(1) Within steady-state LNs, Res cDC are localized in the interfollicular and medullary peripheral regions, promoting robust sampling of draining antigens. **(2)** During type I inflammation, Res cDCs rapidly relocalize from the LN periphery into the deep TZ in a CCR7-mediated fashion to induce early T cell activation. Concurrently, MOs begin to infiltrate the dLNs in large numbers via HEVs and migrate into the TZ, bringing in an additional and substantial source of IL-12 cytokine for effector T cell differentiation. **(3)** MO infiltration is nonuniform across the TZ, leading to heterogeneity in the local abundance of MOs and cDCs, and the generation of MO-rich vs cDC-rich LN microenvironments. These distinct LN microenvironments support divergent T cell programming across the tissue, with the highly differentiated effector T cells primarily being found in the MO-rich regions, and less differentiated T cells predominantly found in areas rich with cDCs and with lower MO abundance.

The finding that LN-Res cDCs respond to inflammatory stimuli and use CCR7 to reposition within the dLNs is consistent with the migration programs of peripheral tissue and splenic cDC subsets[41,72,73,116]. Our data connect these observations, demonstrating that cDCs across multiple different tissues use the CCR7 axis during inflammation for migration into the most proximal T

cell compartments. These observations also highlight caveats in studies using CCR7.KO animals to dissect the role of migratory cDCs, as we showed that the same pathway was used by LN-Res cDCs for intra-nodal repositioning. Similar considerations likely apply to other models in which the migratory capacity of multiple cDC populations may be affected[116,142-144]. Our findings do not argue against the role of migratory cDCs in T cell immunity, as these cells are critical during highly tropic infections[145,146], and for promoting T helper 2 and T follicular helper responses[45,143,147]. Migratory cDCs and pDCs can also cargo antigens to Res cDCs[31,87,88,148-150]. We did not find efficient Res cDC repositioning or MO recruitment in type II inflammatory conditions, supporting the importance of migratory cDCs in these settings. Instead, our observations indicated that in conditions of ample antigen drainage after vaccination or during certain microbial infections, Res cDCs are exceptionally potent at inducing T cell activation[13,27,101,121,151]. A better understanding of the distinct contributions of peripheral versus Res cDC populations in different immunologic settings will aid in vaccine design[152]. Additionally, the responses seen for LN-Res cDC1s, cDC2s and MOs occurred in response to multiple Type-I agonists regardless of TLR expression on these populations[153-155]. This suggests that secondary inflammatory mediators, such as IFN-I or tumor necrosis factor–α, may be involved[122,156-158].

In addition, we provided substantial insight into the organization and role of MOs during type I inflammation. As early as 6 hours after immunization, MOs entered the dLNs, primarily via the local HEVs instead of the afferent lymphatics, and rapidly occupied various LN regions, including the medulla, B cell follicles and parts of the TZ. CCR2 appears critical for this process and it is likely that CCR2 ligands in both the BM and inflamed dLNs are involved[93,98,122]. In contrast, CCR7 was not essential for MO trafficking to the dLNs during inflammation, and if anything, previous studies have reported increased numbers in CCR7.KO mice[93,96]. There was

substantial heterogeneity in MO infiltration across the TZ, likely driven by localized afferent drainage and polarized dispersal of inflammatory stimuli[13]. This heterogeneity generated distinct microenvironments in dLNs which were directly associated with different effector CD8 T cell subtypes, with more differentiated effector T cells primarily observed within MO-rich regions and less differentiated cells found in cDC1-dominated regions with lower MO abundance. Divergent T cell programming appeared to be at least in part MO-derived IL-12 mediated, as blockade of MO trafficking or IL-12 production resulted in loss of effector T cell spatial polarity and reduced differentiation. Thus, MOs generated highly inflammatory microenvironments in LNs to promote the generation of fully differentiated effector T cells in a localized fashion. Our findings do not contradict previous observations that cDC1s can produce IL-12 and promote effector T cell differentiation[132,133,135,136,159,160]. We observed potent IL-12 production by Res and migratory cDC1s, and MO blockade suppressed but did not abolish effector T cell responses. Instead, our data suggested that cDCs provide an early source of IL-12, and this is further amplified by the IL-12 derived from MOs in a localized fashion. Therefore, the collaborative action of both cDCs and MOs was important for optimized generation of adaptive immunity.

Our spatial analysis was largely limited to use of tissue sections from individual time points and tgeneration of effector T cells in MO-rich regions could be, in part, influenced by cellular repositioning after initial priming. This may particularly be true for CD4 T cell responses, which have distinct kinetics of effector programming and additional chemotactic properties as compared with CD8 T cells[74,119,161,162]. Statistical region analysis, as performed here, minimized this issue, but the development of next-generation technologies capable of comprehensive spatiotemporal tracking of T cell fates across entire organs and over time is necessary. In addition, our study did not thoroughly investigate all possible immunologic settings. Whether similar processes occur in

other conditions, such as autoimmunity or cancer, and how distinct myeloid cell microenvironments influence T cell priming remain to be investigated. Our findings do highlight the concept that rational vaccine strategies to simultaneously target multiple innate cell populations, including MOs, should be explored[163,164]. MOs are a highly plastic innate cell population capable of a wide spectrum of functions[165]. Given their abundance and ability to infiltrate most tissues, strategies to modulate MO trafficking and function may prove of value in a variety of settings. In conclusion, our findings revealed fundamental features of innate-adaptive cell cross-talk during type I inflammation, demonstrating that the spatial coordination and functional cooperation of innate cells within dLNs were critical for the generation and shaping of adaptive responses to vaccines and infections.

2.4 Materials and methods

Study design:

The aim of this study was to investigate the role of innate cell LN microenvironments in shaping T cell immunity in mouse models of vaccination and infection. We performed multi-modal analysis with quantitative confocal imaging, intravital two-photon microscopy and flow cytometry to examine the dynamic changes in spatial organization for various myeloid cell populations during inflammation, as well as their association with activated T cells. In vivo adoptive transfer assays, mixed BMC systems, and antibody blocking studies were used to investigate the role of cDCs and MOs in the generation of T cell responses. Detailed methods are described below and in the Supplementary Materials.

Mice:

C57BL/6J, B6.129(Cg)-*Ccr2*$^{tm2.1Ifc}$/J (CCR2-RFP), B6.Cg-Tg(Itgax-Venus)1Mnz/J (CD11c-YFP), B6(Cg)-*Tyr*$^{c-2J}$/J (B6 albino), B6.Cg-*Zbtb46*$^{tm4.1(HBEGF)MnzTyrc-2J}$/J (*Zbtb*46-DTR),

B6.129P2(C)-*Ccr7*^{tm1Rfor}/J (CCR7.KO), B6.129S1-*Il12*^{btm1Jm}/J (IL-12p40.KO), and B6.129S4-*Ccr2*^{tm1Ifc}/J (CCR2.KO) mouse strains were obtained from The Jackson Laboratory. CD45.1^{+} B6.Cg-Tg(TcraTcrb)425Cbn/J (OT-II), CD45.1^{+} C57BL/6-Tg(TcraTcrb)1100Mjb/J (OT-I), and B6.SJL-*Ptprc*^{a}*Pepc*^{b}/BoyCrl (CD45.1^{+}) were obtained either from donating investigators (Dr. P. J. Fink, University of Washington) or Charles River. CD11c-YFP animals were crossed with B6 albino mice to homozygosity and next crossed to CCR2-RFP mice to generate a CD11c-YFP × CCR2-RFP$^{\text{Heterozygous}}$ dual reporter mice. CCR2-DTR mice were obtained from donating investigator (S. F. Ziegler, Benaroya Research Institute) and with approval from the originating investigators (T. M. Hohl and E. G. Pamer, Memorial Sloan-Kettering Cancer Center)[166]. Six to 10 week-old male and female mice were kept in specific pathogen–free conditions at an Association for Assessment and Accreditation of Laboratory Animal Care–accredited animal facility at the University of Washington, South Lake Union campus. All procedures were approved by the University of Washington Institutional Animal Care and Use Committee.

BMCs and adoptive transfers:

For BMCs, C57BL/6 mice were exposed twice to 6 Gy of gamma irradiation from a cesium source separated by a 3-hour rest period and injected with 2×10^6 donor BM cells intravenously the same day. Mice were kept on neomycin for 3 weeks or Baytril for 2 weeks and used experimentally at least 6 weeks after transplant.

For CCR7 BMCs, irradiated recipients were reconstituted with a 50:50 mix of CCR7.KO or C57BL/6 and *Zbtb*46-DTR BM. For IL-12p40.KOs, irradiated recipients were reconstituted with IL-12p40.KO BM. For IL-12p40.KO:CCR2-DTR mixed BMCs, a 50:50 mix of IL-12p40.KO or C57BL/6 and CCR2-DTR BM was used for reconstitution. For CCR2.KO:IL-12p40.KO mixed BMCs, a 50:50 mix of CCR2.KO or C57BL/6 and IL-12p40.KO BM was used

for reconstitution. For CCR7.KO:WT mixed BMCs, irradiated recipients were reconstituted with a 50:50 mix of congenically marked CCR7.KO BM and C57BL/6 BM. In experiments using DTR BMCs, mice were administered with DT in phosphate-buffered saline (PBS) at 20 ng / g bodyweight intraperitoneally every 2 days.

For adoptive transfers, naïve CD45.1$^+$ OT-II or CD45.1$^+$ OT-I T cells were isolated from LNs and spleens using either the naïve CD4+ or CD8+ T cell isolation kits (Miltenyi Biotec), respectively. Average purity of OT-II and OT-I cells was about 75 and 90%, respectively. The indicated number of cells was transferred into CD45.2$^+$ C57BL/6 hosts intravenously.

Immunizations and infections:

The following adjuvants and amounts per immunization site were used: 20 μg of CpG ODN 1668 (AdipoGen), 10 μg of R848 (Invivogen), 10 to 20 μg of poly(I:C) (Amersham), 10 μg of LPS from *E. coli* O111:B4 (Sigma-Aldrich), 20 μg of flagellin (FliC) from *Salmonella enterica* Typhimurium (kind gift from K. D. Smith, University of Washington)[167], Alhydrogel or 'Alum' (Invivogen) diluted 1:2 with PBS, 50 μg of papain (Sigma-Aldrich), and Addavax (Invivogen) diluted 1:2 with PBS. Except for Alum and Addavax, the indicated adjuvants were mixed with PBS (20 μl total volume). All adjuvants were injected in either the front or hind footpads, or intradermally in the ear pinnae (brachial, popliteal, or auricular dLNs, respectively) as indicated. In indicated studies, the immunized ear pinnae were surgically removed 1 to 2 hours after immunization.

In some studies, ~1.2 × 10^7 heat-killed *E. coli* BioParticles (Thermo Fisher Scientific) in 20 μl of PBS were injected into the ear. For West Nile virus infections, 100 plaque forming units (PFU) of West Nile virus (Texas strain) in 20 μl of PBS were injected into the footpad. For *Nippostrongylus brasiliensis* infections, infectious third-stage larvae (L3) were raised and

maintained as described[168]. Mice were infected subcutaneously at the base of the tail (dLN, inguinal) with 500 *Nippostrongylus brasiliensis* L3.

For in vivo antibody blocking studies, 100 μg of anti-CD62L (clone Mel-14, BioXCell) and/or 100 μg of anti–PSGL-1 (clone 4RA10, BioXCell) were injected intraperitoneally at the time of immunization. In some experiments, 20 μg of MC-21 CCR2-blocking antibody (gift from M. Mack, University Hospital Regensburg) was injected intraperitoneally at the time of immunization, and administered daily for up to 3 days after[169]. Intravascular labeling was achieved by injecting 2.5 μg of CD45.2–phycoerythrin (PE) antibody 10 min before animal euthanasia[170]. OVA immunizations used endotoxin-free OVA (InvivoGen), either 1 or 10 μg, as indicated, along with 20 μg of CpG or p(I:C). In some studies, 1 μg of recombinant LCMV preglycoprotein GPC (amino acids 10 to 90) (MyBioSource) along with 20 μg of CpG was injected intradermally in the ear pinnae. For antigen presentation studies, 10 μg of LPS-free EαGFP (gift from M. K. Jenkins, University of Minnesota) plus 20 μg of CpG were injected intradermally in the ear pinnae.

Enzyme-linked immunosorbent assay:

The Mouse IL-12 p70 Quantikine ELISA Kit (R&D Systems) was used on concentrated LN supernatants using the manufacturer's protocol. Detailed methods can be found in the Supplementary Materials.

Confocal and two-photon intravital microscopy:

For confocal imaging, fixed LN tissue sections were imaged as previously described using a Leica SP8 microscope[26]. For two-photon intravital imaging, immunized or control mice were anesthetized and popliteal LNs were surgically exposed and imaged as previously described[63]. Detailed methods can be found in the Supplementary Materials.

Histocytometry:

Histocytometry analysis was performed as previously described[13,26], with some modifications. Myeloid and T cell isosurface three-dimensional (3D) objects were generated in Imaris, and object statistics were then exported to FlowJo software for gating and phenotypic characterization. Additional positional and spatial correlation analysis was performed in CytoMAP[29]. For visual clarity, Imaris 3D surface objects were used for some data display (Figs. 1 and 2, and figs. S1A, S2, and S3G). Detailed methods can be found in the Supplementary Materials.

Cell isolation and flow cytometry:

For myeloid cells, disrupted tissues were treated with collagenase D (400 U/ml; Roche Applied Science). In some studies, enhanced digestion was used for increased cell yield, as described[171,172]. T cell flow cytometry studies did not use enzymatic digestion. Data were acquired on an LSR-II flow cytometer (BD Biosciences) and analyzed using FlowJo software (TreeStar). Detailed methods, as well as antibody and staining reagent data can be found in the Supplemental Materials.

Antibodies, staining reagents, microscopy, and image analysis:

Detailed descriptions are available in Supplementary Methods.

Statistics:

Statistical analysis was performed using GraphPad Prism software. The statistical significance of differences in mean values between two groups was analyzed by a two-tailed unpaired Student's *t* test with Welch's correction. When analyzing data with multiple side-by-side groups, a one-way analysis of variance (ANOVA) with Tukey's multiple comparisons test was performed. In multi-adjuvant comparison studies where variance between groups could not be

assumed to be equal, the Brown-Forsythe and Welch ANOVA tests with Dunnett's multiple comparison tests were performed. Paired t test was performed only when comparing responses within the same experimental animal or tissue. In bar graphs for all figures, bars represent data mean. Error bars represent SD. ****, $P \leq 0.0001$; ***, $P \leq 0.001$; **, $P \leq 0.01$; *, $P \leq 0.05$; not significant, $P > 0.05$. In all figures, unless otherwise noted, data points represent independent LNs.

2.5 Supplementary methods

Antibodies and staining reagents:

Antibodies used for staining sections for confocal imaging or isolated cells for flow cytometry include: CD64 (clone X54-57.1; BioLegend), B220 (clone RA3-6B2; eBioscience), CD3 (clone 17A2; BD), SIRPα (clone P84; BD), CD169 (clone 3D6-112; BioLegend), CD11c (clone N418; eBioscience), CD11b (clone M1/70; eBioscience), Collagen IV (rabbit polyclonal; Abcam), MHC-II (clone M5/114.15.2; BioLegend), IRF4 (clone IRF4.3E4; BioLegend), CD45.1 (clone A20; BioLegend), Ki67 (clone B56; BD Pharmingen), Y-Ae (clone eBioY-Ae; eBioscience), CD3 (clone 17A2; BioLegend), CD69 (clone H1.2F3; BioLegend), CD62L (clone Mel-14; BD Biosciences), CD8 (clone 53-6.7; BioLegend), Ly6C (clone HK1.4; BioLegend), IL-12p40 (clone C15.6; BioLegend), Tbet (clone 4B10; BioLegend), TCF1 (clone C63D9; Cell Signaling), CCR7 (clone 4B12, Biolegend), NK1.1 (clone PK136; BioLegend), CD19 (clone 6D5; BioLegend), CD44 (clone IM7; BioLegend), Ly-6G (clone 1A8; BD Biosciences), XCR1 (clone ZET; BioLegend), IFNγ (clone XMG1.2; eBioscience), GATA3 (clone L50-823; BD Biosciences), IL-2 (clone JES6-5H4; BioLegend), CXCR3 (clone CXCR3-173; BioLegend), CXCR5 biotin (clone 2G8; Fisher Scientific), pS6 (clone 2F9; Cell Signaling), PD-1 (clone RMP1-30; BioLegend), CD45.2 (clone 104; eBioscience), CD25 (clone PC61; BioLegend), F4/80 (clone BM8; eBioscience), TNFα (MP6-XT22; BD Pharmingen), EpCAM (clone G8.8; eBioscience),

CD103 (clone 2E7; BD Biosciences), CD301b (clone MGL2; BioLegend), CD115 (clone CSF-1R; BioLegend), CD26 (clone: H194-112; BioLegend), CD88 (clone 20/70; BioLegend), and Ly-6B.2 (clone 7/4; Novus Biologicals).

For two-photon intravital microscopy studies, CD90.2 (clone 30-H12; BioLegend), CD31 (clone 390; BioLegend), and Dextran-FITC (70,000 MW; Molecular Probes) were used.

Enzyme-linked immunosorbent assay:

For ELISA experiments, dLNs from each mouse were harvested into PBS in Precellys Soft tissue homogenizing tubes (Bertin Corp), and then homogenized for 20 seconds at 5500 rpm in a Precellys 24 Tissue Homgenizer (Bertin Corp). Tubes were then spun at 15000 rpm for 10 minutes at 4°C, and supernatants were concentrated to 50 µl using Microcon 30 kDa columns (EMD Millipore). ELISA assay was then performed on concentrated supernatants using the Mouse IL-12 p70 Quantikine ELISA Kit (R&D Systems), using the manufacturer's described protocol.

Confocal and two-photon microscopy:

For confocal imaging, isolated LNs were fixed using Cytofix (BD Biosciences) buffer diluted 1:3 with PBS for 12 hours at 4° C and then dehydrated with 30% sucrose for 12 to 24 hours at 4° C. Tissues were then embedded in O.C.T. compound (Tissue-Tek) and stored at -80° C. LNs were sectioned on a Thermo Scientific Microm HM550 cryostat into 20 µm sections and were then prepared and imaged as previously described[26]. A Leica SP8 tiling confocal microscope equipped with a 20x 0.7NA or 40x 1.3NA oil objectives were used for confocal image acquisition.

For two-photon intravital microscopy, immunized or control mice were anesthetized using an isoflourane vaporizer and popliteal LNs were surgically exposed. Imaging was done as previously described[27] using a Leica SP8 tiling confocal microscope outfitted with a Chameleon laser and a 20x, 1.0 NA water immersion objective. In some experiments, mice were intravenously

administered dextran-FITC, CD31-Alexa 488, and/or CD90.2-Alexa 488 1 to 2 hours prior to imaging. All acquired raw imaging data was processed and analyzed in Imaris (Bitplane).

Histocytometry:

Histocytometry analysis was performed as previously described[13,26], with some modifications. Multiparameter confocal images were corrected for fluorophore spillover using the built-in Leica Channel Dye Separation module. For acquisition of single stained controls, UltraComp eBeads (Invitrogen) were incubated with fluorescently conjugated antibodies, mounted on slides, and imaged. All images were visualized and analyzed in Imaris. Myeloid cell isosurface objects were created separately on CD11c, MHC-II, and CD64 signal using the surface object creation wizard in Imaris, as previously reported[26]. In some analyses, histocytometry gating was further used to discriminate cDC2 and cDC1 populations using SIRPα and Clec9a markers, respectively. For some experiments, a combined myeloid cell channel was first created by adding normalized signals for SIRPα, CD11c, MHC-II and CD64 using the Imaris XT channel arithmetic module, and this sum channel was then used for object creation. For histocytometry involving T cells, objects were created directly using the congenic CD45.1 signal. Alternatively, all proliferating cells within the LN were analyzed by creating objects using the Ki67 signal. Object statistics were then exported to FlowJo software for gating and phenotypic characterization. TZ borders were manually created using B220 (B cell follicles), CD3 (T cell zone), and CD64 super bright staining (medullary macrophages), and the Spot creation function in Imaris. In some analyses lacking explicit B220 and CD3 staining, TCF1 and MHC-II were used for demarcating the TZ borders. Positional data for the spot objects were exported to FlowJo to generate a spatial T zone gate. TZ localization was calculated as the frequency of a given cell population found within the T zone gate. Cell distances from the deep TZ center were calculated in CytoMAP[29].

Spatial correlation analysis was also performed in CytoMAP. In brief, position of all myeloid cells in LNs were spatially segmented into 30-μm radius neighborhoods and the Pearson correlation coefficient was calculated between the number cells of the different cell types in these neighborhoods.

Cell isolation and flow cytometry:

For myeloid cells, tissues were disrupted and treated with 400 U/ml collagenase D (Roche Applied Science) solution for 30 minutes at 37º C with periodic agitation. In some studies, enhanced digestion was used for increased cell yield, as described[171,172]. Flow cytometry studies conducted on T cells did not use enzymatic digestion. Cell staining was conducted at 4º C for 30 minutes, except for: LCMV GP 66-77 tetramer (NIH Tetramer Core) – room temperature for 1 hour, CXCR5 – room temperature for 45 minutes, and CCR7 – 37º C for 30 minutes. For T cell cytokine production, cells were restimulated with 100 ng/ml of phorbol 12-myristate 13-acetate (PMA), 1 μg/mL ionomycin (Sigma-Aldrich), and 1 μg/ml GolgiStop (BD Biosciences) in complete RPMI media for 4 to 5 hours at 37°C. For myeloid cell cytokine production, cells were stained in media containing GolgiStop, without restimulation. FoxP3 Fix/Perm Kit (Invitrogen) was used. Data was acquired on an LSR-II flow cytometer (BD Biosciences) and analyzed using FlowJo software (TreeStar).

Experimental design:

Experimental animals were randomly allocated into treatment groups. The investigators were not blinded to allocation during experiments and outcome assessment. No statistical method was used to predetermine sample size. All experiments were repeated at least two independent times.

2.6 Acknowledgements

We thank S. Thomas, J. Lund, and J. B. Graham for help with West Nile virus infections, and J. von Moltke and J. W. McGinty for help with *Nippostrongylus brasiliensis* infections. We are grateful to M. Mack for providing the CCR2 blocking antibody. We also thank M. Pepper, E. Hemann, M. Prlic, N. J. Maurice, and A. K. Taber for additional reagents and resources.

Author contributions:

J.M.L., J.Y.H., K.K., and M.Y.G. conceptualized the study. J.M.L., J.Y.H., K.K., M.R.L.-C., B.E.O., and M.Y.G. performed experiments and analyzed data. C.S. developed and implemented the software used in this study. M.G. and C.S. provided critical reagents and resources. J.M.L., J.Y.H., and M.Y.G. wrote the original draft of the manuscript. All authors helped review and edit the manuscript. M.Y.G. supervised the project.

Chapter 3: Current understanding of how immune responses are generated within lymph nodes during type-I inflammation

This chapter is adapted from the following manuscript:

Huang JY, Lyons-Cohen MR, Gerner MY. Information flow in the spatiotemporal organization of immune responses. *Immunol Rev*. Mar 2022;306(1):93-107.doi:10.1111/imr.13046

3.1 Generation of immune responses during type-I inflammation

In contrast to steady state conditions, inflammation of peripheral tissues, and specifically for this review, the murine skin, induces large-scale activation of immune cells both within the affected tissues and the draining LNs to support critical immunological functions. Many microbial infections of barrier surfaces or injected vaccines result in rapid release of pathogens, pathogen or danger associated molecular patterns (PAMPs, DAMPs), foreign antigens, alarmins, and other inflammatory mediators into the tissue parenchyma and subsequently the lymph[3]. Within minutes, these agonists flood the draining node, and the innate immune cells positioned within the lymphatic sinuses provide the first line of defense to contain the incoming threats as well as to trigger the initial wave of inflammation (Figure 1). Macrophages lining the lymphatic sinuses serve as local "flypaper," and readily capture antigens, immune complexes, and pathogens as they enter through the afferent lymph. Medullary macrophages are highly phagocytic and rapidly degrade the captured microbes[18]. In contrast, subcapsular sinus macrophages are less degradative, and instead deliver the sequestered antigens to adjacent B cells to drive humoral immune responses[173-176], as well as secrete type-I interferon (IFN-I) to alert and protect neighboring cells from further pathogen spread[177-179].

In addition to direct containment, inflammasome activation and locally released cytokines from subcapsular macrophages elicits robust antigen-independent production of type-II interferon (IFN gamma, IFNγ) by nearby innate lymphoid cells (NK cells, gamma-delta T cells, NKT cells, and innate-like CD8 T cells). This rapid wave of IFNγ in turn enhances the phagocytic activity of macrophages to amplify host defense[21]. Inflammasome activation also stimulates the influx of additional innate effector cells from the blood[21,180], including neutrophils, which provide further support for pathogen containment[21,181-183]. Memory CD8 T cells close to the subcapsular sinus similarly secrete IFNγ upon detection of cognate antigen, inducing local CXCL9 production by macrophages and stromal cells. This leads to the repositioning of additional CXCR3-expressing memory T cells towards the site of infection, and these bystander-activated CD8 T cells rapidly mediate pathogen clearance[23,24,184]. CXCL9 can also be displayed on the lumen of high endothelial venules, enabling additional recruitment of central and effector memory CD8 T cells from the circulation[185]. Thus, within just a few hours of inflammation, various innate effector and adaptive memory cells that are pre-positioned in or rapidly recruited to the subcapsular sinus niche create a barrier to pathogen entry and prevent dissemination into the blood circulation as well as the deeper parenchymal regions of the LN.

Also enriched near the lymphatic sinuses are LN resident cDCs, and as shown by our group as well as by others, this allows them to efficiently intercept and present draining antigens[27,28,36,101,121]. The peripheral positioning of resident cDCs near the lymphatic sinuses, however, minimizes their chances of interacting with cognate naïve T cells, which are primarily localized within the T cell zone. In contrast to macrophages, which recruit immune cells locally, we demonstrated that activated resident cDCs instead undergo rapid maturation to express the chemotactic receptor CCR7, and use the CCL19/CCL21 chemotactic gradient within the LN

parenchyma to relocalize from the lymphatic-rich peripheral regions into the T cell zone[28]. As these resident cDCs mature, they also increase surface expression of MHC and costimulatory molecules, thus facilitating enhanced antigen presentation and subsequent scanning by and activation of cognate T cells[28]. Further efficiency in reducing the search time for cognate cDC–T cell interactions is achieved directly within the T cell zone. As we and others have shown, resident and migratory cDC subsets segregate here, with activated cDC2s preferentially localizing in the outer paracortex, and cDC1s predominantly positioned within the deeper T cell zone, and this is conserved across most, but not all, Type-I inflammatory conditions[16,28,72,73]. This segregation of innate cells is also mirrored by the non-random distribution of naïve CD4 and CD8 T cells. CD4 T cells express higher levels of Ebi2 and also preferentially localize within the outer paracortex, thus paralleling the distribution of Ebi2-expressing cDC2s[74,116]. Given the enhanced abilities of cDC2s in MHC-II antigen presentation, and the converse specialized ability of cDC1s to cross-present antigens on MHC-I, we found that this spatial coordination between the cDC and T cell subsets further reduces the search space necessary for the T cells to locate their MHC-presenting cognate antigens, and ensures rapid generation of T cell responses in the event of an inflammatory insult[74].

As the resident cDCs migrate towards the T cell zone to elicit these cognate responses, we and others have demonstrated that inflammatory monocytes within the blood circulation also begin to infiltrate the draining LNs in large numbers via the high endothelial venules[28,93,94,186]. Upon entering the LN parenchyma, the recruited monocytes acquire markers of activation and migrate into the T cell zone, eventually colocalizing with the co-clustered resident cDCs and early activated T cells[28]. In comparison with resident cDCs, monocyte maturation and entry into the T cell zone is relatively delayed, and monocytes do not appear to play a significant role in early antigen

presentation and T cell activation in these settings. However, monocytes do arrive at the optimal time to provide an ample source of IL-12 to support the differentiation of recently activated T cells, and thus cooperate with the cDCs to enhance T cell effector programming[28,93,94]. Therefore, we suggest that the spatiotemporal dynamics of resident cDC and monocyte migration, maturation, and function represent critical features of T cell activation and differentiation in LNs during Type-I inflammation.

Following these very early T cell activation events, additional involvement of the CXCL9/10–CXCR3 chemokine axis has been shown to help reinforce subsequent effector T cell programming[100]. Expression of CXCL9 and CXCL10 chemokines by stromal and myeloid cells in the peripheral regions of inflamed LNs, such as the interfollicular zones and along the T-B boundary, elicits the recruitment of early differentiated effector T cells expressing CXCR3[156,162,186-189]. Multiple cellular sources likely contribute to the generation of this chemotactic gradient, including monocytes which are significant producers of CXCL9 and CXCL10 following skin immunization[156,162,186-188]. Migration of early effector T cells towards these microenvironments exposes these cells to additional sources of antigen and inflammation, and thus further enhances their differentiation[162,186,187]. Of note, early activated CD4 T cells expressing Tbet and CXCR3 can also utilize this chemotactic axis to migrate to the T-B border and promote humoral immunity[189]. In contrast, less-differentiated CD8 T cells are predominantly retained within the deep T cell zone, which further enhances the bifurcation of T cell responses[187].

Additional innate support for the generation of T cell responses during Type-I inflammation has been shown for NK cells and plasmacytoid DCs (pDCs). IFNγ secreted by NK cells within the subcapsular sinus regions can enhance the activation of neighboring myeloid cells. Consistent with this, depletion of NK cells or blockade of IFNγ in certain inflammatory settings

can lead to reduced cDC and monocyte responses, including diminished expression of IL-12 and CXCL9[156,190-192]. Reciprocally, IL-12 or IL-18 cytokines released by the activated cDCs or monocytes may amplify NK cell-mediated IFNγ production to create a positive feed-forward inflammatory cascade[188,191,193,194]. pDCs have also been shown to facilitate adaptive responses. During viral infection, pDCs can undergo CCR5-mediated intranodal migration within LNs to colocalize with responding CD8 T cells and cDC1s in order to optimize cDC1 maturation and downstream T cell priming via IFN-I signaling[91]. The CCR5 chemotactic axis has also been previously shown to enhance CD4 T cell help to CD8 T cell responses, by promoting more efficient scanning of cognate antigens by naïve CD8 T cells and for generating productive memory responses[30,31,195-199].

In addition, migratory cDCs residing directly within inflamed tissues also integrate pathogen-derived signals and inflammatory cues, undergo full maturation, and traffic to the draining LNs in a CCR7-dependent manner to facilitate the generation of adaptive immunity[36,41,200]. The relative contributions of migratory vs. resident cDCs in T cell priming appear to be condition specific. As we and other groups have demonstrated, in settings of robust antigen and inflammatory agonist drainage via the lymph, with the exception of TfH responses, migratory cDCs appear mostly dispensable for early T cell responses[27,28,101,121,201]. However, during highly tropic or slowly replicating microbial infections, such as HSV infection, foreign antigens and stimuli remain largely trapped in the periphery and do not enter the lymph in sufficient quantities to elicit responses by LN-resident innate cells. In these settings, antigen-bearing migratory cDCs are indispensable for the initiation of T cell immunity[31,145,146]. In particular, migratory cDC1s can produce copious amounts of IL-12 and directly support the induction of Th1 and CD8 effector responses[132,134,145]. Dermal cDC2s can also undergo functional maturation to support Th1, Th2

(below) or Th17 polarization, based on the specific types of encountered stimuli[128,200,202]. In addition to direct induction of T cell responses, in certain infection or tumor models, migratory cDCs can transfer antigens to resident cDCs to further potentiate T cell activation[30-32,148]. It has also been shown that lymph-borne antigens can be stored within LN LECs for extended periods of time, and then slowly released to the transmigrating migratory cDCs, leading to continued induction of T cell immunity[203-205].

In sum, Type-I inflammation induces a large-scale, orchestrated activation, recruitment, and crosstalk of multiple innate and adaptive cell types within draining LNs, which together promote rapid pathogen containment, as well as facilitate optimal generation of adaptive immunity.

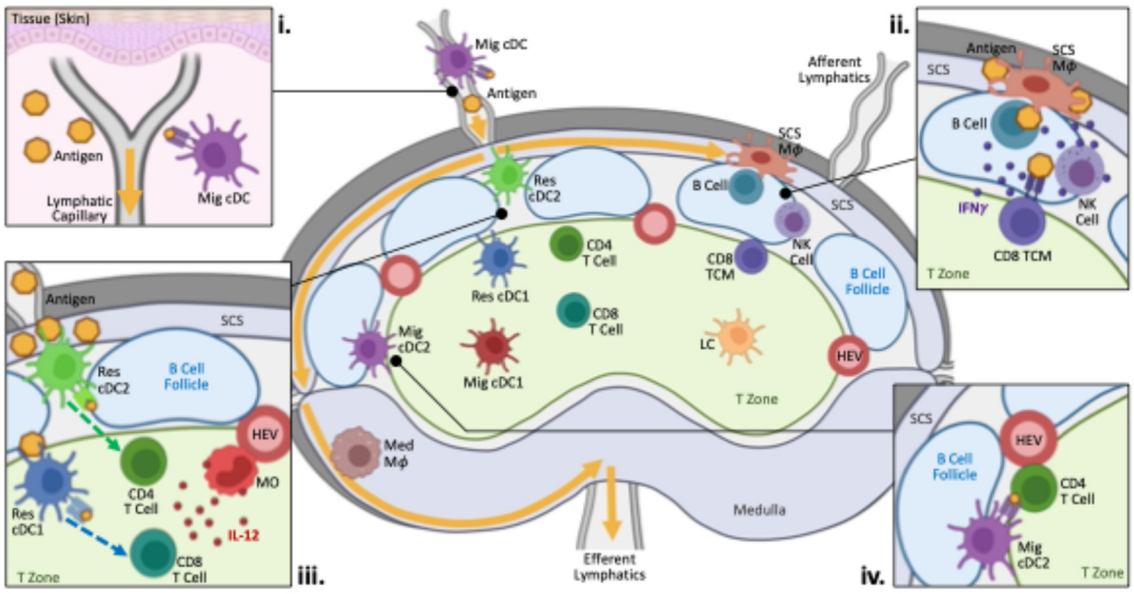

Figure 1. Initiation and organization of immune responses within lymph nodes.
Diagram depicts the preferential localization of different immune populations within steady state LNs. Biased spatial positioning is seen for both innate and adaptive cell subsets. (i) At both steady state and during inflammation, information about the state of peripheral tissues is delivered into the nearest LNs via the lymphatics either through direct antigen drainage or active transport by migratory cDCs. (ii & iii) During Type-I inflammation, macrophages and resident cDCs located directly within or proximally to the lymphatic sinuses readily capture antigens and inflammatory agonists. (ii) Innate and adaptive immune cells positioned near the subcapsular sinus initiate early inflammatory responses to promote pathogen containment and clearance. (iii) Resident cDCs also undergo maturation and relocalize into the T cell zone,

while inflammatory monocytes infiltrate the LN from the blood. Together, these two cell types functionally cooperate to drive early T cell activation and effector differentiation. Migratory cDC1s can also support Th1 differentiation. (iv) Antigen-bearing migratory cDC2s preferentially position along the T-B border, where they interact with responding CD4 T cells to promote TfH responses. During Type-II inflammation, these cDCs are also the dominant drivers of Th2 differentiation. Yellow arrows indicate direction of lymph flow. Created with BioRenderer.com. Abbreviations: CD8 TCM, central memory CD8 T cell; HEV, high endothelial venule; LC, Langerhans cell; Mϕ, macrophage; Med, medullary; Mig, migratory; MO, monocyte; Res, resident; SCS, subcapsular sinus

3.2 Information gradients in the generation of immune responses

Additional considerations to how immune responses are propagated within reactive LNs are the spatial distribution and kinetics of lymph-borne antigens, inflammatory agonists, and the incoming migratory cDCs (Figure 2). Imaging studies by us and others have demonstrated that drainage of antigens and other soluble mediators from the inoculation site to LNs can happen within several minutes[13,14,90,121,206,207]. Upon reaching the lymphatic sinuses, proteins and particles are physically separated based on molecular weight, with smaller antigens (<70kDa) and fluids entering the LN conduit network distributed throughout the interfollicular regions and the T cell zone[90,208-211]. These conduits are also directly connected to the nearby blood vessels, and within a few hours, fluid-borne antigens, cytokines, and chemokines that entered the conduits are rapidly cleared out into the circulation. This can promote deposition of chemokines and inflammatory mediators on the lumen of high endothelial venules and lead to enhanced trafficking of immune cells into the reactive LNs[98,209,212]. In contrast, large antigens and pathogens are retained within the lymphatic sinuses, and instead can directly cross the floor of the lymphatic sinuses into the parenchyma either by passive diffusion via local fenestrations or by active transcytosis by the LECs[13,14,206,213]. We have previously shown that this results in enhanced accumulation of certain antigens within the lymphatic sinuses and the sinus-proximal parenchymal space, and the generation of steep antigen gradients across the LN. Significantly greater amounts of antigen are deposited near the lymphatic sinuses, while reduced quantities are found within the deeper T cell

zone[13]. Given the preferential distribution of macrophages and resident cDC2s near the lymphatics, this leads to increased uptake of antigens by these populations[13,14]. In contrast, lower abundance of antigens within the deeper T cell zone leads to reduced antigen capture by the centrally localized cDC1s. As a consequence, subunit immunizations with limiting doses of antigen result in enhanced CD4 T cell activation as compared to CD8 T cells[13]. This suggests that the spatial positioning of cDC subsets within the LN, coupled with the generation of antigen gradients across the tissue, directly impacts which classes of cellular immunity are generated. Such spatial regulation of T cell responses may reflect the distinct roles of these T cell subsets in immunity. Preferential CD4 T cell responses to lymph-borne soluble antigens may promote an appropriate balance of activation against extracellular draining antigens. Early and efficient activation of CD4 helper T cells may also be necessary in order for these cells to provide timely help for CD8 T cell and humoral responses[30,31,64,196,214]. This is in contrast with intracellular infections, which are less likely to result in copious amounts of soluble antigens. In these settings, the more centrally localized cDC1s may be optimally positioned to acquire and cross-present antigen derived from infected host cells or antigen-bearing migratory cDCs, thus promoting robust CD8 T cell responses during conditions when the effector functions of cytotoxic CD8 T cells would be most utilized[30-32].

We have recently demonstrated that in addition to the radial axis of antigen dispersal across the lymphatic and T cell zone regions, lateral dispersal gradients also likely contribute to the generation of immune responses (Figure 2). LNs contain multiple incoming afferent lymphatic vessels, each draining a unique peripheral tissue, which are distributed in distinct sites across the subcapsular sinus. Accordingly, during infection or immunization of a given tissue, the draining node receives incoming stimuli via one dominant lymphatic vessel. This in turn results in markedly greater deposition of antigens and agonists in regions most proximal to the involved afferent vessel,

and leads to establishment of lateral gradients across the LN[13,28]. Concentration of antigen and inflammatory signals on one side of the LN is likely to influence the activation, localization, and function of multiple innate cell types. In this regard, we found highly polarized infiltration of inflammatory monocytes during Type-I inflammation, leading to varied abundance of innate cell subsets across the tissue[28]. Similar considerations likely apply to migratory cDCs. As various migratory cDC subsets accumulate within the draining LN[31,43,215,216], they similarly enter from the specific afferent lymphatic vessel draining the inflamed tissue, and this likely reinforces the polarized distribution of antigen-bearing cDCs across the LN parenchyma. Consistent with this idea, in a variety of infection settings, more robust migratory cDC-driven T cell priming can be observed on one side of the draining LN[31,187,217,218]. Together, this lateral axis of innate cell composition and activity sets up the generation of multiple distinct microenvironments within a single LN, in which T cells experience divergent conditions during early activation dependent on their localization[28]. In turn, this imparts distinct differentiation properties to the responding T cells. As we demonstrated in settings of Type-I inflammation, increased infiltration of IL-12-producing activated monocytes into one side of the LN after immunization results in the localized generation of highly differentiated effector T cells. Conversely, less differentiated T cells expressing markers of memory precursor cells are preferentially observed in regions with fewer inflammatory monocytes and a greater abundance of cDCs[28]. We thus propose that the fundamental rules of lymphatic flow and information dispersal across the LN can directly regulate the heterogeneity of the resultant T cell response.

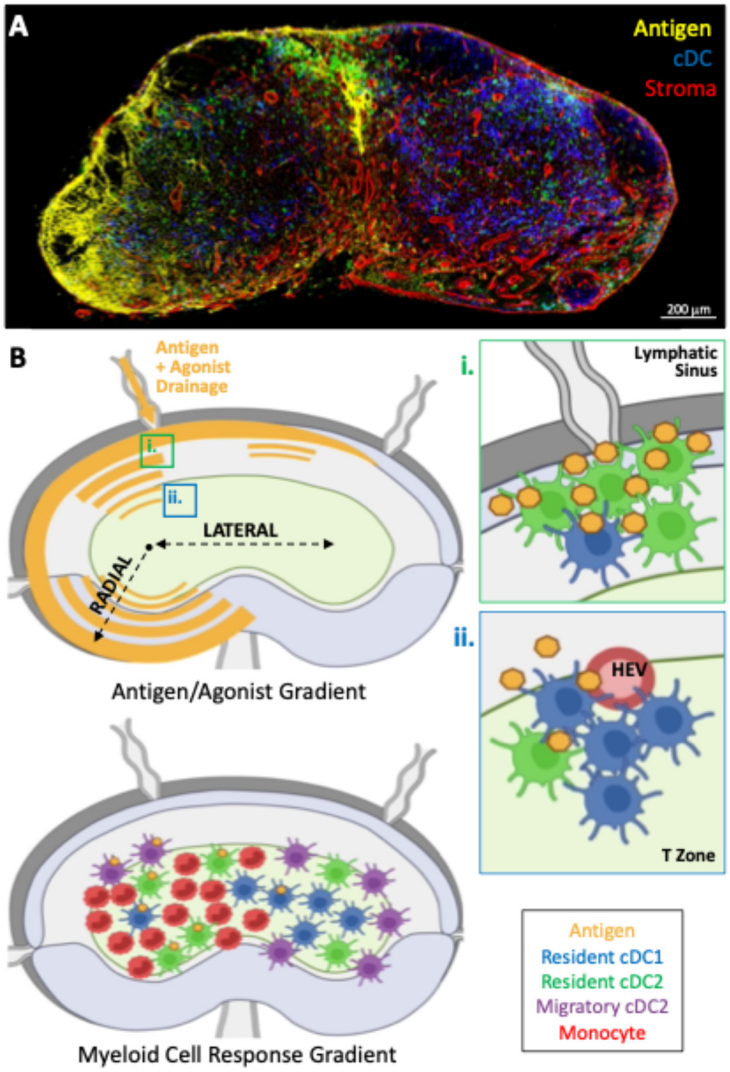

Figure 2. Generation of information gradients within lymph nodes. (A) Confocal microscopy image of a draining LN demonstrating gradient formation 2 hours after subcutaneous injection of EαGFP (antigen, yellow) fluorescent protein. cDCs and stromal networks are also revealed with CD11c and Collagen-IV staining, respectively. (B) Schematic showing the radial and lateral gradients of antigen and agonist which are generated within the draining LNs (top). Influence of radial gradients is depicted in the zoom insets (i & ii). (i) Resident cDC2s are enriched near the lymphatic sinuses, and robustly acquire draining antigens. (ii) Lower abundance of antigen is observed within the T cell zone, therefore limiting antigen capture by the more centrally localized cDC1s. Bottom panel depicts the influence of lateral gradients on downstream myeloid cell localization and function. Created with BioRenderer.com.

Overall, these studies reveal several key features of how immunity is generated and provide important considerations for rational vaccine design. In particular, our past observations of reduced antigen capture by resident cDC1s and less efficient CD8 T cell activation during subunit immunization may have critical implications for vaccine outcomes. In line with this, while subunit vaccines have been shown to generate robust CD4 T cell and antibody responses in humans, they do not appear to induce robust CD8 T cell responses, even when delivered with potent adjuvants[300,301]. Thus, strategies to better retain antigens within the draining LN, while also promoting higher diffusive properties, may help to improve CD8 T cell responses during vaccination[152,302]. In this regard, vaccine formulations that are designed to promote long-term antigen persistence in draining LNs have been shown to augment CD8 T cell responses[110,303,304].

Work by many groups, including ours, also highlight the notion that functional cooperation between diverse innate cell types is intimately involved in regulating the magnitude and quality of both cell-mediated and humoral immunity. Therefore, vaccine strategies that simultaneously target multiple innate cell populations should be explored. Finally, it should be noted that different routes of immunization can induce distinct kinetics and biodistribution of vaccine derived materials. This can influence myeloid cell maturation and function as well as downstream adaptive immunity, which can in turn further shape vaccine outcomes[305,306].

Chapter 4: Dendritic Cells Regulate the Innate-Adaptive Balance in Lymph Nodes for Optimal Host Defense

This chapter is adapted from the recently submitted manuscript:

Huang JY and Gerner MY. Dendritic cells regulate the innate-adaptive balance in lymph nodes for optimal host defense. 2025. *In revision*.

4.1 Introduction

Lymph nodes (LNs) have evolved to serve two fundamental functions. They filter draining lymph and provide innate defense against disseminating pathogens, as well as bring together antigen presenting cells and recirculating T cells to initiate the generation of adaptive immunity.

During infection of peripheral tissues, lymphatic vessels can transport microbes via the lymph into the bloodstream, resulting in dissemination and sepsis. This necessitates potent mechanisms of defense by the host immune system to contain the draining pathogens. Much of this is mediated within LNs, which filter the lymph and locally elicit protective innate responses. LN macrophages located within the lymphatic sinuses intercept many of the incoming microbes, while concurrently inducing the activation of nearby lymphoid cells, including NK cells, to further amplify antimicrobial functions of the organ[19,21]. Circulating neutrophils and monocytes are also recruited into the LNs through high endothelial venules (HEVs) and swarm the sites of infection to support microbial containment[21,180-183,219,220]. Together, this results in the rapid generation of an innate cell firewall at the lymphatic sinuses, where multiple innate effector cells functionally cooperate to limit pathogen spread.

In addition to innate defense for immediate protection against disseminating pathogens, LNs are critical sites which generate adaptive responses for long-term sterilizing immunity. In

particular, dendritic cells (DCs) are innate sentinels that respond to local inflammatory cues and efficiently process antigens for MHC presentation, serving as professional antigen presenting cells for T cell responses. Positioning of DCs within tissues is important for facilitating their functions. In the steady state, many LN-resident DCs are strategically localized near or within the lymphatic sinuses, promoting lymph sampling and capture of information about the state of peripheral tissues[13,26,27,221]. During infection or vaccination, these DCs efficiently take up draining antigens, undergo maturation, and relocalize into the T cell zone[28,222]. Migratory DCs also enter the T cell zone over time, providing additional antigenic information. As a result, activated DCs spatially converge with a pool of naïve, recirculating T cells, which enter LNs via HEVs and migrate throughout the T cell zone, searching for cognate stimuli. Together, the DC populations present antigens on MHC molecules in the context of costimulatory molecules and cytokines to the naive T cells to initiate adaptive immunity[200,221].

This innate-adaptive functional duality of the LN is paramount for effective host defense. One strategy that enables the organ to effectively perform both its roles is the relative compartmentalization of innate effector cells and T cells within distinct regions of the tissue[15,221]. Innate inflammatory responses are generally thought to be confined to the outer boundaries of the LN, such as near or within lymphatic vessels, which are the sites of early microbe dissemination. In contrast, the generation of T cell responses occurs within the T cell zone, which is situated in the LN interior and in close proximity to HEVs. Notably, we and others have demonstrated that during infection or vaccination, monocytes also migrate into LNs via HEVs and robustly infiltrate the T cell zone[28,93,94,188]. This recruitment occurs in a highly polarized manner, resulting in the formation of distinct innate cell microenvironments, characterized by monocyte-rich versus DC-dominant regions[28]. Once in the paracortex, the monocytes undergo activation and functionally

cooperate with the antigen-presenting DCs by producing large quantities of the inflammatory cytokine, IL-12[28,93,94,188]. This locally amplifies effector T cell differentiation, leading to divergent programs of early T cell priming that are spatially encoded across the tissue, which in turn promotes heterogeneity in the adaptive immune response[28].

The mechanisms regulating monocyte trafficking and polarization across the LN, as well as their coordinated crosstalk with both DCs and T cells, remain undefined. Moreover, the findings that innate effector cells efficiently infiltrate the T cell zone indicate that strict compartmentalization of innate and adaptive responses is not as clearly delineated as thought. Complicating this further are studies showing that monocytes, neutrophils, and NK cells can all suppress adaptive responses in certain settings of inflammation, resulting in counterproductive processes that could lead to failure of efficacious immunity[223-234]. This suggests that there must be a system which coordinates and synchronizes both innate and adaptive responses across the LN to ensure productive host defense.

Here, we examined the spatiotemporal dynamics of innate and adaptive responses within LNs following vaccination or disseminating bacterial infection. We found that these inflammatory stimuli elicited a rapid modulation of LN architecture and function, with large-scale and polarized infiltration of multiple innate effector cells, including neutrophils, monocytes, and NK cells, across the LN parenchyma and T cell zone. This recruitment was mediated by conventional DCs, which upon maturation and intranodal migration, generated a rich haptotactic matrix to support directed innate cell trafficking across the tissue. Although these processes were essential for effective innate defense, such extensive innate cell influx disrupted the T cell zone, rendering the LN suboptimal for the generation of adaptive responses. However, this disruption was transient and reversible, as upon pathogen containment, DCs along with DC-recruited monocytes restored the LN architecture,

as well as established the innate cell microenvironments necessary for downstream T cell response heterogeneity. Taken together, these findings identify that, beyond their classical roles as antigen presenting cells, DCs dynamically tune the balance between innate and adaptive functions of the LN, promoting synchronized and coordinated responses of both to meet the organism's immediate and long-term immunological needs.

4.2 Results

Rapid, large-scale, and polarized recruitment and redistribution of innate effector cells in LNs during inflammation

We first studied the dynamics of innate and adaptive immune cells within draining LNs following intradermal or footpad administration of several type-I inflammatory stimuli. These included immunization with a TLR9 agonist (CpG), inoculation with heat-killed *Escherichia coli*, or live bacterial infection with *Pseudomonas aeruginosa*. Draining LNs were collected at various time points after challenge and examined by flow cytometry. Assessment of the fold change in cellular abundance with respect to steady state revealed that across all three models, there was a rapid and selective increase in the recruitment of neutrophils and monocytes into the LNs, while T and B cells remained relatively unchanged (Figures 1A and S1A). Consistent with other reports[28,93,181,220,235], neutrophils and monocytes primarily entered draining LNs from the blood via HEVs, as CD62L blockade markedly reduced their cellularity (Figure S1B). In contrast, removal of the immunization site two hours after had a no significant effect, suggesting a limited role for lymphatic trafficking at these time points. To provide additional resolution of cellular influx, we used serial intravascular staining (SIVS), which involves timed intravenous (i.v.) antibody labeling to detect cells that have entered the tissue parenchyma from circulation[236,237]. Validation of this

approach with microscopy showed that, unlike the cells i.v.-labeled 3 to 5 minutes before harvest which remained localized within the blood vasculature, cells labeled 2 hours prior were predominantly found within the LN parenchyma (Figure S1C). Flow cytometry analysis further confirmed that most cells labeled 1 to 3 hours before tissue harvest were not stained with the 5-minute i.v.-administered probe, indicating that these cells were no longer in circulation (Figure S1D). We then used SIVS to measure the relative entry rates for various immune cell types during early inflammation. Again, we found that the cellular influx rates were selectively increased for neutrophils and monocytes, but not for other lymphocyte populations (Figures 1B and S1E). These data demonstrate that there is a preferential bias towards rapid recruitment of innate effector cells, rather than adaptive immune cells, into the draining LNs following immunization and infection.

We next used histo-cytometry to quantitatively visualize innate cell trafficking and localization within the LNs (Figure S1A)[26,28]. At homeostasis, innate effector cells and resident DCs are primarily localized near the lymphatic sinuses or in proximity to blood vessels, while the deep T cell zone mainly contains activated migratory DCs and a fraction of resident DC1s[21,26,27,29,222,238-240]. Strikingly, all tested models of inflammation resulted in significant remodeling of innate cell organization within the draining LNs (Figures 1C and 1D). Consistent with prior observations[28], resident DCs intranodally repositioned from the outer periphery into the T cell zone, and this was accompanied by a large influx of inflammatory monocytes from the blood. In addition, we observed a marked infiltration of neutrophils, which was particularly prominent during bacterial infection (Figures 1C and 1D). Many neutrophils were detected directly in or adjacent to HEVs, consistent with predominant recruitment via local blood vessels. Within the LN parenchyma, these neutrophils accumulated both at the subcapsular sinus and medulla as previously described[21,219,220], but also were found well beyond these peripheral regions,

encompassing substantial portions of the B cell follicles and deeper T cell zone. Another innate effector cell type that we visualized was NK cells, as proper positioning of these cells has been implicated in innate defense[238]. Although changes in their cellularity were relatively minor (Figures 1B and 1C), we found that during inflammation, NK cells repositioned from their steady state localization in the medulla to the T cell zone (Figure 1D). Notably, these observed responses were all highly polarized across the tissue, with more pronounced recruitment of innate effector cells corresponding with the sites of increased agonist deposition[13,28,221], suggesting that the cells were rapidly migrating towards the sites of inflammation to perform their effector functions. Interestingly, concurrent visualization of T cell trafficking using SIVS revealed that HEVs with enhanced neutrophil recruitment also displayed reduced T cell entry, and instead, T cell infiltration was largely relegated to more distal and less inflamed regions of the LN (Figure 1E). Altogether, these results show that type-I inflammation elicits rapid, large-scale, and polarized recruitment and redistribution of multiple innate effector cells across the LN. Furthermore, these innate responses occupy significant areas of the organ that are typically associated with adaptive immune functions.

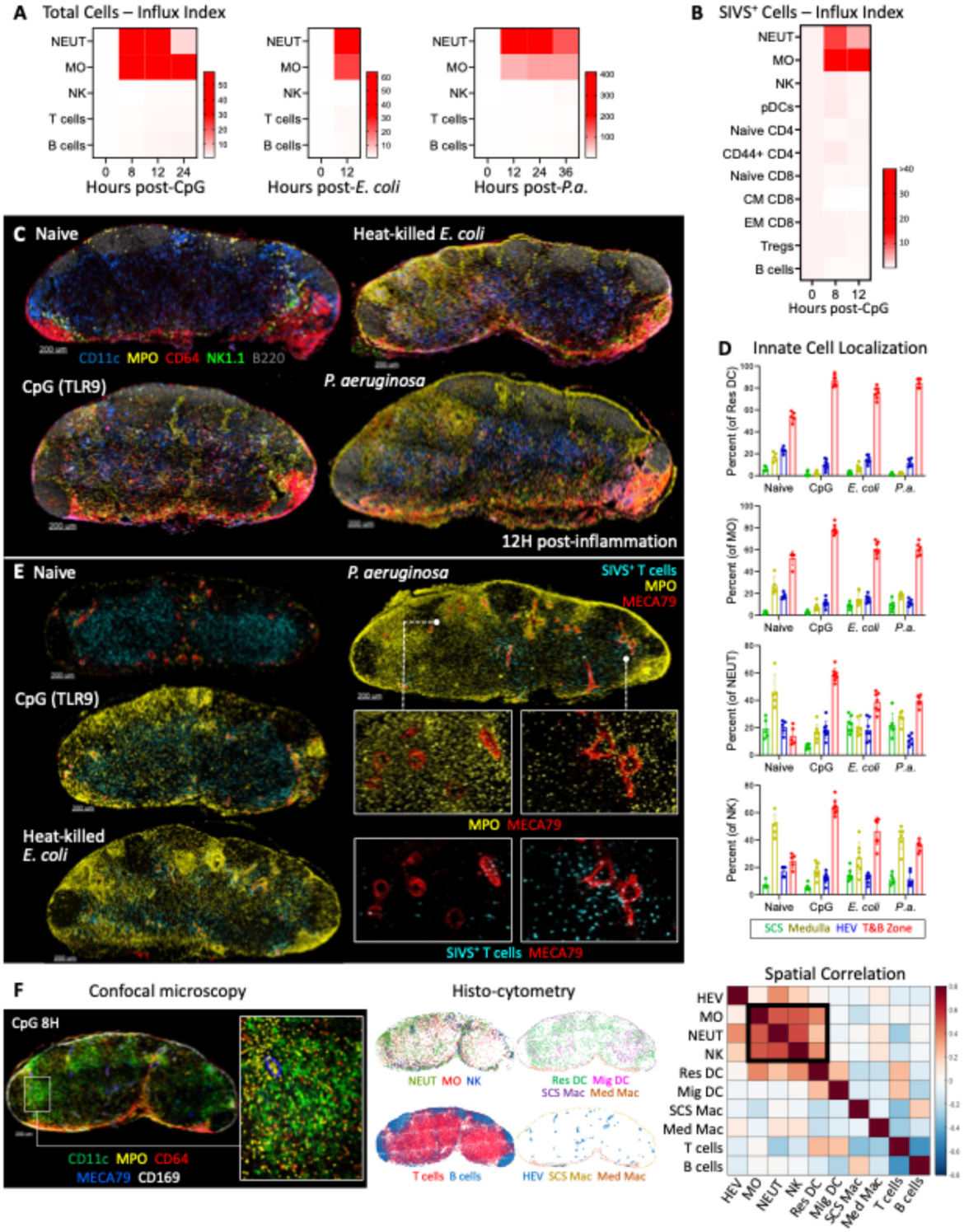

Figure 1. Type I inflammation elicits rapid, large-scale, and polarized recruitment of innate effector cells.

(A) B6 mice were immunized with CpG, inoculated with heat-killed *E. coli*, or infected with *P. aeruginosa* and draining LNs were assessed by flow cytometry at the indicated time points. For each cell type, the relative increase in cell number (i.e. influx index) was measured by dividing the total number of cells in

draining LNs by the average number of cells in naïve LNs. (B) CpG-immunized mice were given an i.v. injection of fluorescent CD45.2 antibody 3 hours before tissue harvest (i.e. SIVS). The influx index for $SIVS^+$ cells in draining LNs was enumerated via flow cytometry 8 hours after immunization. (C and D) B6 mice were treated with the indicated stimuli and draining LNs were visualized by microscopy 12 hours later. (C) Representative images and (D) quantification of innate cell distribution using histo-cytometry. (E) B6 mice were treated with the indicated stimuli and SIVS was performed 1 hour before harvest. Images show the positioning of $SIVS^+$ $CD3^+$ T cells and MPO^+ cells (neutrophils) 12 hours after immunization or infection. MECA79 identifies HEVs. (F) Innate cells within draining LNs were examined by microscopy 8 hours after CpG immunization (left). Histo-cytometry was performed to map the specified cell types (middle). Spatial correlation analysis for cell pairs across the LN (right). Graphs in (D) show mean ± SD. All data are representative of at least two independent experiments.

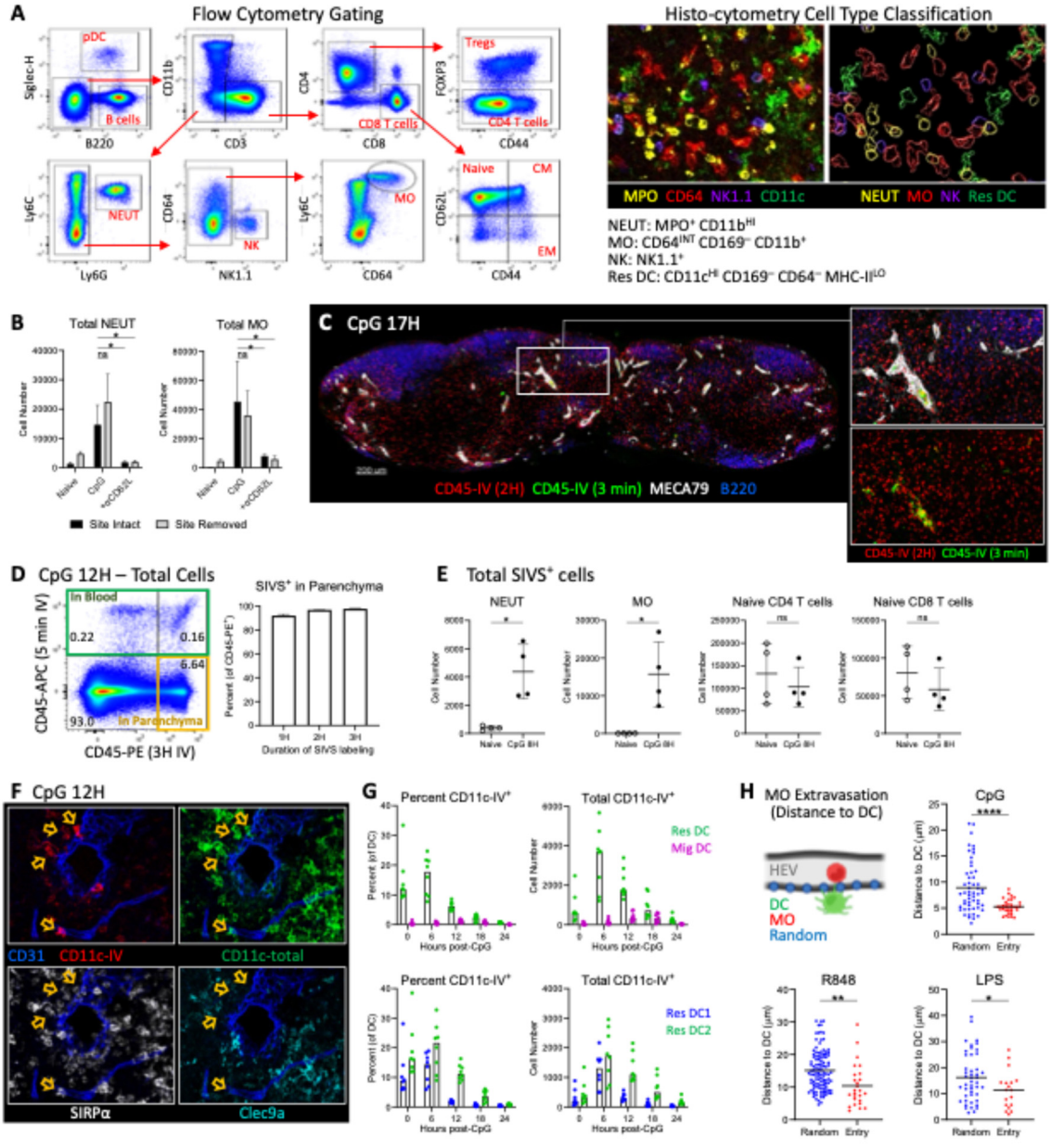

Figure S1. Characterization of cellular influx into LNs during inflammation.

(A) Flow cytometry gating scheme for various cell populations (left) and representative histo-cytometry object classification for innate cells in LNs (right). (B) B6 mice were immunized with CpG in the ear pinnae, with or without anti-CD62L treatment. Two hours later, one immunization site was surgically removed and the contralateral was left intact. Draining LNs were analyzed by flow cytometry 12 hours post-immunization. (C) Validation of SIVS by microscopy. CpG-immunized mice were given sequential i.v. injections: CD45.2–PE 2 hours before tissue harvest and CD45.2–BV421 3 minutes prior. (D) Validation of SIVS via flow cytometry. CpG-immunized mice were given two i.v. injections: CD45.2–PE either 1, 2, or 3 hours before harvest and CD45.2–APC 5 minutes prior. (E) Supplemental data for Figure 1B. Total number of $SIVS^+$ cells in naïve LNs versus 8 hours after CpG immunization. (F and G) B6 mice were immunized with CpG and then given an i.v. injection of CD11c–PE 30 minutes before harvest. (F) Visualization of IV^+ vasculature-associated DCs by microscopy. (G) Characterization of IV^+ DC subsets via flow cytometry. (H) CCR2-RFP CD11c-YFP mice were immunized with the specified TLR agonists (CpG–TLR9, R848–TLR7/8, or LPS B4–TLR4) and draining LNs were imaged by intravital two-photon microscopy. Distance from monocyte extravasation sites to the nearest DC was compared with the distance from random points along the blood vessel to the nearest DC. Graphs in (E) and (H) show mean ± SD and were analyzed using unpaired *t* test with Welch's correction. **** $P \leq 0.0001$; ** $P \leq 0.01$; * $P \leq 0.05$; not significant (ns) $P > 0.05$. All data are representative of at least two independent experiments.

Conventional DCs regulate innate cell trafficking and LN organization

We next sought to investigate the mechanisms regulating innate cell recruitment and localization. DCs represent the largest population of innate sensory cells within the LN parenchyma. During inflammation, as activated resident DCs migrate away from the lymphatic sinuses and towards the T cell zone, they traverse through the interfollicular regions, which are rich with HEVs (Figure 1F, left)[28]. Intravascular staining with fluorescent anti-CD11c antibody to label vasculature-associated DCs[222,241,242] confirmed that many DCs were localized near blood vessels (Figure S1F). The labeled cells were predominantly comprised of resident and not migratory DCs, with the number of vessel-associated DCs peaking around 6 hours post-immunization, and then diminishing over time (Figure S1G), consistent with the timing of resident DC accumulation within the T cell zone[28]. Furthermore, the composition of DCs associated with LN blood vessels changed across time, with resident DC2s becoming the primary subset labeled by 12 hours after agonist administration (Figures S1F and S1G). Notably, resident DC association with blood vessels coincided with neutrophil and monocyte recruitment via HEVs (Figure 1F, left). Additional analysis of cellular spatial correlations across the inflamed LN using CytoMAP[29]

demonstrated that the positioning of neutrophils, monocytes, and NK cells was positively correlated with one another, as well as with resident DCs (Figure 1F, middle and right). In contrast, these innate effector cells showed weaker or negative spatial correlations with migratory DCs as well as macrophages.

To further explore the relationship between innate cell trafficking and DC positioning, we visualized draining LNs by intravital two-photon microscopy. We first used CD11c-YFP Actin-DsRed double reporter mice, in which DsRed is highly expressed in endothelial cells[243]. This showed that there were many CD11c-expressing DCs closely associated with the HEVs, often appearing to extend dendrites directly into the HEV lumen (Movie S1). We next examined monocyte and DC dynamics within the LNs using CCR2-RFP CD11c-YFP double reporter mice, with i.v. injection of fluorescent dextran to label the vasculature[28]. We found abundant monocyte extravasation following immunization, and frequently multiple monocytes entered the LN parenchyma from the same location, indicating the presence of hotspot entry sites along the HEVs[244-247] (Movie S2). Intriguingly, these hotspots were located directly adjacent to perivascular DCs, and the monocytes continued to interact extensively with DCs upon migration into the perivascular space. Quantification of the distance between monocyte extravasation points and the nearest DC, using these and previously published data[28], revealed that there was a preferential bias for monocyte entry at sites proximal to DCs, compared with random points along the blood vessel (Figure S1H). Similar observations were made when we visualized neutrophil trafficking in relation to DCs, as detected by i.v. injection of fluorescent anti-Ly6G antibody into CD11c-YFP reporter mice (Movie S3). Taken together, these data suggest that resident DC activation and localization near blood vessels may be functionally connected with innate effector cell recruitment and positioning.

We therefore hypothesized that DCs could be directly involved in regulating innate cell trafficking in LNs during inflammation. To test this, we generated Zbtb46-DTR bone marrow chimeras, which allow depletion of conventional DCs following diphtheria toxin (DT) administration, without off-target toxicity[120,248]. Zbtb46-DTR chimeras were immunized with CpG, with or without DT injection 4 hours prior, and SIVS was performed 3 hours before tissue harvest to study the rates of cellular entry. In comparison with immunization only controls, DC ablation led to significant decreases in the total number of neutrophils and monocytes within draining LNs, with concordant reductions in the abundance of SIVS-labeled cells emigrating from the blood (Figures 2A, 2B, and S2A). No major changes were observed within the bone marrow (Figure S2B), suggesting that the absence of DCs did not simply impair leukocyte egress. In fact, DC depletion alone can elicit neutrophilia (Figure S2C, top)[120,249,250], and normalization of cellularity in draining LNs to non-draining LNs revealed an even greater diminishment in neutrophil recruitment when DCs were ablated (Figure S2C, bottom). To further control for any differences in the circulating cells, wildtype bone marrow cells were i.v.-injected into immunized Zbtb46-DTR chimeras, with or without DT treatment. Again, we found a significant decrease in the total number of transferred neutrophils and monocytes within draining LNs of DC-depleted mice (Figure S2D). Of note, neutrophil and monocyte trafficking to the peripheral skin site of immunization remained intact in the absence of DCs (Figure S2E), consistent with described roles for other cell types in promoting entry into peripheral tissues[251-253]. This indicates that innate cell trafficking is not lost at all sites of inflammation upon DC ablation, but rather that DCs selectively regulate innate cell recruitment into the draining LNs. We also evaluated whether other cell populations were affected by the lack of DCs. B cell cellularity was modestly affected in inflamed LNs after DC depletion, but otherwise, no consistent patterns emerged for other studied cell types

(Figure 2C). Importantly, naïve T cell trafficking remained largely unaltered in the absence of DCs. Therefore, although prolonged ablation of DCs can result in dysfunctional HEVs[33], short-term depletion does not, as previously noted[84,254,255].

We next assessed whether DC depletion affected innate cell localization within the draining LNs. As above, DC ablation resulted in significant decreases in the overall density of neutrophils and monocytes within the LNs (Figures 2D–2G). In addition, we observed marked changes in the positioning of the recruited cells. In contrast to controls, in which neutrophils and monocytes robustly infiltrated the LN parenchyma during immunization, in DC-depleted tissues the cells remained more closely associated with HEVs and displayed impaired migration into the T cell zone. Moreover, the polarized distribution of innate cells across the LN was significantly diminished. Of note, monocytes in DC-depleted mice effectively entered the T cell zone by 24 hours, suggesting secondary mechanisms of monocyte control, such as via stromal cells[230]. Nevertheless, a greater proportion of the monocytes exhibited a rounded morphology (Figure S2F) as well as had reduced surface expression of CD11c and MHC-II (Figure S2G) with DC depletion. This suggests that in addition to coordinating their recruitment, DCs help promote monocyte differentiation, either directly or indirectly, such as by facilitating NK cell crosstalk[156]. In fact, when we examined NK cell localization, we found that in contrast to control immunized tissues, in which NK cells repositioned into the T cell zone, NK cells were largely retained within the outer periphery of DC-ablated LNs (Figures 2H and 2I). Collectively, these data show that DCs regulate the recruitment and localization of multiple innate effector cell populations within the draining LNs, as well as drive the establishment of tissue polarity during inflammation.

Given the close correspondence of resident DCs with innate cell distribution across the LN, we reasoned that as the DCs repositioned from the outer periphery, through the HEV-rich regions,

and into the deep T cell zone, they concurrently provided local guidance cues to recruit innate effector cells. Resident DCs utilize the chemotactic receptor CCR7 to migrate into the T cell zone during inflammation[28]. To test whether the positioning of innate effector cells was linked to that of DCs, we conditionally ablated CCR7 expression on DCs by generating 50:50 mixed bone marrow chimeras, consisting of Zbtb46-DTR and either wildtype or CCR7.KO donors. These chimeric animals maintain normal lymphoid architecture while depletion of DCs from Zbtb46-DTR origin leaves either the wildtype (DC-WT) or CCR7.KO (DC-CCR7.KO) DCs intact. Chimeras were treated with DT and immunized with CpG. Recapitulating prior findings[28], CCR7-deficient resident DCs were significantly impaired in their ability to reposition into the T cell zone and instead remained localized in the outer paracortex, in closer proximity to HEVs (Figures S2H and S2I). As expected, migratory DCs were also absent in DC-CCR7.KO LNs while the number of resident DCs was unaffected. Notably, disruption of resident DC positioning was associated with misdirected innate cell localization. As with the resident DCs, the percentages of neutrophils, monocytes, and NK cells within the T cell zone were all significantly diminished in DC-CCR7.KO LNs, and instead these cells accumulated in the outer periphery of the tissue and were closer to HEVs (Figures S2H and S2J–S2L). No major differences in the abundances of neutrophils, monocytes, and NK cells were detected. These data demonstrate that CCR7-dependent repositioning of DCs within inflamed LNs regulates the localization of the innate effector cells.

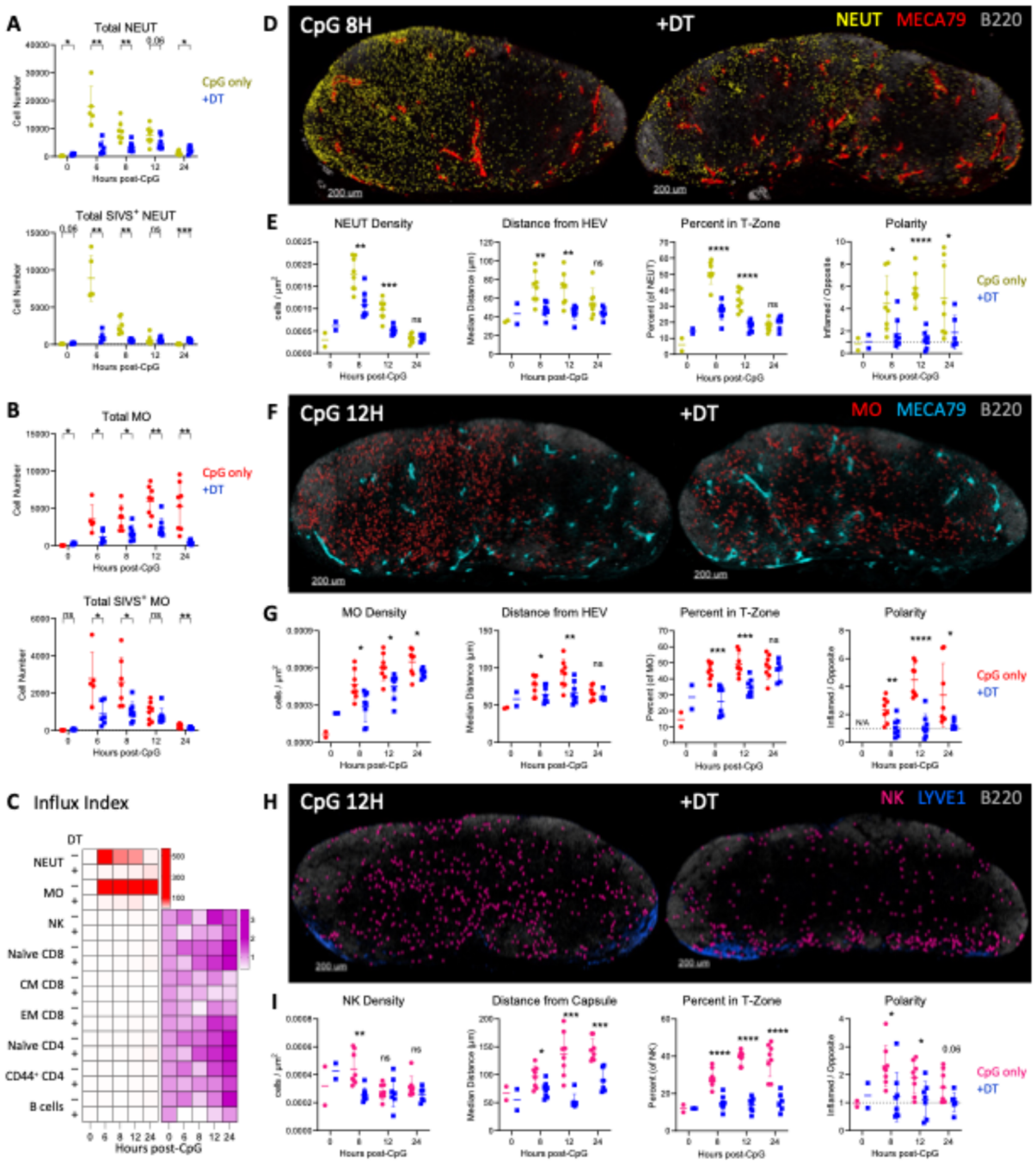

Figure 2. DCs regulate innate cell trafficking and LN organization during inflammation. (A to C) Zbtb46-DTR bone marrow chimeras were immunized with CpG, and some mice were also treated with DT 4 hours prior to ablate DCs. 3 hours before harvest, SIVS was performed to label cells infiltrating the tissues from circulation. Draining LNs were assessed by flow cytometry at multiple time points. Quantification of total and SIVS$^+$ (A) neutrophils and (B) monocytes. (C) Influx index for the indicated cell types. (D to I) Zbtb46-DTR chimeras were immunized with CpG, with or without DT treatment. Draining LNs were evaluated via microscopy and histo-cytometry at various time points. Representative images as well as quantifications of density, localization, and polarity across the tissue for (D and E) neutrophils, (F and G) monocytes, and (H and I) NK cells. All graphs show mean ± SD and were analyzed using unpaired

t test with Welch's correction. **** $P \leq 0.0001$; *** $P \leq 0.001$; ** $P \leq 0.01$; * $P \leq 0.05$; not significant (ns) $P > 0.05$. All data are representative of at least two independent experiments.

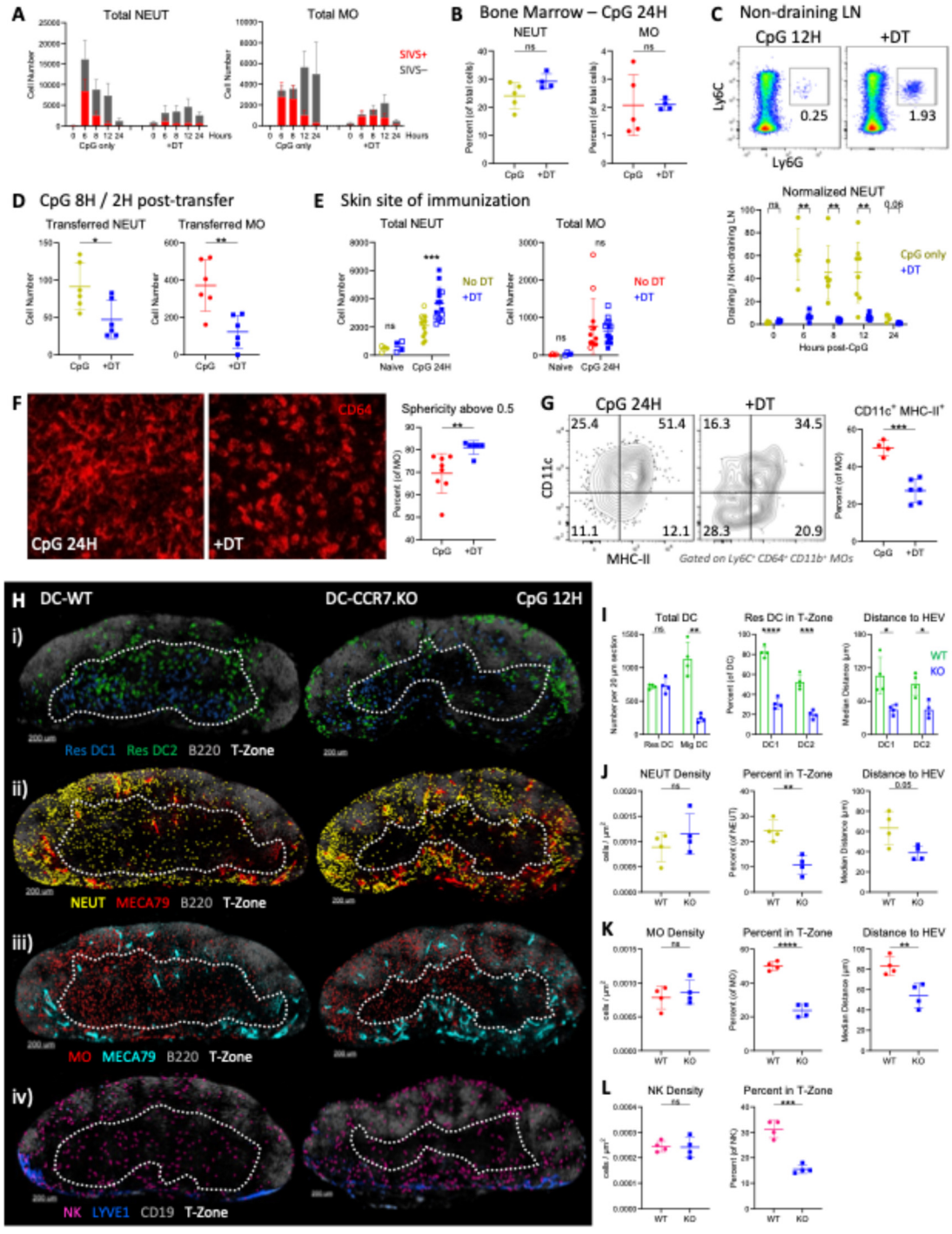

Figure S2. DCs facilitate innate cell migration in draining LNs but not other sites.
(A) Supplemental data for Figures 2A and 2B. Kinetics of $SIVS^+$ (recently infiltrated) and $SIVS^-$ (in parenchyma at time of labeling) neutrophils and monocytes in draining LNs of CpG-immunized Zbtb46-DTR chimeras, with or without DT treatment. (B) Neutrophil and monocyte abundance in the bone marrow of Zbtb46-DTR chimeras, analyzed by flow cytometry 24 hours post-immunization. (C) Supplemental data for Figure 2A. Representative flow plots of neutrophils in non-draining LNs, with or without DT (top). To

account for neutrophilia induced by DT injection, the number of neutrophils in draining LNs was divided by the number of neutrophils in non-draining LNs (bottom). (D) Zbtb46-DTR chimeras were immunized with CpG, with or without DT treatment. 6 hours later, chimeras were i.v. transferred bone marrow cells from wildtype mice. Total numbers of transferred neutrophils and monocytes in draining LNs were enumerated via flow cytometry 2 hours later. (E) Zbtb46-DTR chimeras were immunized with CpG. Neutrophil and monocyte cellularity in the skin site of immunization was quantified by flow cytometry 24 hours later. Data are pooled from two experiments, denoted by different symbols. (F and G) Zbtb46-DTR chimeras were immunized with CpG. 24 hours later, (F) monocyte sphericity as well as (G) CD11c and MHC-II surface expression was measured using histo-cytometry and flow cytometry, respectively. (H to L) DC-WT and DC-CCR7.KO mixed bone marrow chimeras were treated with DT. One day later, chimeras were immunized with CpG along with another injection of DT. Innate cell distribution in draining LNs was assessed via imaging and histo-cytometry 12 hours after immunization. (H) Representative images showing the localization of (i) resident DCs, (ii) neutrophils, (iii) monocytes, and (iv) NK cells. Dotted line demarcates the T cell zone. (I) Total numbers of resident and migratory DCs per imaged section, percent of resident DCs in the T cell zone, as well as the median distance of resident DCs from HEVs. (J) Neutrophil, (K) monocyte, and (L) NK cell density in the LN as well as quantification of their localization. All graphs show mean ± SD and were analyzed using unpaired *t* test with Welch's correction. **** $P \leq 0.0001$; *** $P \leq 0.001$; ** $P \leq 0.01$; * $P \leq 0.05$; not significant (ns) $P > 0.05$. Data in (A to C), and (F to L) are representative of at least two independent experiments. In (B), (D), (E), and (G), DT or PBS control was administered at the time of immunization.

DCs generate a rich haptotactic matrix to facilitate innate effector cell migration

We next aimed to understand the molecular mechanisms by which DCs regulate innate cell trafficking and localization. To do so, we first conducted RNA sequencing to identify genes that were expressed by resident DCs during early inflammation. Resident DC1s and DC2s were sorted from LNs at steady state as well as 6 hours post-CpG administration, a time point of peak innate cell recruitment via HEVs. We also performed intravascular staining with fluorescent anti-CD11c antibody to further sort on vasculature-associated and non-associated populations, to ask whether there were differences based on proximity to blood vessels. As expected, multiple genes related to inflammatory signaling and activation were expressed by both DC subsets upon immunization (Dataset S1). Notably, the resident DCs upregulated the expression of numerous inflammatory chemokines (Figure 3A), including those with known roles in regulating monocyte, neutrophil, and NK cell trafficking (CCL5, CXCL1, CXCL2, CXCL9, and CXCL10)[233,256-260]. These chemokines varied in expression between DC1s and DC2s, albeit differences between vasculature-associated and non-associated DCs were minor. Additional attractants implicated in neutrophil

trafficking[21,181,220] were also noted (Figures S3A and S3B). We next verified chemokine production by resident DCs at the protein level using flow cytometry. Consistent with the RNA sequencing data, resident DCs from CpG-immunized LNs showed significantly increased expression of all examined chemokines compared with those from naïve LNs (Figure S3C). Imaging of LN sections further confirmed that there was heightened chemokine signal associated with resident DCs following immunization (Figure 2B). To test the contribution of DCs in the production and spatial dispersal of these chemokines, we next visualized draining LNs from immunized Zbtb46-DTR chimeric mice by microscopy. CpG administration induced marked expression of multiple inflammatory chemokines throughout the LN parenchyma in a highly polarized manner (Figure 3C). Ablation of DCs led to a significant loss of chemokine expression, both across the LN and along the blood vessels (Figures 3C and S3D). Of note, CXCL9 was not altered by DC depletion (Figure S3E), indicating that DCs are not a dominant source of this chemokine and other cell populations contribute[24,187]. In addition, the homeostatic chemokine CCL21, which is stromal-derived, was not markedly affected by the absence of DCs. All in all, these data indicate that during inflammation DCs generate a polarized gradient of inflammatory chemokines within the draining LNs.

Chemokine sensing by cells induces integrin activation and interactions with integrin ligands. Neutrophils and monocytes utilize the integrin ligand ICAM-1 expressed on endothelial cells and pericytes for extravasation into tissues[123]. Notably, DCs also express ICAM-1, which further increases after maturation. Moreover, ICAM-1 expression by DCs has been shown to promote high-speed, directional migration of naïve T cells into the T cell zone in steady state tissues[261]. We thus hypothesized that enhanced ICAM-1 expression by DCs during inflammation, coupled with local chemokine production, could facilitate innate cell trafficking into the LN

parenchyma. Supporting this notion, resident DCs rapidly upregulated ICAM-1 at both gene and protein levels after CpG immunization (Figures 3D and S3F). Visualization of LNs by microscopy further confirmed that, in addition to ICAM-1 expression on blood endothelial cells, DCs in draining LNs robustly expressed ICAM-1, forming an adhesion molecule-rich matrix extending from the HEVs and surrounding perivascular sheath into the deeper paracortex (Figures 3E and S3G). To test whether ICAM-1 expression on DCs contributes to innate cell trafficking, we generated 50:50 mixed bone marrow chimeras consisting of Zbtb46-DTR bone marrow, mixed with either wildtype or ICAM-1.KO bone marrow. DT treatment allowed ablation of DCs from Zbtb46-DTR origin, leaving only DCs derived from wildtype (DC-WT) or ICAM-1.KO (DC-ICAM-1.KO) donors (Figure S3H). No major differences in the total number of DCs or the positioning of resident DCs were detected between DC-WT and DC-ICAM-1.KO mice (Figures S3H and S3I). We next enumerated leukocyte recruitment during CpG immunization by flow cytometry. SIVS was performed 3 hours prior to harvest to label cells that had recently infiltrated from circulation. Compared with DC-WT controls, the total number of neutrophils and monocytes, as well as their SIVS-labeled counterparts, were significantly reduced in DC-ICAM-1.KO draining LNs 6 and 8 hours after CpG administration (Figures 3F and S3J). No difference was observed between groups at later time points. This suggests that although other cellular sources of ICAM-1 and additional adhesion molecules also play a role in neutrophil and monocyte entry into inflamed LNs[123], ICAM-1 expression on DCs supports the efficiency of this process. We next assessed the localization of the innate effector cells by quantitative imaging. This revealed that in addition to reduced neutrophil and monocyte density in DC-ICAM-1.KO LNs, for the cells that did enter, they were more proximal to the HEVs and less able to migrate into the deep T cell zone (Figures 3G–

3I). Hence, these data show that DC expression of ICAM-1 facilitates efficient innate cell entry and migration across the LN parenchyma.

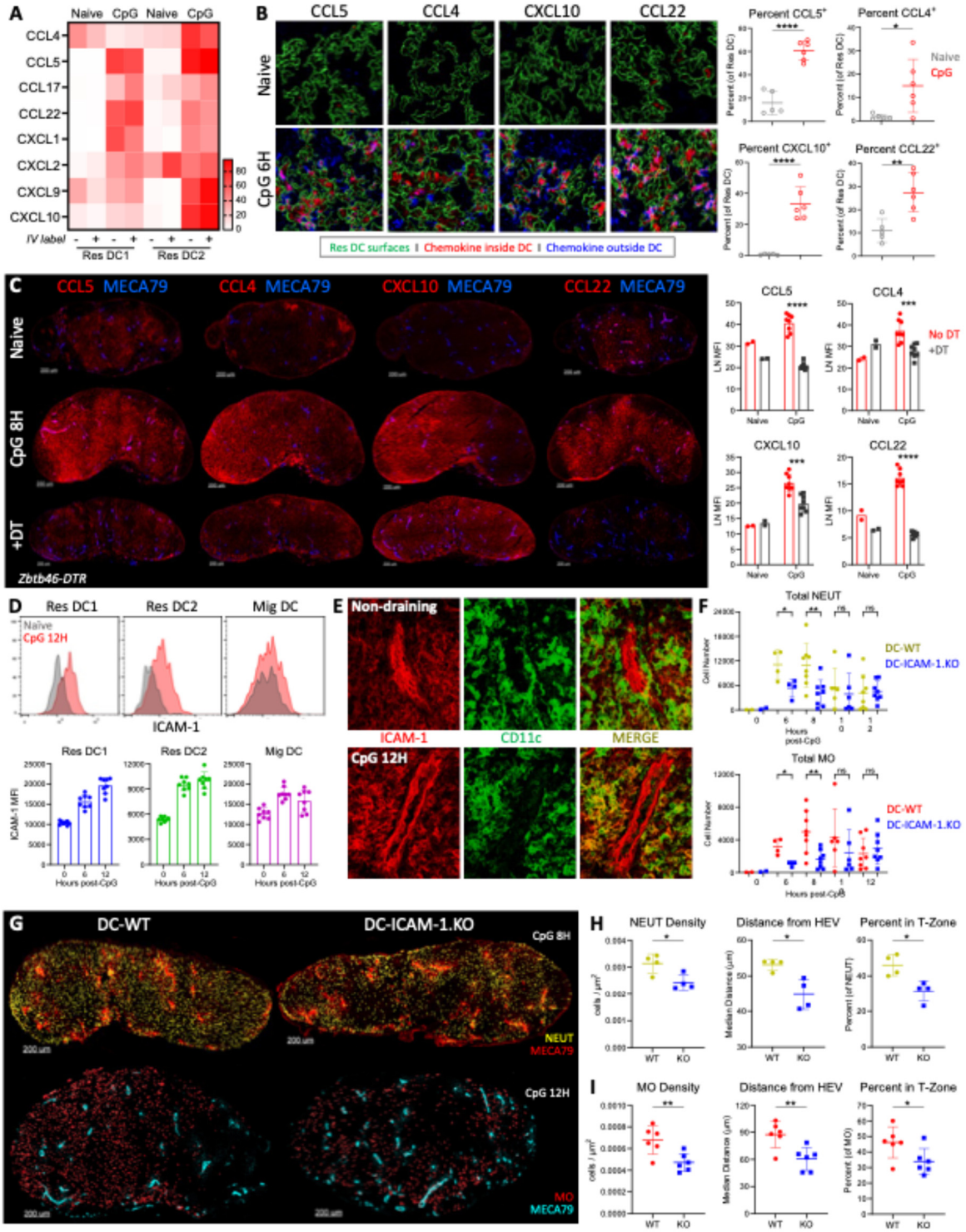

Figure 3: DCs generate a chemokine- and adhesion molecule-rich matrix which supports innate cell infiltration.
(A) B6 mice were immunized with CpG and administered CD11c–PE i.v. 30 minutes before harvest to label vasculature-associated DCs. Resident DC1s and DC2s (IV^- and IV^+) were sorted from draining LNs 6 hours post-immunization or from naïve LNs for RNA sequencing. Heatmap depicts normalized transcript abundance for the chemokines upregulated in immunized mice (>2× fold change). Expression for each chemokine is normalized to its range. (B) Representative images of chemokine signal localized inside or outside of resident DC surfaces in naïve or immunized LNs (left). Histo-cytometry quantification of chemokine expression by resident DCs (right). (C) Zbtb46-DTR chimeras were immunized with CpG, with or without DT treatment. Chemokine expression in draining LNs was evaluated by imaging and histo-cytometry at 8 hours. Representative images depicting the spatial dispersal of the specified chemokines across the LNs (left) and quantification of the mean fluorescence intensity (MFI) for the chemokines across the entire LN (right). (D and E) B6 mice were immunized with CpG and ICAM-1 expression on DCs was assessed by (D) flow cytometry and (E) imaging at specified time points. (F to I) DC-WT and DC-ICAM-1.KO mixed bone marrow chimeras were treated with DT. One day later, chimeras were immunized with CpG along with another injection of DT. (F) SIVS was also performed 3 hours before tissue harvest. Neutrophil and monocyte cellularity in draining LNs was measured by flow cytometry at the indicated time points. (G) Representative images and (H and I) quantification of neutrophil and monocyte density and localization. All graphs show mean ± SD and were analyzed using unpaired *t* test with Welch's correction. **** $P \leq 0.0001$; *** $P \leq 0.001$; ** $P \leq 0.01$; * $P \leq 0.05$; not significant (ns) $P > 0.05$. All data are representative of at least two independent experiments.

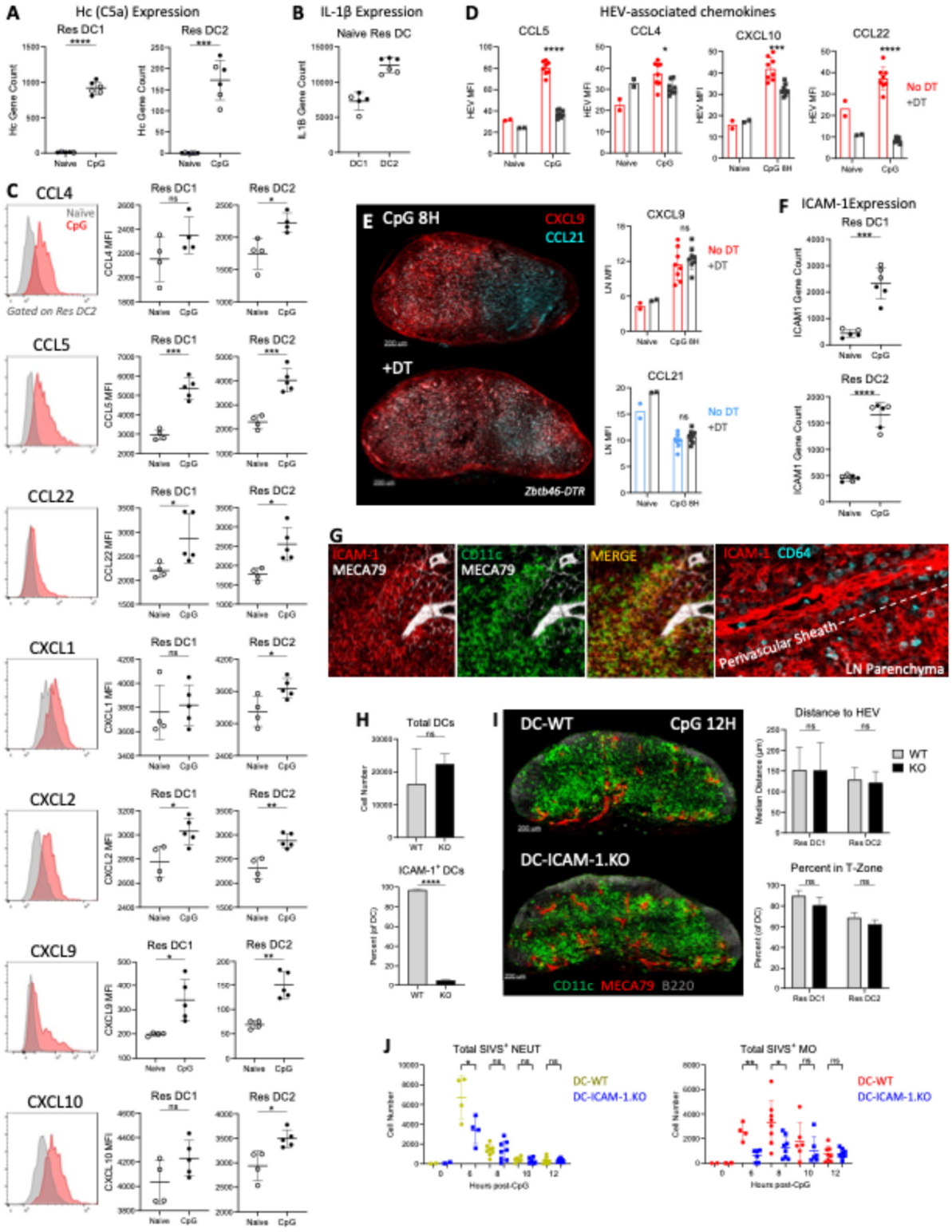

Figure S3: DCs create haptotactic scaffolds across the LN parenchyma.
(A) Gene expression of Hc (hemolytic complement), which can be proteolytically processed to generate C5a, was measured in resident DC subsets from naïve LNs and 6 hours post-CpG immunization. (B) IL-1β gene expression by resident DCs from naïve LNs. (C) Chemokine expression by resident DCs from naïve

and CpG-immunized LNs was assessed using flow cytometry. Representative histogram of chemokine production by resident DC2s (left) as well as quantification of chemokine MFI in resident DC1s and DC2s (right). (D and E) Zbtb46-DTR chimeras were immunized with CpG, with or without DT treatment, and chemokine expression in draining LNs was evaluated by imaging and histo-cytometry 8 hours later. (D) Supplemental data for Figure 3C. Quantification of chemokine MFI on HEVs. (E) Representative images and quantification of CXCL9 and CCL21 expression across the LN. (F) ICAM1 gene expression by resident DC subsets from naïve LNs and 6 hours post-CpG immunization. (G) Images showing ICAM-1 expression on $CD11c^+$ DCs extending from the HEVs into the deeper paracortex (left) and in relation to infiltrating $CD64^+$ monocytes (right) in draining LNs 12 hours after CpG immunization. (H and I) Validation of DC-WT and DC-ICAM-1.KO mixed bone marrow chimera model. Chimeras were treated with DT and one day later, immunized with CpG along with another injection of DT. (H) Total DCs in draining LNs and their surface expression of ICAM-1 was assessed by flow cytometry. (I) Representative images demonstrating CD11c-high cell distribution (left) and quantification of resident DC localization in draining LNs by histo-cytometry. (J) Supplemental data for Figure 3F. Total number of $SIVS^+$ neutrophils and monocytes in DC-WT versus DC-ICAM-1.KO draining LNs. For (A), (B), and (F), full experimental design in Figure 3A. Closed circles identify IV^+ vasculature-associated DCs; open circles denote $IV^–$ vasculature non-associated DCs. All graphs show mean ± SD and were analyzed using unpaired *t* test with Welch's correction. **** $P \leq 0.0001$; *** $P \leq 0.001$; ** $P \leq 0.01$; * $P \leq 0.05$; not significant (ns) $P > 0.05$. All data are representative of at least two independent experiments.

DC2s promote innate cell trafficking into the T cell zone

DC1s and DC2s have distinct responses to inflammatory stimuli[36,200]. Of relevance, we noted differences between subsets in their expression of chemokines and ICAM-1, as well as their association with LN blood vessels. Furthermore, spatial correlation analysis showed that the recruited innate effector cells were positively correlated with resident DC2s but not DC1s (Figure 4A). Therefore, we investigated whether there were distinct roles for DC1s and DC2s in regulating innate cell trafficking. To test this, we first used $CD11c^{Cre}$ $IRF4^{fl/fl}$ mice, in which DC2 development and/or maturation is impaired[144,262]. Previous characterizations have established that IRF4 is critical for migratory DC2 maturation and migration into skin-draining LNs[262]. Consistent with this paradigm, we found that in comparison with $Cre^–$ controls ($IRF4^{WT}$), the abundance of migratory DC2s within naive LNs was significantly reduced in Cre^+ ($IRF4^{cKO}$) mice, with no difference observed in the total number of resident DC2s, resident DC1s, or migratory DC1s (Figure S4A). Given that LN-resident DC2s also undergo maturation and CCR7-dependent intranodal migration into the T cell zone in settings of type-I inflammation[28], we next ascertained

whether IRF4 similarly modulates resident DC2 activation and localization after CpG immunization. Indeed, resident DC2 maturation was partially yet significantly impaired in IRF4^{cKO} mice, with no differences observed for resident DC1s (Figure S4B). Notably, there was decreased expression of CCR7 in the resident DC2s (Figure 4B). Accordingly, the percentage of resident DC2s within the T cell zone was significantly reduced in IRF4^{cKO} LNs, and these cells instead positioned more in the outer paracortex and in closer proximity to HEVs (Figures 4C and 4D). We next evaluated how these changes in DC2s influenced innate cell localization. We found that in IRF4^{cKO} mice, infiltrating neutrophils and monocytes were located closer to the HEVs and their recruitment into the T cell zone was significantly impaired (Figures 4C, 4E, and 4F). Likewise, NK cell repositioning into the T cell zone was diminished (Figures 4C and 4G). No major differences in the total numbers of neutrophils, monocytes, and NK cells were observed (Figure S4C). This may reflect the partial maturation of resident DC2s or the fact that they still localized near HEVs. Alternatively, it suggests that DC1s may provide the primary cues for innate cell entry. We therefore tested the role of DC1s in this process using BATF3.KO mice, which lack DC1s[263]. No major defect in innate cell trafficking was observed in BATF3.KO draining LNs, and if anything, there was an increase in the number of recruited cells (Figures S4D–S4G). Such increases could potentially be due to either direct roles for DC1s in suppressing innate cell trafficking[264], or indirect effects through their regulation of DC2 function and localization[72,265]. In support of the latter, BATF3.KO mice exhibited increased abundance of DC2s within the T cell zone (Figures S4E and S4H). Altogether, these data indicate that DC2s play a dominant role in promoting innate cell trafficking into the T cell zone during inflammation.

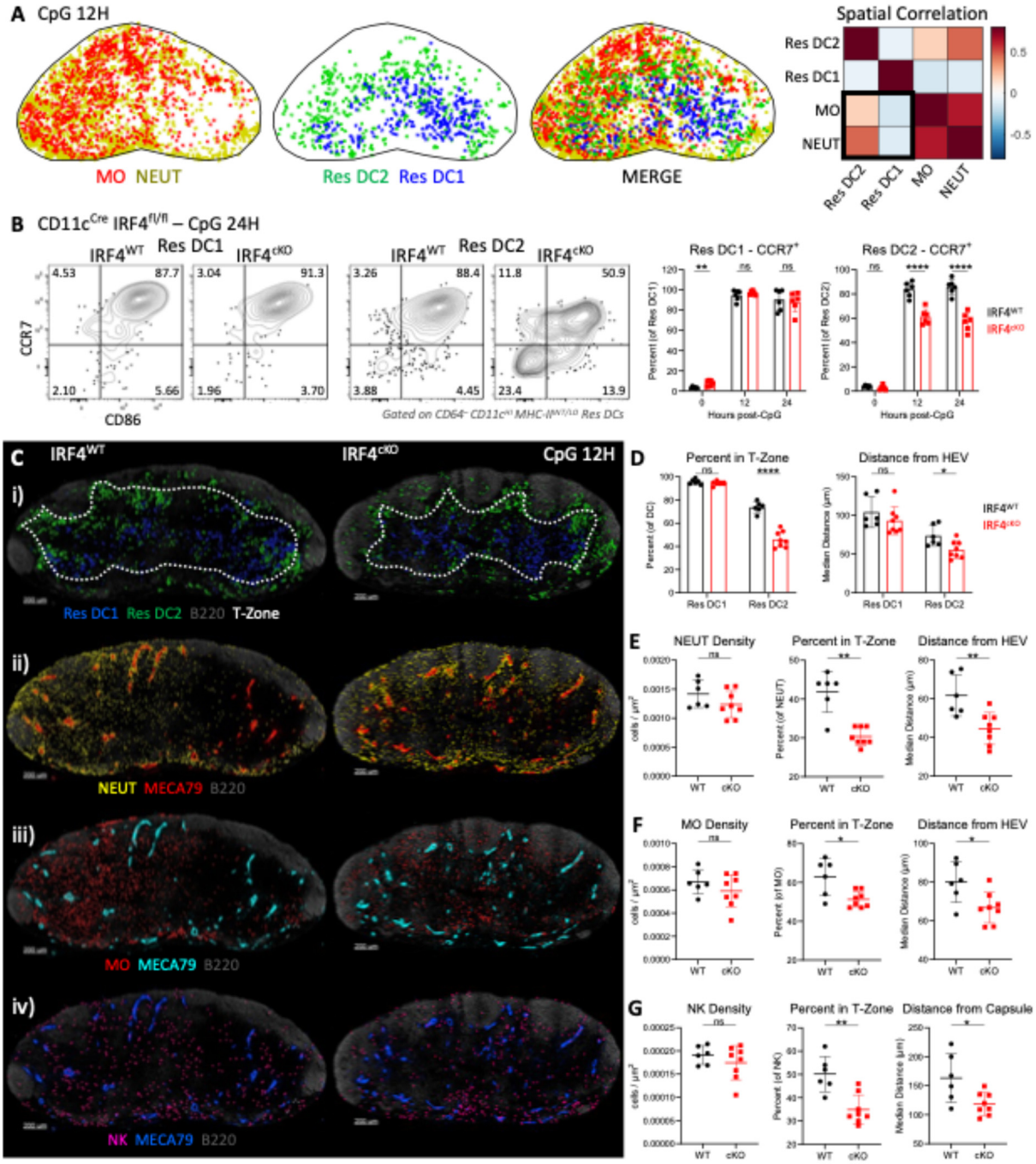

Figure 4: DC2s promote innate cell recruitment into the T cell zone.
(A) B6 mice were immunized with CpG and draining LNs were imaged 12 hours later. The spatial correlation between resident DC subsets and innate effector cells within the paracortex was assessed. (B to G) CD11c^{Cre} IRF4$^{fl/fl}$ mice were immunized with CpG, and Cre^{-} (IRF4^{WT}) versus Cre^{+} (IRF4^{cKO}) draining LNs were evaluated at the indicated time points. (B) CCR7 expression by resident DCs as assessed via flow cytometry. (C) Representative images of (i) resident DC, (ii) neutrophil, (iii) monocyte, and (iv) NK cell localization within the LNs, as well as (D to G) quantification of their positioning using histo-cytometry. Dotted line in images demarcates the T cell zone. All graphs show mean ± SD and were analyzed using

unpaired *t* test with Welch's correction. **** $P \leq 0.0001$; ** $P \leq 0.01$; * $P \leq 0.05$; not significant (ns) $P > 0.05$. All data are representative of at least two independent experiments.

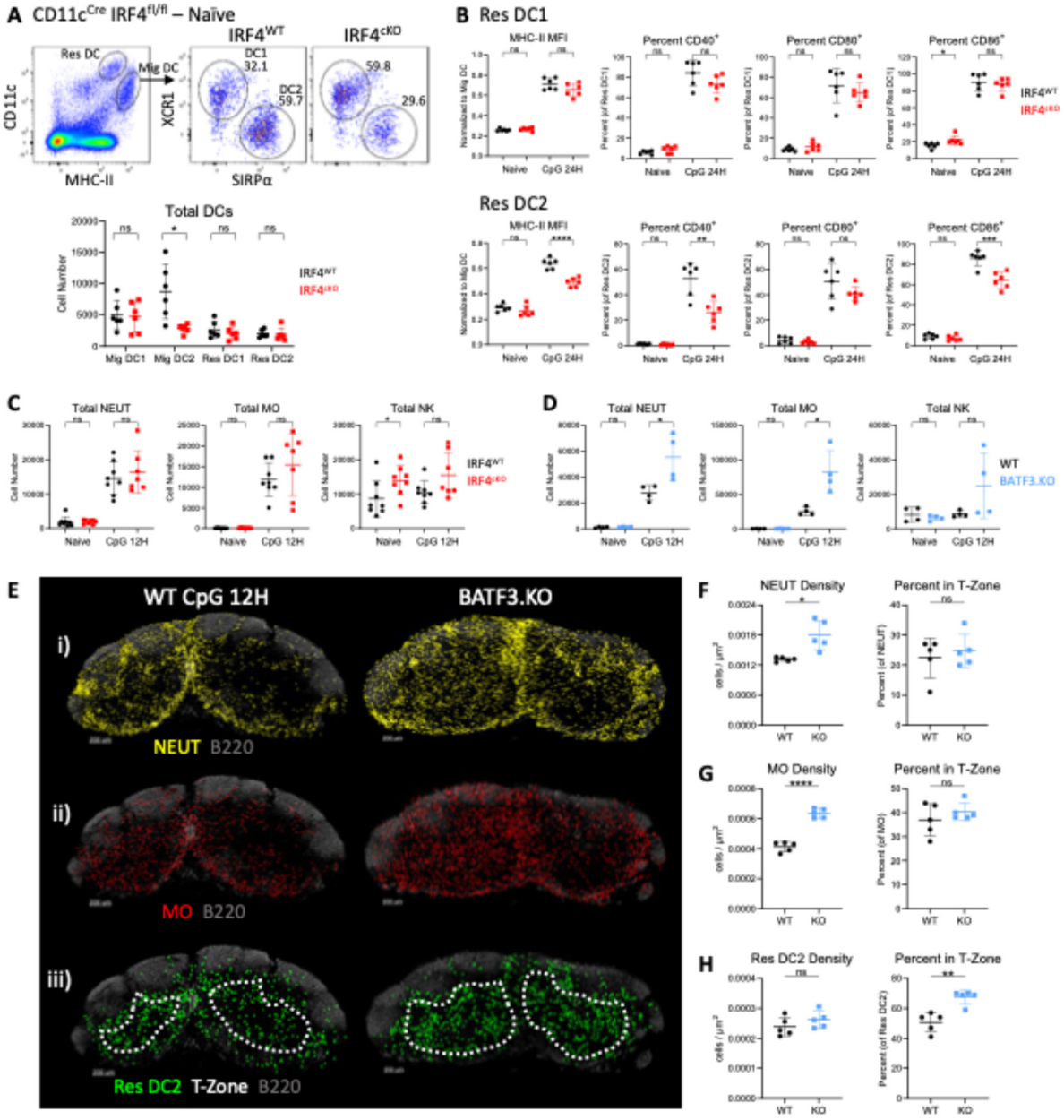

Figure S4: Innate cell trafficking remains intact in the absence of DC1s.
(A) Naïve LNs from CD11c^{Cre} IRF4$^{fl/fl}$ mice were harvested for flow cytometry. DC cellularity in Cre^{-} (IRF4^{WT}) versus Cre^{+} (IRF4^{cKO}) conditions was quantified. Flow plots were pre-gated on CD3^{-} CD19^{-} NK1.1^{-} Ly6G^{-} CD64^{-} cells. (B and C) CD11c^{Cre} IRF4$^{fl/fl}$ mice were immunized with CpG and draining LNs were assessed by flow cytometry at the indicated time points. (B) Expression of MHC-II and costimulatory molecules by resident DC1s and DC2s. (C) Total numbers of neutrophils, monocytes, and NK cells within the LNs. (D to H) Wildtype (WT) and BATF3.KO mice were immunized with CpG and draining LNs were evaluated 12 hours later. (D) Total numbers of neutrophils, monocytes, and NK cells enumerated via flow cytometry. (E) Representative images of (i) neutrophil, (ii) monocyte, and (iii) resident DC2 localization,

as well as (F to H) quantification of their density and frequency within the T cell zone. Dotted line in images demarcates the T cell zone. All graphs show mean ± SD and were analyzed using unpaired *t* test with Welch's correction. **** $P \leq 0.0001$; *** $P \leq 0.001$; ** $P \leq 0.01$; * $P \leq 0.05$; not significant (ns) $P > 0.05$. All data are representative of at least two independent experiments.

DCs are critical for optimized innate control of disseminating pathogens within the draining LNs

We next studied the functional consequences of these responses. We hypothesized that during microbial infection of peripheral tissues, DC-driven recruitment of innate effector cells into draining LNs would be critical for limiting downstream pathogen dissemination. One such pathogen is *P. aeruginosa*, which after skin infection, is rapidly transported into LNs and elicits innate cell responses important for limiting its systemic spread[21]. To interrogate whether DCs play a role in these processes, Zbtb46-DTR chimeras were infected with *P. aeruginosa* expressing GFP, with or without DT injection. We first assessed neutrophil recruitment, which is essential for pathogen containment[21,182,183]. Unlike CpG immunization settings, DC depletion did not significantly affect neutrophil cellularity within draining LNs at 8 hours post-infection (Figure S5A), consistent with past findings that other factors can initiate neutrophil recruitment in this model[21,182]. Regardless, we did observe marked alterations to neutrophil positioning in DC-depleted LNs. In control tissues, neutrophils rapidly formed an extensive and dense cellular aggregate, akin to a barrier, which began at the subcapsular sinus and extended into the T cell zone (Figure 5A). This was associated with tight sequestration of the bacteria within the neutrophils at the subcapsular sinus (Figure 5A, zoom-in panels), reflecting effective pathogen containment. In contrast, in the absence of DCs, neutrophils appeared more dispersed at the subcapsular sinus and instead preferentially accumulated in smaller aggregates near the HEVs and outer paracortex (Figures 5A and 5B). Moreover, more bacteria were localized outside of the neutrophils (Figures

5A, zoom-in panels, and 5C), showing inefficient early immune control over the infection, and supporting the notion that appropriate neutrophil swarming is essential for bacterial containment[183].

We also investigated whether DCs impacted other innate effector cell types. We found that ablation of DCs resulted in a significant decrease in the total number of monocytes within draining lymph nodes (Figure S5A), indicating that DCs regulate monocyte recruitment during both CpG immunization and *P. aeruginosa* infection. Inspection of monocyte and NK cell localization 12 hours post-infection further revealed that the positioning of these innate effector cells was disrupted (Figures S5B–S5E). In control infection settings, monocytes infiltrated the T cell zone, while NK cells accumulated at both the subcapsular sinus and T cell zone. Conversely, with DC depletion, a higher proportion of monocytes were found near the HEVs and outer paracortex, while more NK cells were retained within the medulla.

In addition to individual cell populations, we also evaluated broader antimicrobial functions of the tissue. Rapid IFNγ production by lymphocytes has previously been shown to help fortify local innate defense for enhanced bacterial control[21]. To examine this pathway, we stained for iNOS, a potent antimicrobial mediator directly downstream of IFNγ signaling. We found that 16 hours after *P. aeruginosa* infection, iNOS was highly expressed both at the subcapsular sinus as well as deeper regions of the LN (Figures S5F and S5G). In stark contrast, iNOS was significantly diminished in DC-depleted LNs, indicating that DCs play a critical role in propagating IFNγ-induced antimicrobial functions across the tissue.

Finally, to test whether these diverse DC-regulated innate responses contribute to host protection, we measured total colony-forming units (CFU) in the draining LNs and spleen 16 hours post-infection. We found that ablation of DCs resulted in a significantly greater bacterial burden in the draining LNs as well as increased dissemination of the bacteria into the spleen (Figure 5D).

Collectively, these findings demonstrate that DCs promote multiple layers of innate defense to control and contain disseminating bacterial pathogens.

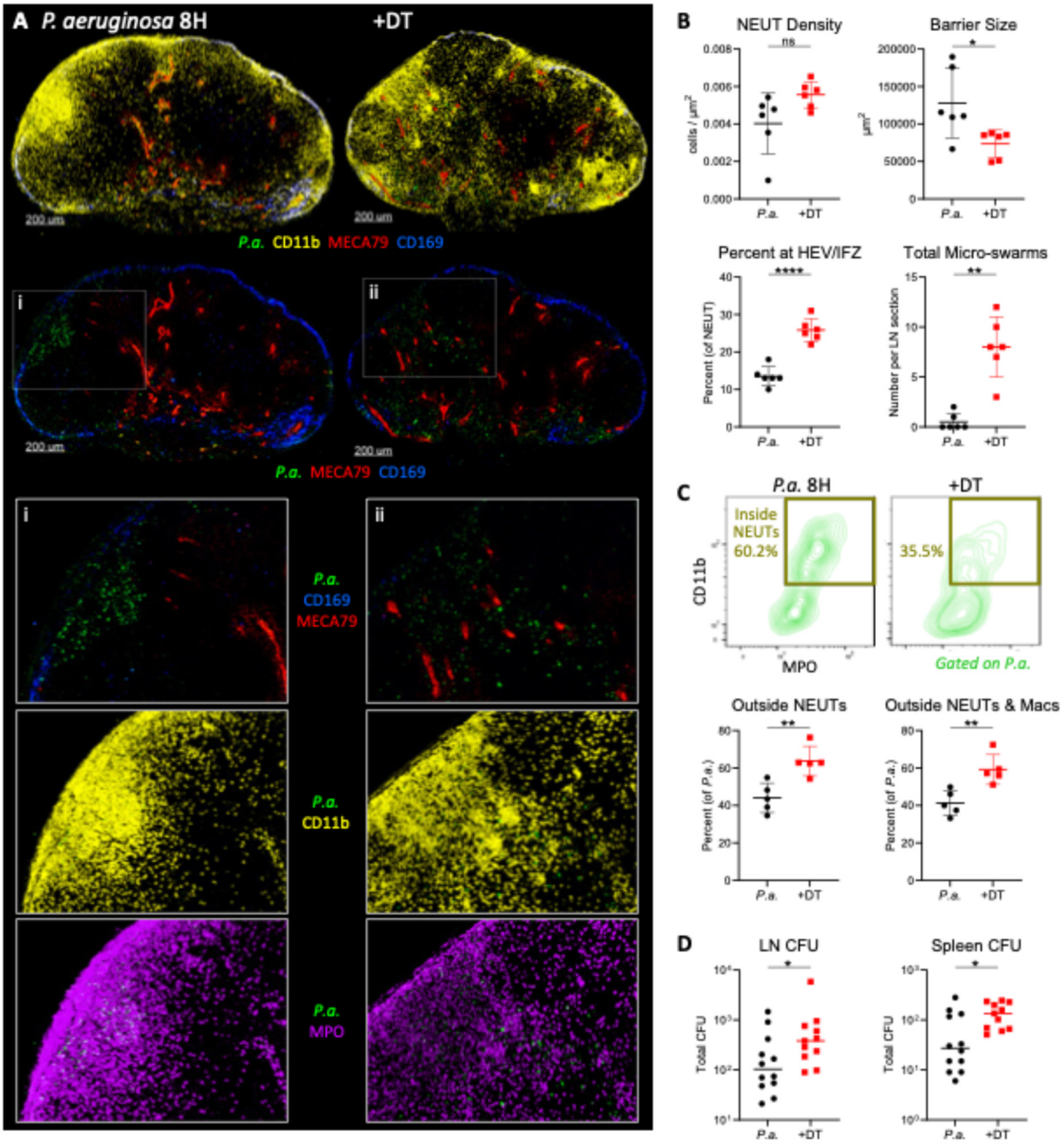

Figure 5: DCs play a critical role in innate defense against disseminating pathogens
Zbtb46-DTR chimeras were infected with GFP expressing *P. aeruginosa* (*P.a.*), with or without DT treatment. (A to C) Draining LNs were visualized by microscopy 8 hours later. (A) Representative images of MPO^+ $CD11b^+$ neutrophil recruitment. Insets show *P. aeruginosa* spread with respect to neutrophils. (B) Histo-cytometry analysis of neutrophil density and distribution in draining LNs. Neutrophil barrier defined as $CD11b^+$ MPO^+ $CD64^-$-dense region extending from the subcapsular sinus into the interfollicular zone.

(C) Representative histo-cytometry plots and quantification of the percent of *P. aeruginosa* localized inside or outside neutrophils (MPO^+ $CD11b^+$) and macrophages ($CD64^+$ or $CD169^+$). (D) Total CFU in the draining LNs and spleen 16 hours after infection. Graphs in (B) and (C) show mean ± SD and were analyzed using unpaired *t* test with Welch's correction. In (D), median is shown, and data was analyzed using Mann-Whitney test. **** $P \leq 0.0001$; ** $P \leq 0.01$; * $P \leq 0.05$; not significant (ns) $P > 0.05$. All data are representative of at least two independent experiments.

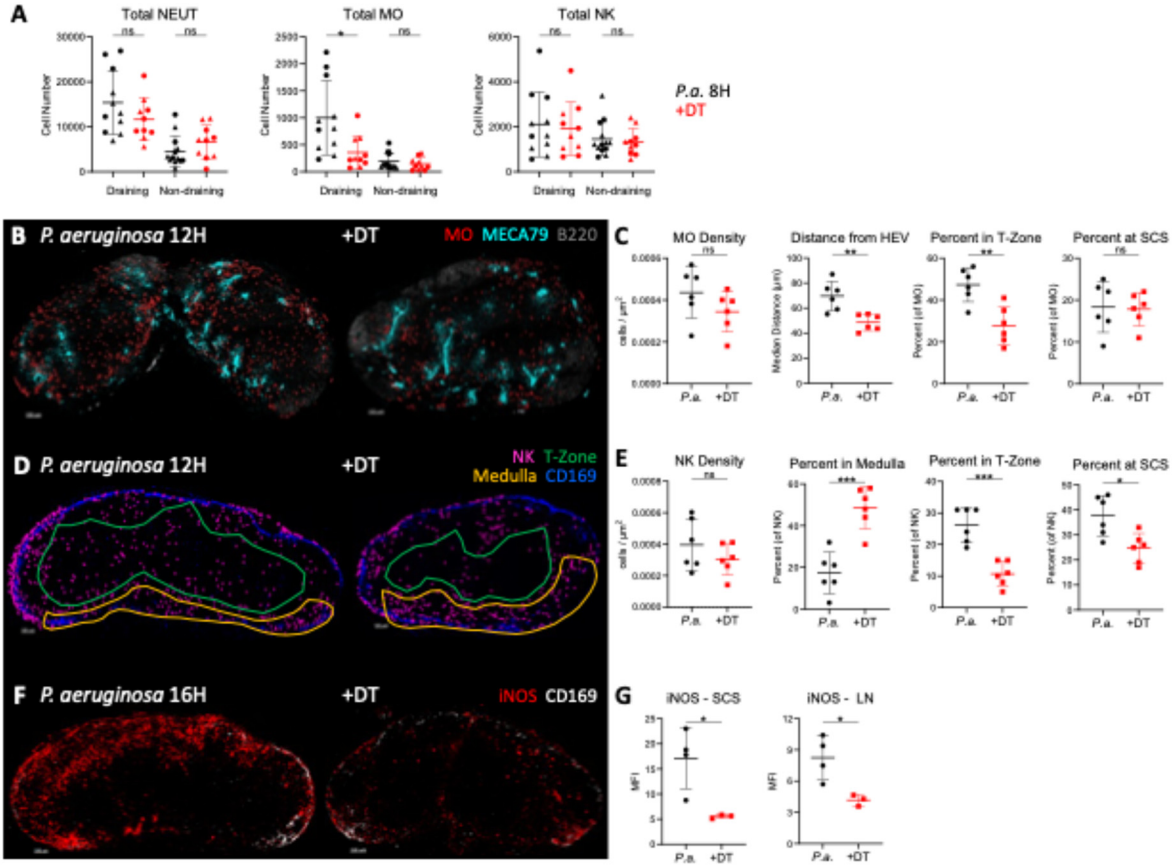

Figure S5: DCs regulate multiple components of the innate response during infection.
Zbtb46-DTR chimeras were infected with GFP expressing *P. aeruginosa*, with or without DT treatment. (A) Total numbers of neutrophils, monocytes, and NK cells in draining and non-draining LNs, enumerated via flow cytometry 8 hours post-infection. (B to G) Draining LNs were visualized by microscopy and quantified via histo-cytometry. Representative images and quantification of (B and C) monocyte and (D and E) NK cell density and localization 12 hours after infection. (F) Representative images and (G) MFI of iNOS expression at the subcapsular sinus as well as across the entire LN 16 hours following infection. All graphs show mean ± SD and were analyzed using unpaired *t* test with Welch's correction. *** $P \leq 0.001$; ** $P \leq 0.01$; * $P \leq 0.05$; not significant (ns) $P > 0.05$. All data are representative of at least two independent experiments.

Extensive innate cell influx disrupts LN architecture and limits early adaptive responses

We next considered how DC-mediated recruitment of innate effector cells would influence adaptive responses within the draining LNs. Strikingly, upon inspection of the sites associated with adaptive immunity, we found that in regions heavily infiltrated by innate cells, and in particular neutrophils, the T cell zone appeared less densely packed with T cells as compared with the contralateral, less inflamed side of the LN (Figure 6A). Complete absence of B cell follicles was also frequently observed in these neutrophil-rich zones. Quantification of T and B cell polarity showed lower densities of these cells in inflamed areas relative to the opposite side of the tissue (Figure 6B). Concurrent visualization of other markers of tissue structure further revealed that high neutrophil influx was associated with disruption of HEVs, as characterized by reduced MECA79, collagen IV, and CCL21 staining (Figures S6A–S6C). Depletion of neutrophils using anti-Ly6G antibody resulted in a uniform distribution of T cells across the tissue (Figure 6B), increased B cell cellularity in the inflamed regions (Figure 6B), and restoration of HEV integrity (Figures S6A and S6D). However, this came at the cost of increased bacterial spread within the draining LNs and spleen (Figures 6A, 6C, and 6D). These data suggest that while neutrophils are critical for local pathogen containment, they also disrupt normal LN architecture, including sites typically dedicated to the generation of adaptive immunity.

Given that DCs regulate innate cell recruitment across the LN parenchyma and into the T cell zone, we next asked whether disruption of the adaptive compartments originated from DCs. To test this, we examined LNs from *P. aeruginosa*-infected Zbtb46-DTR chimeras. We found that polarized dispersal of lymphocytes was less evident after DC depletion (Figure S6E). Instead, we observed smaller pockets devoid of T or B cells, which correlated with the location of neutrophil micro-swarms. We also inspected LNs from CpG-immunized Zbtb46-DTR chimeras, with or

without DC ablation. Similar to infection settings, we found that T cells were more dispersed in areas of high innate effector cell influx (Figure 6E and 6F). Importantly, depletion of DCs normalized both CD4 and CD8 T cell densities across the LNs. Thus, these data indicate that disruption of the T cell zone is indeed DC-mediated.

These findings were counterintuitive, as they suggested that by promoting large-scale innate cell trafficking into LNs, DCs might potentially hinder the ability of naïve T cells to survey these inflamed regions to find their cognate antigens. To probe this idea, we adoptively transferred naïve, OVA-specific OT-I CD8 T cells into mice and then infected the mice with *P. aeruginosa* co-administered with OVA antigen. Draining LNs were collected 12 hours later to visualize early T cell priming by microscopy, and the spatial relationship between neutrophils and antigen-specific T cells was quantified using CytoMAP (Figure S6F). Positional data on cell populations were raster-scanned into 50 μm radius neighborhoods, which were then clustered into regions based on cell type composition. This yielded six distinct regions, of which regions 4 to 6 demarcated the T cell zone, as indicated by the high abundance of CD8 T cells (Figures 6G and S6G). Region 6 specifically identified areas of the T cell zone which were heavily infiltrated by neutrophils, and these neighborhoods were polarized to one side of the LN. Notably, CD8 T cells were found in lower abundance within this region, while the antigen-specific OT-I CD8 T cells were almost completely excluded. In contrast, OT-I T cells were selectively enriched in region 4, and these neighborhoods were primarily localized on the less inflamed side of the LN. Analysis of cell-cell spatial correlations across the tissue indicated that neutrophils were negatively correlated with both OT-I and total CD8 T cells (Figure 6H). Quantification of OT-I T cell polarity confirmed a lower density of OT-I cells on the neutrophil-rich, inflamed side relative to the contralateral side (Figure 6I). Depletion of neutrophils with anti-Ly6G antibody led to a more dispersed distribution

of T cell priming regions across the LN (Figure 6G), and OT-I T cells now displayed a trend towards preferential localization in the inflamed side (Figure 6I). Further assessment by flow cytometry showed no change in the total number of antigen-specific OT-I cells or endogenous lymphocytes (Figures 6J and S6H), suggesting that neutrophils spatially displace lymphocytes away from the site of inflammation, even if it contains more antigen[221]. Importantly, depletion of neutrophils resulted in significantly increased T cell activation, as indicated by higher pS6 expression in OT-I T cells and greater abundance of pS6-high cells (Figure 6J). No major differences in DC cellularity or resident DC maturation were observed (Figure S6I). Together, these data show that extensive neutrophil infiltration limits the available areas within the draining LN for T cell priming, which in turn leads to diminished early T cell activation.

We next tested the role of DC-recruited neutrophils in a vaccination model. Mice were immunized with OVA plus CpG, with or without anti-Ly6G antibody treatment. Endogenous OVA-specific CD8 T cell responses were examined in draining LNs 4 days later by flow cytometry using Kb-SIINFEKL tetramers. We found that neutrophil depletion resulted in enhanced abundance of tetramer-binding CD8 T cells (Figure 6K), indicating that infiltrating neutrophils limit adaptive responses within the LN. We also noted a trending decrease in tetramer MFI, suggesting that neutrophils preferentially disrupt low affinity T cell responses (Figure S6J). No alterations in Ki67 expression or effector differentiation were seen with neutrophil depletion. Collectively, these data demonstrate that while neutrophil recruitment is critical for innate defense, extensive neutrophil influx compromises the LN's capacity to support maximal adaptive responses, and this paradoxically stems from the actions of DCs.

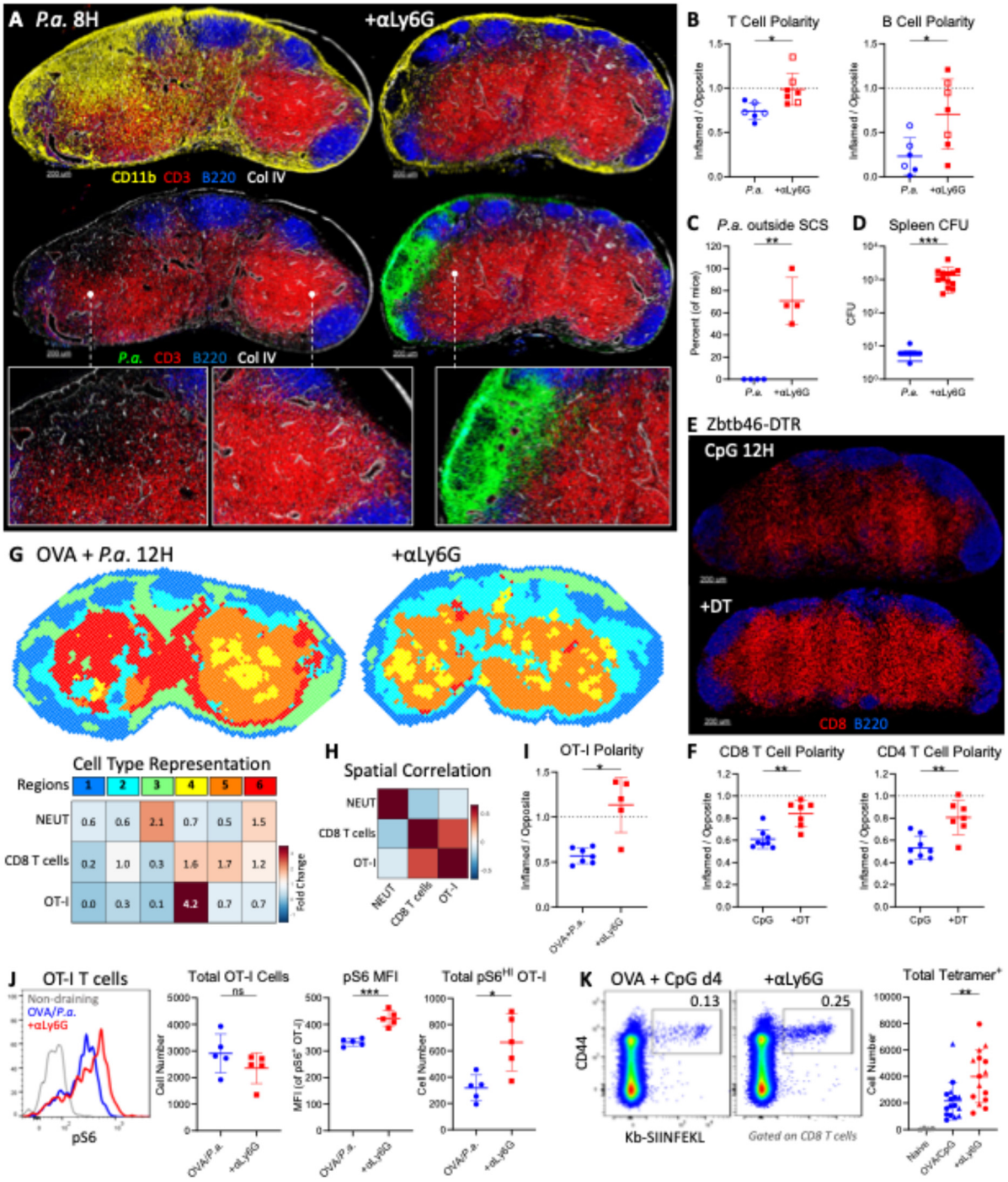

Figure 6: DC-mediated recruitment of innate effector cells disrupts the T cell zone and limits early T cell responses.

(A to D) B6 mice were infected with GFP expressing *P. aeruginosa* (*P.a.*), with or without anti-Ly6G treatment 24 hours prior. (A to C) Draining LNs were assessed by microscopy 8 hours post-infection. (A) Representative images showing the T cell zone, B cell follicles, and *P. aeruginosa* relative to CD11b^{+} innate cell influx. Collagen IV (Col IV) labels stroma. (B) Histo-cytometry quantification of T and B cell polarity across the tissue. Data are pooled from two experiments, indicated by different symbols. (C) Percent of mice displaying *P. aeruginosa* outside of the LN macrophage layer. Each point denotes a separate

experiment. (D) Total CFU in the spleen 12 hours after infection. Data are pooled from multiple experiments. (E and F) Zbtb46-DTR chimeras were immunized with CpG, with or without DT injection, and the T cell zone was visualized 12 hours later. (E) Representative images and (F) quantification of T cell polarity within draining LNs via histo-cytometry. (G to J) B6 mice were transferred naïve OT-I T cells, and some mice were given anti-Ly6G. 24 hours later, mice were infected with *P. aeruginosa* co-administered with OVA. Draining LNs were assessed by (G to I) imaging or (J) flow cytometry 12 hours later. (G) Positional data on neutrophils and T cells was clustered into regions based on cell composition. Distribution of identified regions across representative LNs (left). Cell type representation within each region, shown as fold change over the average across all regions (right). (H) Spatial correlation analysis for cell pairs across the LN. (I) Quantification of OT-I T cell polarity, with or without anti-Ly6G treatment. (J) Representative histogram and quantification of OT-I T cell cellularity and pS6 expression. (K) B6 mice were immunized with OVA plus CpG, with or without anti-Ly6G treatment. Representative flow plots and quantification of $CD44^+$ Kb-$SIINFEKL^+$ CD8 T cells in draining LNs, measured by flow cytometry 4 days after immunization. Data are pooled from two experiments, denoted by different symbols. Graphs in (B), (C), (F), (I), (J), and (K) show mean ± SD and were analyzed using unpaired *t* test with Welch's correction. In (D), median is shown, and data was analyzed using Mann-Whitney test. *** $P \leq 0.001$; ** $P \leq 0.01$; * $P \leq 0.05$; not significant (ns) $P > 0.05$. Data in (A) and (E to K) are representative of at least two independent experiments.

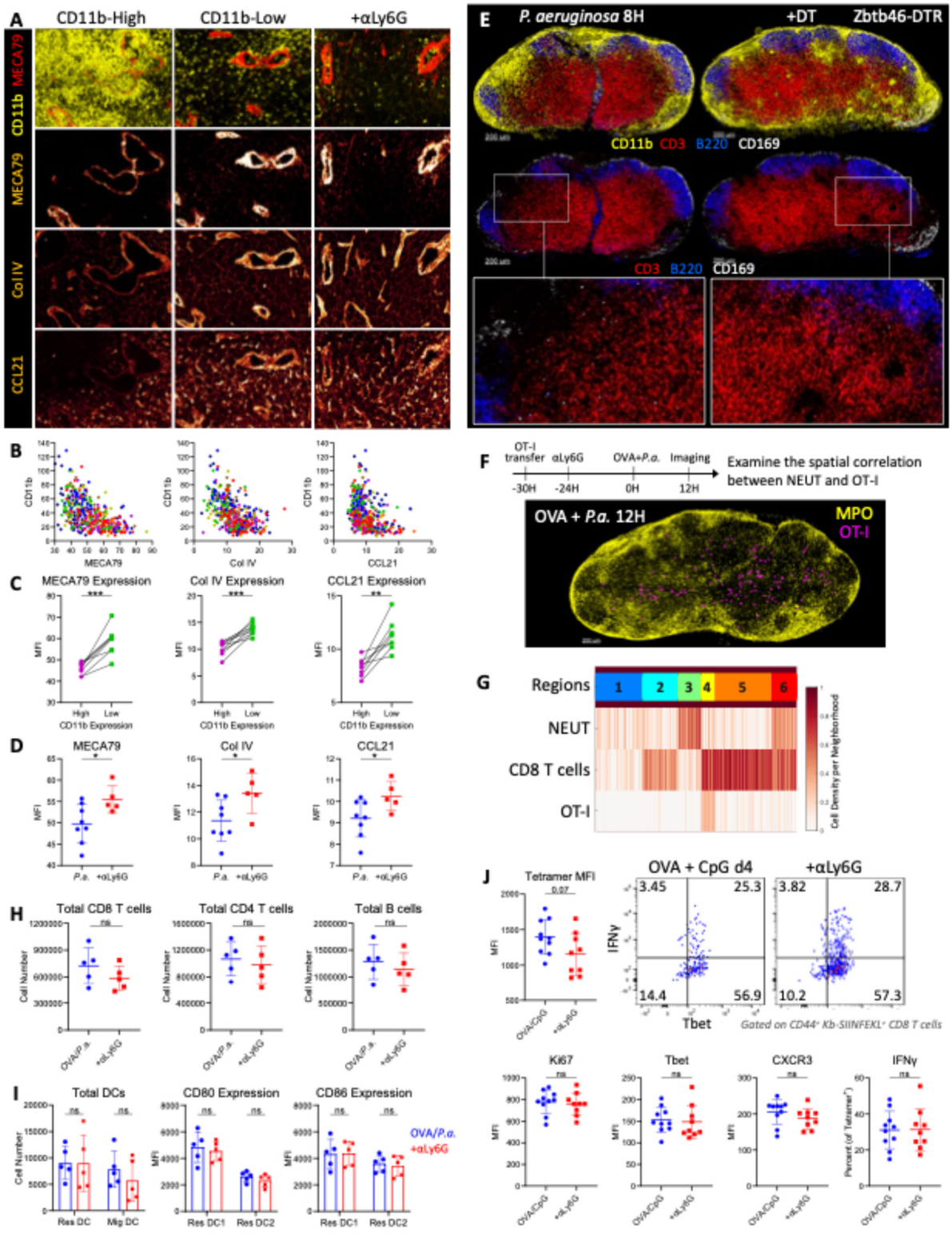

Figure S6: Large-scale neutrophil infiltration disrupts normal LN architecture.
(A to D) B6 mice were infected with GFP expressing *P. aeruginosa* (*P.a.*), with or without anti-Ly6G treatment. HEVs in draining LNs were assessed by microscopy 12 hours later. (A) Insets show representative look-up table (LUT) images of MECA79, collagen IV (Col IV), and CCL21 expression on

HEVs in CD11b-high, neutrophil-rich (left panels) versus CD11b-low, neutrophil-devoid regions (middle panels), as well as following neutrophil depletion (right panels). (B) Correlation plots of CD11b (neutrophil abundance) versus MECA79, collagen IV, or CCL21 fluorescence intensity on HEV surface objects. Each color denotes HEV surfaces from separate LNs. (C) HEV surfaces were grouped based on CD11b expression. MECA79, collagen IV, and CCL21 expression on CD11b-high versus CD11b-low HEV surfaces was quantified. (D) MECA79, collagen IV, and CCL21 MFI on HEV surfaces, with or without anti-Ly6G treatment. (E) Zbtb46-DTR chimeras were infected with *P. aeruginosa*, with or without DT injection, and the T cell zone was visualized 8 hours later. (F and G) Supplemental data for Figures 6G to 6I. (F) Experimental design and representative draining LN showing antigen-specific OT-I T cells in relation to MPO^+ neutrophils 12 hours after infection with *P. aeruginosa* co-administered with OVA. (G) Heatmap showing the cellular composition for each region type. Each column represents a spatial neighborhood, clustered into regions. (H and I) Supplemental data for Figure 6J. Mice were transferred OT-I cells and then infected with OVA plus *P. aeruginosa*, with or without anti-Ly6G treatment. Draining LNs were assessed via flow cytometry 12 hours later. (H) Total numbers of endogenous T and B cells as well as (I) DC cellularity and CD80 and CD86 expression by resident DCs. (J) Supplemental data for Figure 6K. $CD44^+$ Kb-SIINFEKL$^+$ CD8 T cells in draining LNs were examined by flow cytometry 4 days after OVA plus CpG immunization, with or without anti-Ly6G treatment. Quantification of Kb-SIINFEKL MFI, as well as expression of the indicated markers and IFNγ production following ex vivo restimulation. In (C), linked points indicate data from the same LNs and was analyzed via paired *t* test. Graphs in (D), (H), (I), and (J) show mean ± SD and were analyzed using unpaired *t* test with Welch's correction. *** $P \leq 0.001$; ** $P \leq 0.01$; * $P \leq 0.05$; not significant (ns) $P > 0.05$. All data are representative of at least two independent experiments.

DCs and DC-recruited monocytes clear dying neutrophils to restore LN architecture

Given that the generation of adaptive responses is a critical function of the LN, we reasoned that there must also be mechanisms in place to help restore normal LN architecture upon threat cessation. In this regard, we found that while the numbers of monocytes and NK cells within inflamed LNs were sustained over time, neutrophil cellularity rapidly declined by 24 to 36 hours (Figures 7A, 7B, and S7A). This was accompanied by the restoration of the T cell zone, as shown by the equilibration of T cell density across inflamed versus less-inflamed parts of the tissue (Figures 7B, 7C, and S7B). Annexin V staining showed that after infiltrating the LNs, many neutrophils underwent apoptosis (Figure S7C). Imaging of neutrophils via MPO staining further revealed that at later time points, much of the MPO signal appeared highly punctate, and was localized within CD11c-expressing DCs as well as CD64-expressing monocytes (Figures 7D and S7D), suggesting that the dying neutrophils were actively being cleared by these cell populations. To test this, LN suspensions were stained with both surface-bound and intracellular Ly6G

conjugated to different fluorophores and analyzed by flow cytometry to detect myeloid cells which have phagocytosed neutrophils (surface-Ly6G^{-}, ICS-Ly6G^{+})[235]. Indeed, we found a large amount of DCs and monocytes that were positive for intracellular Ly6G (Figures 7E and S7E), with monocytes being numerically dominant and the overall kinetics mirroring that of neutrophil clearance (Figures 7A and S7A). Finally, CD11c-expressing cells phagocytosing neutrophils within immunized LNs could be observed directly in situ using intravital two-photon microscopy (Movie S4). Altogether, these findings demonstrate that dying neutrophils are cleared by DCs and DC-recruited monocytes, and this is followed by restoration of the T cell zone and LN architecture.

Notably, while the neutrophils were cleared from inflamed LNs, the polarized distribution of monocytes remained (Figures 7B, bottom, and 7C). Consistent with past observations, this resulted in the generation of distinct innate cell microenvironments across the tissue, characterized by differential abundance of monocytes versus DCs[28]. Furthermore, activated T cells were now found abundantly dispersed throughout the T cell zone, with those on the inflamed side encountering a higher concentration of monocytes, and those on the contralateral side exposed to more DCs (Figure 7B, zoom-ins). These two innate cell types provide non-redundant signals to T cells during priming[28,93,94], and their spatial organization into discrete microdomains within the LN in turn help establish early heterogeneity in T cell differentiation[28]. Therefore, DC-driven recruitment and localization of innate effector cells influences not only the initial inflammatory response but also shapes the quality of subsequent adaptive immunity.

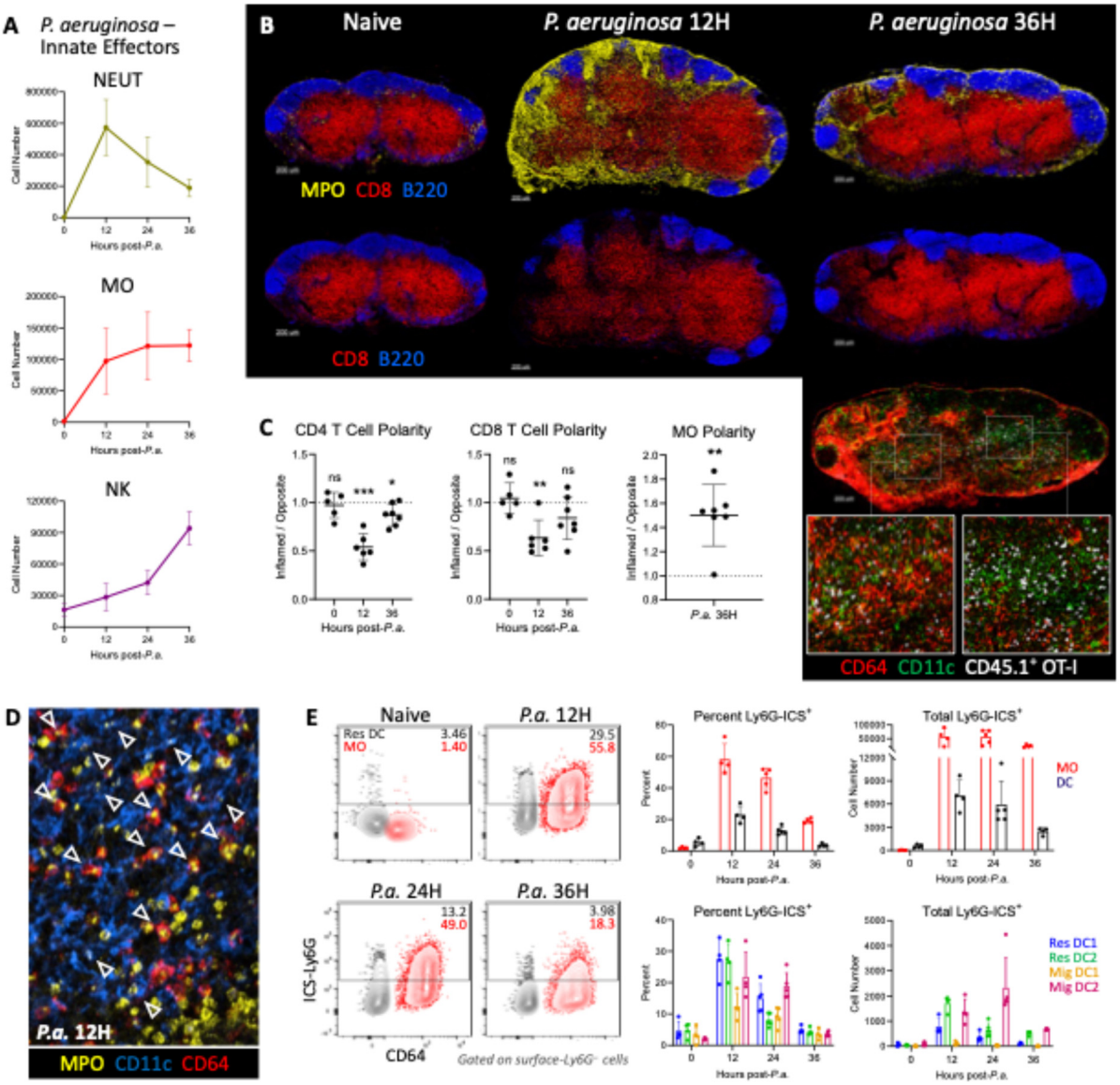

Figure 7: DCs and DC-recruited monocytes phagocytose neutrophils to restore the T cell zone.
B6 mice were infected with GFP expressing *P. aeruginosa* (*P.a.*) and draining LNs were evaluated at multiple time points. In (B and C), mice were also transferred naïve OT-I T cells one day prior to infection, and OVA was co-administered with *P. aeruginosa*. (A) Total numbers of the specified cell types, as measured by flow cytometry. (B) Representative images of T and B cell zones with respect to MPO^+ cell abundance over time (top panels). Localization of $CD64^+$ monocytes, $CD11c^+$ DCs, and $CD45.1^+$ antigen-specific OT-I T cells at 36 hours is also shown (bottom panel and zoom-ins). (C) Quantification of CD4 T cell, CD8 T cell, and monocyte polarity across the tissue at the indicated time points. (D) Draining LNs visualized by microscopy 12 hours after infection. Arrows point to examples of $CD11c^+$ DCs and $CD64^+$ monocytes with detectable intracellular MPO signal. (E) *P. aeruginosa*-infected LNs stained with both surface-bound and intracellular Ly6G conjugated to different fluorophores, analyzed by flow cytometry. Myeloid cells which have phagocytosed neutrophils (surface-$Ly6G^-$, ICS-$Ly6G^+$) were quantified. All graphs show mean ± SD. Data in (C) was analyzed with one-sample *t* test with a hypothetical value of 1.0. *** $P \leq 0.001$; ** $P \leq 0.01$; * $P \leq 0.05$; not significant (ns) $P > 0.05$. All data are representative of at least two independent experiments.

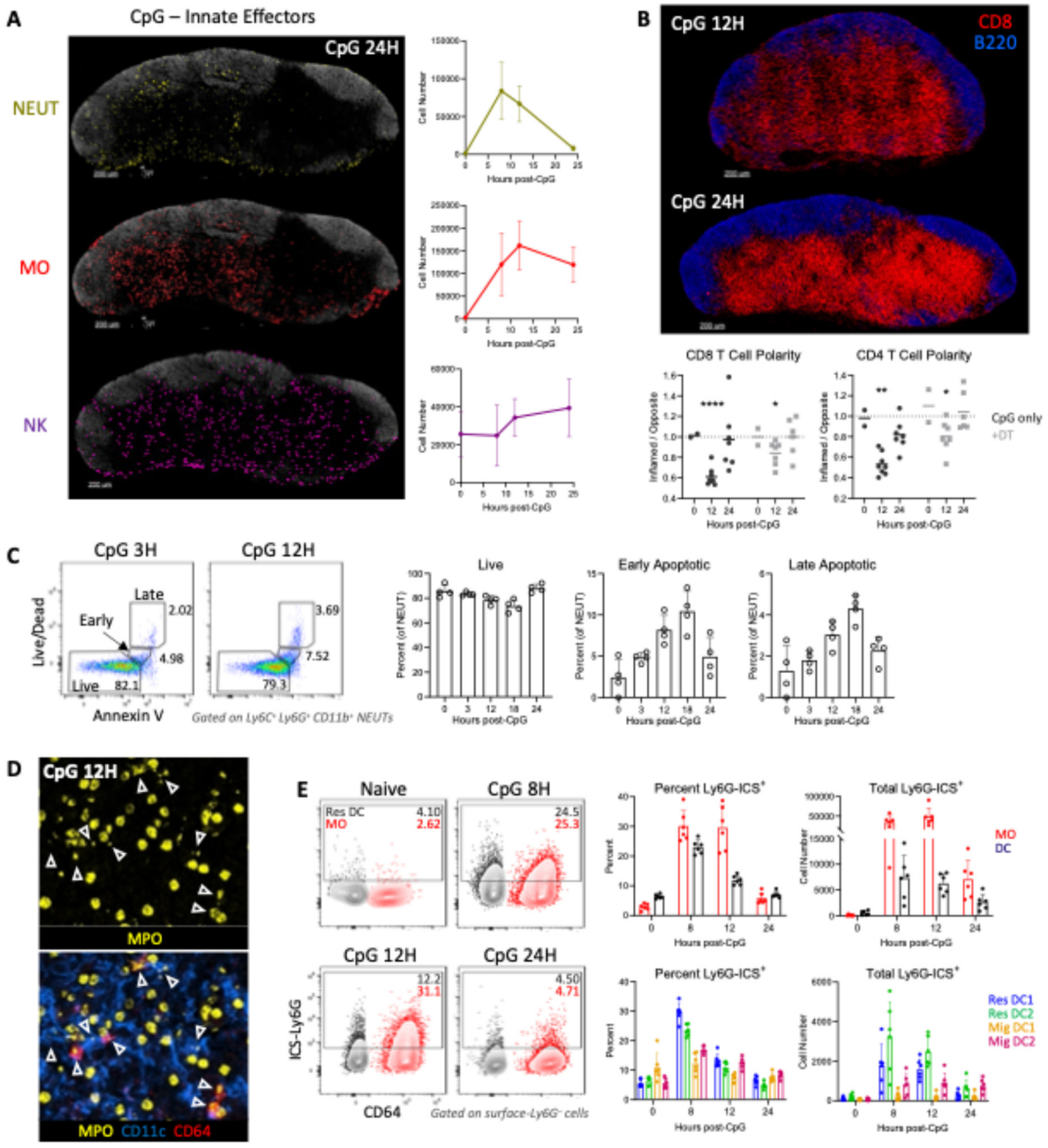

Figure S7: Neutrophils are cleared from LNs over time by DCs and monocytes.
(A) Neutrophil, monocyte, and NK cell density and cellularity in draining LNs were evaluated by imaging (Zbtb46-DTR chimeras, no DT treatment) and flow cytometry (B6 mice) following CpG immunization at the indicated time points. (B) Zbtb46-DTR chimeras were immunized with CpG and draining LNs were collected for microscopy. Representative images of the T cell zone at early versus late time points (top). Analysis of CD4 and CD8 T cell polarity across the draining LNs over time (bottom). Extended dataset for Figure 6F. (C) B6 mice were immunized with CpG, and neutrophils were assessed for Annexin V and Live/Dead expression via flow cytometry at the specified time points. (D) Draining LNs from CpG-immunized mice were visualized by microscopy at 12 hours. Arrows point to examples of $CD11c^+$ DCs and $CD64^+$ monocytes with detectable intracellular MPO signal. (E) CpG-immunized LNs stained with both surface-bound and intracellular Ly6G conjugated to different fluorophores, analyzed by flow

cytometry. Myeloid cells which have phagocytosed neutrophils (surface-Ly6G$^-$, ICS-Ly6G$^+$) were quantified. Graphs show either mean or mean ± SD. Data in (B) was analyzed with one-sample *t* test with a hypothetical value of 1.0. **** $P \leq 0.0001$; ** $P \leq 0.01$; * $P \leq 0.05$. All data are representative of at least two independent experiments.

4.3 Discussion

It has long been recognized that DCs represent an integral bridge between the innate and adaptive arms of the immune system. They serve as chief sentinel cells which integrate information about the state of peripheral tissues and present antigens to T cells to promote either immune tolerance or initiation of adaptive responses[36]. We now report that the functional repertoire of DCs extends beyond these classical functions. By regulating the recruitment and organization of innate cells within the LNs during inflammation, DCs first tune the organ towards a pro-innate state to help prevent pathogen dissemination and then re-establish normal tissue architecture for optimal generation of adaptive immunity. Thus, DCs orchestrate a delicate balance between the organ's innate and adaptive functions, which are temporally synchronized and calibrated to the organism's need for effective host defense.

Upon pathogen breach of the skin barrier, immune cells within the LN must quickly work together to contain lymph-borne pathogens and block access to the systemic circulation, while also initiating the generation of adaptive responses for long-term protective immunity. Effective execution of these functions is achieved by several concomitant and highly coordinated processes[15,221]. Macrophages lining the subcapsular sinuses sequester incoming pathogens to limit systemic spread as well as shuttle these antigens to B cells to promote humoral immunity. Strategically prepositioned or recruited innate effector cells further fortify local innate defense. Simultaneously, LN resident-DCs residing near the lymphatic sinuses capture draining antigens, undergo maturation, and reposition into the T cell zone, where they initiate T cell responses.

We now uncover that en route to the T cell zone, activated DCs migrate through the HEV-dense interfollicular zones, concurrently producing multiple inflammatory chemokines as well as expressing high levels of the integrin ligand, ICAM-1. This generates a rich haptotactic scaffold that facilitates efficient HEV-mediated entry and intranodal migration of multiple innate effector cells, including neutrophils, monocytes, and NK cells. Recruitment of innate effector cells is highly polarized across the LN, mirroring the drainage of pathogens and inflammatory signals. Thus, DCs provide the pathways for innate cells to rapidly migrate toward the sites of pathogen invasion to perform their effector functions, while also setting up inflammatory gradients across the tissue. Although these processes are necessary for effective innate defense, if excessive, they can interfere with the LN's ability to generate early adaptive responses. During bacterial infection, large-scale infiltration of neutrophils results in substantial disruption of normal LN architecture, including alterations to local blood vessels as well as displacement of the T cell zone and B cell follicles. This relegates early priming of naïve T cells to regions distal to the sites of high neutrophil influx, thereby limiting the potential magnitude of T cell immunity. Importantly though, the DCs also provide the mechanism to resolve this issue as the demand for innate defense diminishes over time. Upon threat cessation, DCs and DC-recruited monocytes phagocytose the infiltrating neutrophils, clearing them from the LN parenchyma. This leads to the restoration of the T cell zone and allows for more optimal adaptive responses to ensue.

In this regard, we have previously shown that polarization of LNs based on innate cell composition plays important roles in local programing of T cell responses[28]. Following DC-dependent entry, recruited monocytes undergo maturation, produce copious amounts of IL-12, and functionally cooperate with the antigen-presenting DCs to potentiate effector T cell differentiation. In contrast to neutrophils, monocyte gradients are maintained over multiple days, creating discrete

innate cell microenvironments within the LN. This fosters nonuniform T cell differentiation across the tissue, where early effector T cells are primarily generated in microenvironments heavily infiltrated by monocytes, while less differentiated T cells are found in microenvironments with fewer monocytes and a greater abundance of DCs. Additional functional distinctions between DCs and monocytes may further influence these microdomains and the ensuing T cell response[266-269], whose differentiation can be reinforced by subsequent migration into highly inflamed regions of the LN[162,186,187,270,271]. These studies highlight that DCs and monocytes extensively cooperate to shape the local innate cell landscapes that modulate the quality and heterogeneity of T cell responses.

Past studies have identified that the subcapsular sinus is a critical niche where multiple immune cell types coalesce to prevent pathogen dissemination[19,21,180,272,273]. Our findings now reveal that innate defense is not restricted to the outer periphery but instead can extend into the deeper parenchymal regions of the LN. Moreover, DCs direct the generation of these additional layers of defense. Much like subcapsular sinus macrophages, LN-resident DCs localize near the lymphatic sinuses at steady state and efficiently detect lymph-borne pathogens and inflammatory agents. However, in contrast to the macrophages, which respond to these signals by locally activating and recruiting cells, DCs integrate this information and migrate into the T cell zone, propagating innate responses across the tissue. Given the numerical dominance of macrophages in the sinuses and that of DCs within the deep parenchyma of the organ, it stands to reason that the cooperative action of both cell types ensures optimal generation of innate defense within the draining LNs.

We also find non-identical roles for DC subsets in regulating innate cell trafficking. Removal of the immunization site did not significantly affect the total numbers of innate effector

cells in draining LNs, indicating that the influx of migratory DCs is not required for innate cell recruitment. Furthermore, in DC-CCR7.KO chimeras, where migratory DCs are absent, innate cell trafficking is not reduced but mislocalized, mirroring the altered distribution of resident DCs within the tissue. Consistent with this, the spatial dispersal and timing of innate cell infiltration appear highly concordant with that of resident DC activation and repositioning, which also occur prior to a significant influx of migratory DCs. Together, these findings suggest that innate cell recruitment and positioning is largely driven by the actions of LN-resident DCs. This reinforces the notion that while migratory DCs effectively surveil peripheral tissues, resident DCs are poised to scan lymphatic fluids and elicit rapid responses within LNs for immediate host defense in settings of pathogen dissemination or vaccine drainage[27]. Nevertheless, we do not exclude the possibility of migratory DC involvement. Migratory DCs are present within LNs even at homeostasis, and express high levels of ICAM-1. Of relevance, migratory DC2s have been shown to localize near HEVs and in the interfollicular zones at both steady state and during inflammation[26,29,65,143,274-276]. Therefore, resident and migratory DCs likely intermix during inflammation, together forming dense cellular networks that support innate cell trafficking across the parenchyma. It should be noted that our studies focus on immune responses occurring within draining LNs during the initial 24 hours of inflammation. Late-arriving migratory DCs may influence subsequent innate responses, such as by guiding tissue-derived monocytes into downstream LNs via the lymphatics[260]. DCs have also been reported to promote innate effector cell recruitment to the sites of infection and antigen deposition in peripheral tissues and spleen[257,277,278]. This posits that DCs function as critical regulators of innate cell activity across multiple organs and stages of the immune response.

We further examine the respective contributions of DC1 versus DC2 populations and find that DC2s play a preferential role in promoting innate cell recruitment into the T cell zone. Divergent chemokine and ICAM-1 expression were observed between the subsets, although this did not yield an obvious explanation for the DC2 bias in this process, indicating that additional factors are involved. Localization differences may explain some of the disparities in their functions. At steady state, resident DC2s are enriched near lymphatic sinuses while resident DC1s instead position in proximity to blood vessels within the paracortex[26,27,29,222]. Consequently, during drainage of inflammatory agonists or microbes, it is predominantly the resident DC2s which migrate from the lymphatic sinuses, through the HEV-rich interfollicular zones, and into the T cell zone. In contrast, resident DC1s rapidly detach from the HEVs and enter the deep T cell zone at earlier time points. Therefore, in addition to functional specializations, spatiotemporal differences in DC migration, and how these intersect with the kinetics of innate cell recruitment, likely dictate the relative contributions of individual DC populations in regulating innate cell trafficking.

It has been previously documented that DCs can instruct T cell priming through expression of chemokines and adhesion molecules[162,196,197,271,276,279-283]. Our studies now indicate that through similar mechanisms, DCs also direct the recruitment and localization of multiple innate effector cells across the LN, thereby regulating both the innate and adaptive arms of the immune response. Of note, while our results clearly demonstrate that DC depletion leads to diminished innate responses, some of these effects may be indirectly mediated. Various forms of crosstalk among the involved cell populations have been described in other inflammatory contexts[156,188,191,192,194,257,284,285], and it is possible that DCs are upstream of a cascade of feed-forward innate cell activity and interactions[286]. For instance, DCs may provide an initial source of chemokines, while recruited cells subsequently amplify the chemotactic gradient, reinforcing

polarity across the lymph node. Additionally, innate effector cells may produce inflammatory cytokines that further enhance DC maturation. Moreover, DCs closely interact with the underlying stroma and blood endothelial cells, and this could provide additional means to modulate cellular trafficking. For example, DCs have been shown to control fibroblastic reticular cell contractility and survival as well as the phenotype of HEVs, and this can in turn influence lymphocyte influx and retention[33,82-85,254,255,287]. Alternatively, DCs may locally shape the chemokines expressed by blood endothelial cells, such as via IL-1β secretion.

A key finding in our work is that during infection or vaccination, the LN undergoes significant reorganization due to large-scale infiltration of innate cells into the T cell zone and B cell follicles. This is surprising given that the T cell zone is often characterized as a more pristine region, sheltered away from the innate cell battleground, and dedicated to the initiation of adaptive immunity. In fact, we find that extensive neutrophil recruitment can actively disrupt normal LN architecture. This includes changes to HEV integrity, altered patterns of lymphocyte trafficking, ablation of B cell follicles, as well as dispersal of the T cell zone. Functionally, such robust neutrophil influx appears to confine early T cell activation to less inflamed areas of the paracortex, limiting the overall magnitude of T cell responses. Consistent with these findings, it has previously been reported that in addition to causing general pathology within peripheral tissues[182,219,288-291], neutrophil trafficking to LNs can dampen CD4 T cell and B cell adaptive responses in immunization settings[224,226,227,232]. Along similar lines, it has been shown that monocytes can infiltrate B cell follicles and suppress humoral immunity[229,230,234], while NK cell relocalization into the splenic white pulp can impair both arms of the adaptive immune response[223,225,228,233]. Furthermore, major disruption of lymphoid tissues attributed to excessive innate cell recruitment has been noted in chronic infection settings, and this markedly reduced the ability of the organ to

generate functional adaptive responses[231,292,293]. Curiously, we also find induction of iNOS expression across the LN parenchyma, a molecule known not only for its antimicrobial functions but for its potent capacity to suppress T and B cell responses[229,231,294-298]. Together, this raises important considerations for rational vaccine design. It suggests that while innate cell activation and recruitment are essential for productive generation of adaptive responses, excessive or prolonged inflammation could be detrimental.

Notably, neutrophil, monocyte, and NK cell recruitment, as well as iNOS induction, are all at least in part downstream of DC-mediated activity. This suggests that the role of DCs in promoting innate defense is complex and can come at a significant cost to adaptive responses. This notion contradicts our general understanding of DC biology in settings of inflammation, in which they typically play positive roles in the generation of adaptive immunity. Importantly, we find that following the initial disruption of LN architecture, DCs over time help restore the tissues. Neutrophils undergo cell death after delivering their effector functions, and it is the DCs and DC-recruited monocytes which phagocytose these dying cells to clear the T cell zone and B cell follicles. In other work, DCs have also been shown to support vascular growth and re-establishment of quiescence[84,254,255]. Thus, these findings demonstrate that DCs as a population are highly dynamic and adapt their functions during distinct stages of inflammation.

Collectively, our studies propose that during pathogen invasion, the LN faces a tradeoff between the need for immediate innate defense against rapidly disseminating pathogens and the generation of maximal adaptive responses for long-term sterilizing immunity. This balance appears to be actively managed by DCs, which serve as a rheostat to regulate these two critical functions of the organ in a timely fashion. Our findings underscore that the capabilities of DCs surpass their originally described roles as antigen-presenting cells. By regulating cellular

organization across the tissue, promoting large-scale innate defense within the LNs, and driving T cell adaptive responses, DCs coordinate the dual evolutionary functions of the LN, and orchestrate a unified response that is tailored to the organism's short- and long-term needs for effective host defense.

4.4 Limitations of the study

Although we showed that DCs increase their expression of multiple chemokines and the adhesion molecule ICAM-1 during inflammation, they may also regulate innate cell trafficking via other direct and indirect mechanisms. Furthermore, this could vary based on specific models of infection or inflammation, with altered kinetics of drainage and modes of signaling. In addition, while our work identified that innate effector cells predominantly enter draining LNs via HEVs, cells arriving from afferent lymphatics also contribute. These lymph-derived cells may rely on distinct molecular mechanisms and could uniquely influence the immune response[6,96,235,260]. Finally, CD11c-YFP reporter mice used in two-photon intravital microscopy studies do not allow resolution of the diverse CD11c-expressing populations, and additional reporter strains will be necessary to resolve the complexity of myeloid cell types involved[299].

4.5 Materials and methods

Mice:

CD11c-YFP mice were crossed to Actin-DsRed mice to make CD11c-YFP Actin-DsRed dual reporter mice. CD11c-YFP mice were crossed with B6 albino mice to homozygosity and next crossed to CCR2-RFP mice to generate CD11c-YFP CCR2-RFP heterozygous dual reporter mice. CD11c-Cre mice were crossed to $IRF4^{fl/fl}$ mice to generate CD11c-Cre $IRF4^{fl/fl}$ mice. All mice were maintained in specific pathogen-free conditions at an Association for Assessment and

Accreditation of Laboratory Animal Care-accredited facility at the University of Washington, South Lake Union campus. All procedures were approved by the University of Washington Institutional Animal Care and Use Committee.

Bone marrow chimeras:

C57BL/6 mice were exposed twice to 500 rad of X-ray irradiation separated by a 3 hour rest period and then intravenously injected with 1 to 2 million donor bone marrow cells the same day. Mice were kept on Baytril for 2 weeks after that and allowed to reconstitute for at least 6 weeks before experimentation. For Zbtb46-DTR bone marrow chimeras, irradiated recipients were reconstituted with zDC-DTR bone marrow. For DC-CCR7 bone marrow chimeras, irradiated recipients were reconstituted with a 50:50 mix of Zbtb46-DTR and CCR7.KO or C57BL/6 bone marrow. For DC-ICAM-1 bone marrow chimeras, irradiated recipients were reconstituted with a 50:50 mix of Zbtb46-DTR and ICAM-1.KO or C57BL/6 bone marrow. Diphtheria toxin (DT) was intraperitoneally administered in phosphate-buffered saline (PBS) at 20 ng/g bodyweight.

Immunizations and infections:

All immunizations and infections were administered intradermally into the ear pinnae and/or into the front footpads (auricular or brachial draining LNs, respectively). For CpG immunizations, 20 μg of CpG ODN 1668 (AdipoGen) was mixed with PBS to a 20 μl final volume. For heat-killed *Escherichia coli* inoculations, ~ 2.4 x 10^7 heat-killed *E. coli* BioParticles (Thermo Fisher Scientific) was prepared in 20 μl PBS. For *Pseudomonas aeruginosa* infection, GFP-expressing *P. aeruginosa* PAO1 (kindly provided by Matthew Parsek, University of Washington) was grown in 10 mL LB medium at 37°C until OD_{600nm} 0.6 to 0.7. 10^7 colony-forming units (CFU) of bacteria were then diluted in 30 μl PBS. To measure bacterial loads, LN and spleen homogenates were prepared and then plated on LB agar plates. Plates were incubated at 37°C for 16 to 24 hours

and then colonies were enumerated. For OVA immunizations, 1 μg endotoxin-free OVA (Invivogen) plus 20 μg CpG, or 10 μg OVA and 10^7 CFU *P. aeruginosa* were used.

In vivo treatments:

In some experiments, SIVS[236,237] was performed by intravenously injecting 3 μg of fluorescent anti-CD45.2 antibody (clone 104; BioLegend; APC, BV421, or PE conjugate). Intravascular labeling of DCs[241,242] was done by intravenously injecting 3 μg of fluorescent anti-CD11c antibody (clone HL3; BD Pharmingen; PE conjugate) 30 minutes prior to tissue harvest. For the site removal study, the immunized ear pinnae was surgically removed 2 hours post-immunization. In some animals, 100 μg anti-CD62L (clone Mel-14; BioXCell) was administered intraperitoneally 2 hours before immunization. For the bone marrow transfer study, $CD45.1^+$ bone marrow was isolated from naïve mice and $1.5x10^7$ cells were intravenously transferred into CpG-immunized $CD45.2^+$ Zbtb46-DTR chimeras. For adoptive transfers, naïve $CD45.1^+$ OT-I T cells were isolated from LNs and spleens using the naïve $CD8^+$ T cell isolation kit (Miltenyi Biotec). $1.2–1.5x10^6$ (imaging) or $7.5x10^4$ (flow cytometry) then transferred into $CD45.2^+$ C57BL/6 hosts intravenously. For neutrophil depletion, 500 μg of anti-Ly6G (clone 1A8; BioXcell) was injected intraperitoneally 24 hours prior to immunization or infection.

Confocal and two-photon intravital microscopy:

For confocal imaging, isolated LNs were fixed using BD Cytofix (BD Biosciences) diluted 1:2 with PBS for 8 to 24 hours at 4°C and then dehydrated with 30% sucrose for 12 to 48 hours at 4°C. Tissues were then embedded in OCT compound (Tissue-Tek) and stored at -80°C. LNs were sectioned on a Thermo Scientific Microm HM550 cryostat into 20 μm sections and were then stained as outlined previously[26]. A Leica SP8 tiling confocal microscope equipped with a 40x 1.3NA oil objective was used for confocal image acquisition. For two-photon intravital

microscopy, immunized mice were anesthetized using an isoflourane vaporizer and popliteal LNs were surgically exposed. Imaging was done as before[28] using a Leica SP8 tiling confocal microscope outfitted with a Chameleon laser and a 20x, 1.0 NA water immersion objective. Mice were intravenously administered 300 μg Dextran (70,000 molecular weight; FITC conjugate) and, in some experiments, 3 μg anti-Ly6G antibody (PE conjugate), 1 to 2 hours prior to imaging. All acquired raw imaging data was processed and analyzed in Imaris (Bitplane).

Image analysis:

Histo-cytometry analysis was performed as previously described[26,28]. In brief, multiparameter confocal images were corrected for fluorophore spillover using the built-in Leica Channel Dye Separation module. All images were visualized and analyzed in Imaris. Cell objects were created separately on neutrophils (MPO^+, CD11b-high), monocytes (CD64-intermediate, $CD169^-$, $CD11b^+$ or $SIRP\alpha^+$), NK cells ($NK1.1^+$), resident DCs (CD11c-high, MHC-II-intermediate, $CD169^-$, $CD64^-$), migratory DCs (MHCII-high, CD11c-low/intermediate, $CD169^-$, $CD64^-$, $B220^-$), subcapsular sinus macrophages ($CD169^+$, CD64-low/negative), medullary macrophages (CD64-high), T cells ($CD3^+$) CD4 T cells ($CD4^+$), CD8 T cells ($CD8^+$), OT-I T cells ($CD45.1^+$), or B cells ($B220^+$) using the surface or spot object creation wizard in Imaris. In some analyses, further subgating on Clec9a and SIRPα / CD11b was used to identify DC1s and DC2s, respectively. For *P. aeruginosa* cell objects, GFP signal was used. HEV objects were generated on MECA79 staining. For the data presented in Figure S6, HEV objects were split using 15 μm seed points to better capture heterogeneity. Borders of the deep T cell zone were manually identified using combined staining for B220 and CD3 to demarcate the boundaries between the B cell follicles and T cell zone, as well as MECA79 to exclude outer paracortical regions densely enriched in HEVs. Localization in the subcapsular sinus was defined as cells ≤ 50 μm to $CD169^+$

CD64-low/intermediate staining, whereas positioning in the medulla was identified as cells ≤ 50 μm to CD64-high signal. Proximity to HEVs was defined as cells ≤ 30 μm to MECA79 surface objects. For analysis in Figure 1D, cells in the T and B cell zones represent all remaining cells that were not at the subcapsular sinus, medulla, or HEVs. Cell densities, distances between objects, localization within the T cell zone, as well as the MFI for markers of interest were all quantified using object statistics in Imaris. Polarity was measured by calculating the ratio of cellular density in inflamed versus uninflamed parts of the LN T cell zone. For some analysis, object statistics were exported into FlowJo software for initial subset gating. The data was then transferred into CytoMAP[29] to measure cellular spatial correlations (Pearson's correlation) across tissue neighborhoods (50 μm radius) as well as to cluster cellular neighborhoods into regions based on cell type representation.

Cell isolation and flow cytometry:

LNs were mechanically disrupted and subjected to enzymatic digestion at 37°C on a shaker for 30 min. For quantification of immune cell trafficking, disrupted tissues were treated with collagenase D (400 U/mL; Roche Applied Science). For DCs, digestion with PBS plus 10% fetal bovine serum (FBS) mixed with DNase I (100 ug/mL; Sigma-Aldrich), Dispase II (800 ug/mL; Sigma-Aldrich), and Collagenase P (200 ug/mL; Sigma-Aldrich)[171,172] was used for improved cell yield. For skin digestion, isolated ear skin was incubated on a shaker at 37°C for 45 min in 0.5 mg/ml Dispase II in HBSS and 10% complete RPMI media. Dermal layers were separated, cut, and digested for another 45 min using 1mg/ml Collagenase D and 0.05 mg/ml DNAse I (37°C / 45 min). For flow analysis of T cell responses using Kb/SIINFEKL tetramers (stained on ice 1:50) or of bone marrow cells, enzymatic digestion was not used. To examine chemokine production by DCs, naïve and draining LNs 4 hours post-CpG immunization were isolated and then incubated in

complete RPMI containing GolgiStop (1 ug/mL) at 37°C for 4 hours prior to digestion. For analysis of T cell cytokine production, cells were restimulated with PMA (100 ng/mL), ionomycin (1 ug/mL; Sigma-Aldrich), and GolgiStop (1 ug/mL) in complete RPMI for 4 to 5 hours at 37°C. All surface staining was conducted at 4°C for 30 minutes, except for CCR7, which was stained at 37°C for 30 minutes. Intracellular staining was performed at room temperature for 30 minutes after fixation with the FOXP3 Fix/perm kit (Invitrogen). Annexin V labeling was performed based on manufacturer's instructions (Thermo Fisher Scientific). Flow cytometry data was acquired through the University of Washington, Cell Analysis Facility Shared Resource Lab, using the BD LSR II or BD Symphony A3 cytometer (NIH award 1S10OD024979-01A1). Data was analyzed using FlowJo software.

RNA sequencing:

LNs were isolated and extended enzymatic digestion with Collagenase P was performed to ensure the release of cells entrapped in stroma[171,172]. CD11c-IV-positive and -negative DC subsets were sorted from pooled auricular LNs from three individual mice per group. 500 of each DC cell type was sorted using the BD Aria II cell sorter directly into reaction buffer from the SMART-Seq v4 Ultra Low Input RNA Kit for Sequencing (Takara), and reverse transcription was performed followed by PCR amplification to generate full-length amplified cDNA. Libraries were sequenced by the Genomics Core at Benaroya Research Institute. Quality of RNA was determined on the Agilent Tapestation. Sequencing libraries were constructed using the NexteraXT DNA library preparation kit (Illumina) and samples were run on an Illumina NextSeq 2000 to generate paired-end 59-base reads with a depth of 5 million reads per sample. Base calls were processed to FASTQs on BaseSpace (Illumina) and a base call quality-trimming step was applied to remove low confidence base calls from the ends of reads. The FASTQs were aligned to the GRCm38 mouse

reference genome using STAR v.2.4.2a, and gene counts were generated using htseq-count. Gene counts were filtered and normalized from raw counts by Median Ratio Normalization (MRN). Genes upregulated upon CpG-induced inflammation were filtered based on a false discovery rate cutoff ≤ 0.5 and a minimum expression fold change ≥ 2.

Statistics:

Statistical analysis was performed using GraphPad Prism software. The statistical significance of differences in mean values between the two groups was measured by a two-tailed unpaired Student's t test with Welch's correction. Paired t test was performed when comparing responses within the same experimental animal or tissue. For nonparametric data, Mann-Whitney test was used for analysis of statistical significance between the two groups. Data points represent independent LNs, unless otherwise noted. **** $P \leq 0.0001$; *** $P \leq 0.001$; ** $P \leq 0.01$; * $P \leq 0.05$; not significant (ns) $P > 0.05$.

4.6 Acknowledgements

Thank you to Y. Wu for help sorting on DC subsets, preparing the cDNA for RNA sequencing, and assisting with the initial analysis; to G. Verdezoto, J. Chao, J. Leal, and M. Lyons-Cohen for help conducting experiments; to J. Leal for insights into DC repositioning; to M. Parsek and M. Zori for providing GFP-expressing *P. aeruginosa*, as well as for sharing their expertise and reagents for bacterial culture; to B. Gern and L. Cross for guidance on measuring bacterial loads; and to J. Hamerman, J. Woodward, K. Elkon, and S. Ziegler for thoughtful feedback on project directions.

Funding:

This work was supported by the NIH grants R01AI134713 (M.Y.G), F31AI161316 (J.Y.H.), and T32GM007270 (J.Y.H.).

Author contributions:

J.Y.H. and M.Y.G conceptualized the study. J.Y.H. performed all experiments and analyzed data. J.Y.H. and M.Y.G wrote, edited, and reviewed the manuscript. M.Y.G. supervised the project.

Declaration of generative AI and AI-assisted technologies in the writing process:

During the preparation of this manuscript the authors used ChatGPT (GPT-4o) to check word usage and grammatical correctness. After using this tool/service, the authors reviewed and edited the content as needed and take full responsibility for the content of the publication.

Chapter 5: Concluding remarks

This chapter is adapted from the following manuscript:

Huang JY, Lyons-Cohen MR, Gerner MY. Information flow in the spatiotemporal organization of immune responses. *Immunol Rev*. Mar 2022;306(1):93-107.doi:10.1111/imr.13046

In sum, the lymphatics are an information-rich superhighway that enables efficient crosstalk between peripheral tissues and the draining LNs. Such transmission of information is necessary for promoting immune quiescence at steady state, as well as for mounting productive immune responses during inflammation. During microbial infection or vaccination, the spatial organization of innate cells within LNs permits effective sampling of information and threat detection, as well as facilitates highly coordinated crosstalk among different immune cells to drive the generation of functional innate and adaptive responses. At the same time, the drainage patterns of antigens and agonists, coupled with localized innate cell positioning, generates discrete immune microenvironments which control the magnitude, quality, and heterogeneity of downstream adaptive immunity. Together, these large-scale and spatially orchestrated crosstalk events across tissues and among immune cell populations represent the mechanisms responsible for the appropriate generation of immune responses during type-I inflammation.

References

1. Oliver G, Kipnis J, Randolph GJ, Harvey NL. The Lymphatic Vasculature in the 21(st) Century: Novel Functional Roles in Homeostasis and Disease. *Cell*. Jul 23 2020;182(2):270-296. doi:10.1016/j.cell.2020.06.039
2. Petrova TV, Koh GY. Biological functions of lymphatic vessels. *Science*. Jul 10 2020;369(6500)doi:10.1126/science.aax4063
3. Randolph GJ, Ivanov S, Zinselmeyer BH, Scallan JP. The Lymphatic System: Integral Roles in Immunity. *Annu Rev Immunol*. Apr 26 2017;35:31-52. doi:10.1146/annurev-immunol-041015-055354
4. Clement CC, Cannizzo ES, Nastke MD, et al. An expanded self-antigen peptidome is carried by the human lymph as compared to the plasma. *PLoS One*. Mar 26 2010;5(3):e9863. doi:10.1371/journal.pone.0009863
5. Pflicke H, Sixt M. Preformed portals facilitate dendritic cell entry into afferent lymphatic vessels. *J Exp Med*. Dec 21 2009;206(13):2925-35. doi:10.1084/jem.20091739
6. Schineis P, Runge P, Halin C. Cellular traffic through afferent lymphatic vessels. *Vascul Pharmacol*. Jan 2019;112:31-41. doi:10.1016/j.vph.2018.08.001
7. Stern LJ, Santambrogio L. The melting pot of the MHC II peptidome. *Curr Opin Immunol*. Jun 2016;40:70-7. doi:10.1016/j.coi.2016.03.004
8. Baluk P, Fuxe J, Hashizume H, et al. Functionally specialized junctions between endothelial cells of lymphatic vessels. *J Exp Med*. Oct 1 2007;204(10):2349-62. doi:10.1084/jem.20062596
9. Bovay E, Sabine A, Prat-Luri B, et al. Multiple roles of lymphatic vessels in peripheral lymph node development. *J Exp Med*. Nov 5 2018;215(11):2760-2777. doi:10.1084/jem.20180217
10. Bogoslowski A, Kubes P. Lymph Nodes: The Unrecognized Barrier against Pathogens. *ACS Infect Dis*. Aug 10 2018;4(8):1158-1161. doi:10.1021/acsinfecdis.8b00111
11. Adair TH, Moffatt DS, Paulsen AW, Guyton AC. Quantitation of changes in lymph protein concentration during lymph node transit. *Am J Physiol*. Sep 1982;243(3):H351-9. doi:10.1152/ajpheart.1982.243.3.H351
12. Czepielewski RS, Randolph GJ. Lymph nodes go with the flow. *J Exp Med*. Nov 5 2018;215(11):2699-2701. doi:10.1084/jem.20181898
13. Gerner MY, Casey KA, Kastenmuller W, Germain RN. Dendritic cell and antigen dispersal landscapes regulate T cell immunity. *J Exp Med*. Oct 2 2017;214(10):3105-3122. doi:10.1084/jem.20170335
14. Kähäri L, Fair-Mäkelä R, Auvinen K, et al. Transcytosis route mediates rapid delivery of intact antibodies to draining lymph nodes. *J Clin Invest*. Jun 24 2019;129(8):3086-3102. doi:10.1172/jci125740
15. Qi H, Kastenmüller W, Germain RN. Spatiotemporal basis of innate and adaptive immunity in secondary lymphoid tissue. *Annu Rev Cell Dev Biol*. 2014;30:141-67. doi:10.1146/annurev-cellbio-100913-013254
16. Eisenbarth SC. Dendritic cell subsets in T cell programming: location dictates function. *Nat Rev Immunol*. Feb 2019;19(2):89-103. doi:10.1038/s41577-018-0088-1
17. Grant SM, Lou M, Yao L, Germain RN, Radtke AJ. The lymph node at a glance - how spatial organization optimizes the immune response. *J Cell Sci*. Mar 6 2020;133(5)doi:10.1242/jcs.241828

18. Gray EE, Cyster JG. Lymph node macrophages. *J Innate Immun*. 2012;4(5-6):424-36. doi:10.1159/000337007
19. Moran I, Grootveld AK, Nguyen A, Phan TG. Subcapsular Sinus Macrophages: The Seat of Innate and Adaptive Memory in Murine Lymph Nodes. *Trends Immunol*. Jan 2019;40(1):35-48. doi:10.1016/j.it.2018.11.004
20. Gray EE, Friend S, Suzuki K, Phan TG, Cyster JG. Subcapsular sinus macrophage fragmentation and CD169+ bleb acquisition by closely associated IL-17-committed innate-like lymphocytes. *PLoS One*. 2012;7(6):e38258. doi:10.1371/journal.pone.0038258
21. Kastenmüller W, Torabi-Parizi P, Subramanian N, Lämmermann T, Germain RN. A spatially-organized multicellular innate immune response in lymph nodes limits systemic pathogen spread. *Cell*. Sep 14 2012;150(6):1235-48. doi:10.1016/j.cell.2012.07.021
22. Zhang Y, Roth TL, Gray EE, et al. Migratory and adhesive cues controlling innate-like lymphocyte surveillance of the pathogen-exposed surface of the lymph node. *Elife*. Aug 3 2016;5doi:10.7554/eLife.18156
23. Chtanova T, Han SJ, Schaeffer M, et al. Dynamics of T cell, antigen-presenting cell, and pathogen interactions during recall responses in the lymph node. *Immunity*. Aug 21 2009;31(2):342-55. doi:10.1016/j.immuni.2009.06.023
24. Kastenmüller W, Brandes M, Wang Z, Herz J, Egen JG, Germain RN. Peripheral prepositioning and local CXCL9 chemokine-mediated guidance orchestrate rapid memory CD8+ T cell responses in the lymph node. *Immunity*. Mar 21 2013;38(3):502-13. doi:10.1016/j.immuni.2012.11.012
25. Böttcher JP, Beyer M, Meissner F, et al. Functional classification of memory CD8(+) T cells by CX3CR1 expression. *Nat Commun*. Sep 25 2015;6:8306. doi:10.1038/ncomms9306
26. Gerner MY, Kastenmuller W, Ifrim I, Kabat J, Germain RN. Histo-cytometry: a method for highly multiplex quantitative tissue imaging analysis applied to dendritic cell subset microanatomy in lymph nodes. *Immunity*. Aug 24 2012;37(2):364-76. doi:10.1016/j.immuni.2012.07.011
27. Gerner MY, Torabi-Parizi P, Germain RN. Strategically localized dendritic cells promote rapid T cell responses to lymph-borne particulate antigens. *Immunity*. Jan 20 2015;42(1):172-85. doi:10.1016/j.immuni.2014.12.024
28. Leal JM, Huang JY, Kohli K, et al. Innate cell microenvironments in lymph nodes shape the generation of T cell responses during type I inflammation. *Sci Immunol*. Feb 12 2021;6(56)doi:10.1126/sciimmunol.abb9435
29. Stoltzfus CR, Filipek J, Gern BH, et al. CytoMAP: A Spatial Analysis Toolbox Reveals Features of Myeloid Cell Organization in Lymphoid Tissues. *Cell Rep*. Apr 21 2020;31(3):107523. doi:10.1016/j.celrep.2020.107523
30. Eickhoff S, Brewitz A, Gerner MY, et al. Robust Anti-viral Immunity Requires Multiple Distinct T Cell-Dendritic Cell Interactions. *Cell*. Sep 10 2015;162(6):1322-37. doi:10.1016/j.cell.2015.08.004
31. Hor JL, Whitney PG, Zaid A, Brooks AG, Heath WR, Mueller SN. Spatiotemporally Distinct Interactions with Dendritic Cell Subsets Facilitates CD4+ and CD8+ T Cell Activation to Localized Viral Infection. *Immunity*. Sep 15 2015;43(3):554-65. doi:10.1016/j.immuni.2015.07.020
32. Ruhland MK, Roberts EW, Cai E, et al. Visualizing Synaptic Transfer of Tumor Antigens among Dendritic Cells. *Cancer Cell*. Jun 8 2020;37(6):786-799.e5. doi:10.1016/j.ccell.2020.05.002

33. Moussion C, Girard JP. Dendritic cells control lymphocyte entry to lymph nodes through high endothelial venules. *Nature*. Nov 13 2011;479(7374):542-6. doi:10.1038/nature10540
34. Granot T, Senda T, Carpenter DJ, et al. Dendritic Cells Display Subset and Tissue-Specific Maturation Dynamics over Human Life. *Immunity*. 03 21 2017;46(3):504-515. doi:10.1016/j.immuni.2017.02.019
35. Baratin M, Foray C, Demaria O, et al. Homeostatic NF-κB Signaling in Steady-State Migratory Dendritic Cells Regulates Immune Homeostasis and Tolerance. *Immunity*. Apr 21 2015;42(4):627-39. doi:10.1016/j.immuni.2015.03.003
36. Cabeza-Cabrerizo M, Cardoso A, Minutti CM, Pereira da Costa M, Reis ESC. Dendritic Cells Revisited. *Annu Rev Immunol*. Apr 26 2021;39:131-166. doi:10.1146/annurev-immunol-061020-053707
37. Devi KS, Anandasabapathy N. The origin of DCs and capacity for immunologic tolerance in central and peripheral tissues. *Semin Immunopathol*. Feb 2017;39(2):137-152. doi:10.1007/s00281-016-0602-0
38. Manicassamy S, Pulendran B. Dendritic cell control of tolerogenic responses. *Immunol Rev*. May 2011;241(1):206-27. doi:10.1111/j.1600-065X.2011.01015.x
39. Bastow CR, Bunting MD, Kara EE, et al. Scavenging of soluble and immobilized CCL21 by ACKR4 regulates peripheral dendritic cell emigration. *Proc Natl Acad Sci U S A*. Apr 27 2021;118(17)doi:10.1073/pnas.2025763118
40. Weber M, Hauschild R, Schwarz J, et al. Interstitial dendritic cell guidance by haptotactic chemokine gradients. *Science*. Jan 18 2013;339(6117):328-32. doi:10.1126/science.1228456
41. Worbs T, Hammerschmidt SI, Förster R. Dendritic cell migration in health and disease. *Nat Rev Immunol*. 01 2017;17(1):30-48. doi:10.1038/nri.2016.116
42. Kissenpfennig A, Henri S, Dubois B, et al. Dynamics and function of Langerhans cells in vivo: dermal dendritic cells colonize lymph node areas distinct from slower migrating Langerhans cells. *Immunity*. May 2005;22(5):643-54. doi:10.1016/j.immuni.2005.04.004
43. Kitano M, Yamazaki C, Takumi A, et al. Imaging of the cross-presenting dendritic cell subsets in the skin-draining lymph node. *Proc Natl Acad Sci U S A*. Jan 26 2016;113(4):1044-9. doi:10.1073/pnas.1513607113
44. Connor LM, Tang SC, Cognard E, et al. Th2 responses are primed by skin dendritic cells with distinct transcriptional profiles. *J Exp Med*. 01 2017;214(1):125-142. doi:10.1084/jem.20160470
45. Kumamoto Y, Linehan M, Weinstein JS, Laidlaw BJ, Craft JE, Iwasaki A. CD301b^{+} dermal dendritic cells drive T helper 2 cell-mediated immunity. *Immunity*. Oct 17 2013;39(4):733-43. doi:10.1016/j.immuni.2013.08.029
46. Ochiai S, Roediger B, Abtin A, et al. CD326(lo)CD103(lo)CD11b(lo) dermal dendritic cells are activated by thymic stromal lymphopoietin during contact sensitization in mice. *J Immunol*. Sep 1 2014;193(5):2504-11. doi:10.4049/jimmunol.1400536
47. Klein L, Kyewski B, Allen PM, Hogquist KA. Positive and negative selection of the T cell repertoire: what thymocytes see (and don't see). *Nat Rev Immunol*. Jun 2014;14(6):377-91. doi:10.1038/nri3667
48. Liu Z, Gerner MY, Van Panhuys N, Levine AG, Rudensky AY, Germain RN. Immune homeostasis enforced by co-localized effector and regulatory T cells. *Nature*. Dec 10 2015;528(7581):225-30. doi:10.1038/nature16169

49. Wong HS, Park K, Gola A, et al. A local regulatory T cell feedback circuit maintains immune homeostasis by pruning self-activated T cells. *Cell*. Jul 22 2021;184(15):3981-3997.e22. doi:10.1016/j.cell.2021.05.028
50. Gratz IK, Campbell DJ. Organ-specific and memory treg cells: specificity, development, function, and maintenance. *Front Immunol*. 2014;5:333. doi:10.3389/fimmu.2014.00333
51. Smigiel KS, Richards E, Srivastava S, et al. CCR7 provides localized access to IL-2 and defines homeostatically distinct regulatory T cell subsets. *J Exp Med*. Jan 13 2014;211(1):121-36. doi:10.1084/jem.20131142
52. Buszko M, Shevach EM. Control of regulatory T cell homeostasis. *Curr Opin Immunol*. Dec 2020;67:18-26. doi:10.1016/j.coi.2020.07.001
53. Alexandre YO, Mueller SN. Stromal cell networks coordinate immune response generation and maintenance. *Immunol Rev*. May 2018;283(1):77-85. doi:10.1111/imr.12641
54. Rodda LB, Lu E, Bennett ML, et al. Single-Cell RNA Sequencing of Lymph Node Stromal Cells Reveals Niche-Associated Heterogeneity. *Immunity*. May 15 2018;48(5):1014-1028.e6. doi:10.1016/j.immuni.2018.04.006
55. Krishnamurty AT, Turley SJ. Lymph node stromal cells: cartographers of the immune system. *Nat Immunol*. Apr 2020;21(4):369-380. doi:10.1038/s41590-020-0635-3
56. Pikor NB, Cheng HW, Onder L, Ludewig B. Development and Immunological Function of Lymph Node Stromal Cells. *J Immunol*. 01 15 2021;206(2):257-263. doi:10.4049/jimmunol.2000914
57. Kapoor VN, Müller S, Keerthivasan S, et al. Gremlin 1(+) fibroblastic niche maintains dendritic cell homeostasis in lymphoid tissues. *Nat Immunol*. May 2021;22(5):571-585. doi:10.1038/s41590-021-00920-6
58. Pikor NB, Mörbe U, Lütge M, et al. Remodeling of light and dark zone follicular dendritic cells governs germinal center responses. *Nat Immunol*. 06 2020;21(6):649-659. doi:10.1038/s41590-020-0672-y
59. Denton AE, Carr EJ, Magiera LP, Watts AJB, Fearon DT. Embryonic FAP. *J Exp Med*. 10 07 2019;216(10):2242-2252. doi:10.1084/jem.20181705
60. Camara A, Cordeiro OG, Alloush F, et al. Lymph Node Mesenchymal and Endothelial Stromal Cells Cooperate via the RANK-RANKL Cytokine Axis to Shape the Sinusoidal Macrophage Niche. *Immunity*. Jun 18 2019;50(6):1467-1481.e6. doi:10.1016/j.immuni.2019.05.008
61. Mondor I, Baratin M, Lagueyrie M, et al. Lymphatic Endothelial Cells Are Essential Components of the Subcapsular Sinus Macrophage Niche. *Immunity*. Jun 18 2019;50(6):1453-1466.e4. doi:10.1016/j.immuni.2019.04.002
62. Ulvmar MH, Werth K, Braun A, et al. The atypical chemokine receptor CCRL1 shapes functional CCL21 gradients in lymph nodes. *Nat Immunol*. Jul 2014;15(7):623-30. doi:10.1038/ni.2889
63. Bajénoff M, Egen JG, Koo LY, et al. Stromal cell networks regulate lymphocyte entry, migration, and territoriality in lymph nodes. *Immunity*. Dec 2006;25(6):989-1001. doi:10.1016/j.immuni.2006.10.011
64. Crotty S. T Follicular Helper Cell Biology: A Decade of Discovery and Diseases. *Immunity*. May 21 2019;50(5):1132-1148. doi:10.1016/j.immuni.2019.04.011
65. León B, Ballesteros-Tato A, Browning JL, Dunn R, Randall TD, Lund FE. Regulation of T(H)2 development by CXCR5+ dendritic cells and lymphotoxin-expressing B cells. *Nat Immunol*. May 27 2012;13(7):681-90. doi:10.1038/ni.2309

66. Wang X, Cho B, Suzuki K, et al. Follicular dendritic cells help establish follicle identity and promote B cell retention in germinal centers. *J Exp Med*. Nov 21 2011;208(12):2497-510. doi:10.1084/jem.20111449
67. Link A, Vogt TK, Favre S, et al. Fibroblastic reticular cells in lymph nodes regulate the homeostasis of naive T cells. *Nat Immunol*. Nov 2007;8(11):1255-65. doi:10.1038/ni1513
68. Luther SA, Tang HL, Hyman PL, Farr AG, Cyster JG. Coexpression of the chemokines ELC and SLC by T zone stromal cells and deletion of the ELC gene in the plt/plt mouse. *Proc Natl Acad Sci U S A*. Nov 7 2000;97(23):12694-9. doi:10.1073/pnas.97.23.12694
69. Mueller SN, Germain RN. Stromal cell contributions to the homeostasis and functionality of the immune system. *Nat Rev Immunol*. Sep 2009;9(9):618-29. doi:10.1038/nri2588
70. Schumann K, Lämmermann T, Bruckner M, et al. Immobilized chemokine fields and soluble chemokine gradients cooperatively shape migration patterns of dendritic cells. *Immunity*. May 28 2010;32(5):703-13. doi:10.1016/j.immuni.2010.04.017
71. Gatto D, Wood K, Caminschi I, et al. The chemotactic receptor EBI2 regulates the homeostasis, localization and immunological function of splenic dendritic cells. *Nat Immunol*. May 2013;14(5):446-53. doi:10.1038/ni.2555
72. Lu E, Dang EV, McDonald JG, Cyster JG. Distinct oxysterol requirements for positioning naïve and activated dendritic cells in the spleen. *Sci Immunol*. Apr 7 2017;2(10)doi:10.1126/sciimmunol.aal5237
73. Yi T, Cyster JG. EBI2-mediated bridging channel positioning supports splenic dendritic cell homeostasis and particulate antigen capture. *Elife*. May 14 2013;2:e00757. doi:10.7554/eLife.00757
74. Baptista AP, Gola A, Huang Y, et al. The Chemoattractant Receptor Ebi2 Drives Intranodal Naive CD4(+) T Cell Peripheralization to Promote Effective Adaptive Immunity. *Immunity*. May 21 2019;50(5):1188-1201.e6. doi:10.1016/j.immuni.2019.04.001
75. Brulois K, Rajaraman A, Szade A, et al. A molecular map of murine lymph node blood vascular endothelium at single cell resolution. *Nat Commun*. Jul 30 2020;11(1):3798. doi:10.1038/s41467-020-17291-5
76. Veerman K, Tardiveau C, Martins F, Coudert J, Girard JP. Single-Cell Analysis Reveals Heterogeneity of High Endothelial Venules and Different Regulation of Genes Controlling Lymphocyte Entry to Lymph Nodes. *Cell Rep*. Mar 12 2019;26(11):3116-3131.e5. doi:10.1016/j.celrep.2019.02.042
77. Cabeza-Cabrerizo M, van Blijswijk J, Wienert S, et al. Tissue clonality of dendritic cell subsets and emergency DCpoiesis revealed by multicolor fate mapping of DC progenitors. *Sci Immunol*. Mar 1 2019;4(33)doi:10.1126/sciimmunol.aaw1941
78. Grajales-Reyes GE, Iwata A, Albring J, et al. Batf3 maintains autoactivation of Irf8 for commitment of a CD8α(+) conventional DC clonogenic progenitor. *Nat Immunol*. Jul 2015;16(7):708-17. doi:10.1038/ni.3197
79. Schlitzer A, Sivakamasundari V, Chen J, et al. Identification of cDC1- and cDC2-committed DC progenitors reveals early lineage priming at the common DC progenitor stage in the bone marrow. *Nat Immunol*. Jul 2015;16(7):718-28. doi:10.1038/ni.3200
80. Baptista AP, Gerner MY. Lymphoid stromal cells proGrem dendritic cell homeostasis. *Nat Immunol*. 05 2021;22(5):541-543. doi:10.1038/s41590-021-00924-2
81. Acton SE, Astarita JL, Malhotra D, et al. Podoplanin-rich stromal networks induce dendritic cell motility via activation of the C-type lectin receptor CLEC-2. *Immunity*. Aug 24 2012;37(2):276-89. doi:10.1016/j.immuni.2012.05.022

82. Acton SE, Farrugia AJ, Astarita JL, et al. Dendritic cells control fibroblastic reticular network tension and lymph node expansion. *Nature*. Oct 23 2014;514(7523):498-502. doi:10.1038/nature13814
83. Astarita JL, Cremasco V, Fu J, et al. The CLEC-2-podoplanin axis controls the contractility of fibroblastic reticular cells and lymph node microarchitecture. *Nat Immunol*. Jan 2015;16(1):75-84. doi:10.1038/ni.3035
84. Dasoveanu DC, Shipman WD, Chia JJ, Chyou S, Lu TT. Regulation of Lymph Node Vascular-Stromal Compartment by Dendritic Cells. *Trends Immunol*. Nov 2016;37(11):764-777. doi:10.1016/j.it.2016.08.013
85. Kumar V, Dasoveanu DC, Chyou S, et al. A dendritic-cell-stromal axis maintains immune responses in lymph nodes. *Immunity*. Apr 21 2015;42(4):719-30. doi:10.1016/j.immuni.2015.03.015
86. Merad M, Sathe P, Helft J, Miller J, Mortha A. The dendritic cell lineage: ontogeny and function of dendritic cells and their subsets in the steady state and the inflamed setting. *Annu Rev Immunol*. 2013;31:563-604. doi:10.1146/annurev-immunol-020711-074950
87. Heath WR, Carbone FR. Dendritic cell subsets in primary and secondary T cell responses at body surfaces. *Nat Immunol*. Dec 2009;10(12):1237-44. doi:10.1038/ni.1822
88. Villadangos JA, Schnorrer P. Intrinsic and cooperative antigen-presenting functions of dendritic-cell subsets in vivo. *Nat Rev Immunol*. Jul 2007;7(7):543-55. doi:10.1038/nri2103
89. Gonzalez SF, Lukacs-Kornek V, Kuligowski MP, et al. Capture of influenza by medullary dendritic cells via SIGN-R1 is essential for humoral immunity in draining lymph nodes. *Nat Immunol*. May 2010;11(5):427-34. doi:10.1038/ni.1856
90. Roozendaal R, Mempel TR, Pitcher LA, et al. Conduits mediate transport of low-molecular-weight antigen to lymph node follicles. *Immunity*. Feb 20 2009;30(2):264-76. doi:10.1016/j.immuni.2008.12.014
91. Brewitz A, Eickhoff S, Dähling S, et al. CD8(+) T Cells Orchestrate pDC-XCR1(+) Dendritic Cell Spatial and Functional Cooperativity to Optimize Priming. *Immunity*. Feb 21 2017;46(2):205-219. doi:10.1016/j.immuni.2017.01.003
92. Celli S, Garcia Z, Bousso P. CD4 T cells integrate signals delivered during successive DC encounters in vivo. *J Exp Med*. Nov 07 2005;202(9):1271-8. doi:10.1084/jem.20051018
93. Nakano H, Lin KL, Yanagita M, et al. Blood-derived inflammatory dendritic cells in lymph nodes stimulate acute T helper type 1 immune responses. *Nat Immunol*. Apr 2009;10(4):394-402. doi:10.1038/ni.1707
94. De Koker S, Van Hoecke L, De Beuckelaer A, et al. Inflammatory monocytes regulate Th1 oriented immunity to CpG adjuvanted protein vaccines through production of IL-12. *Sci Rep*. Jul 20 2017;7(1):5986. doi:10.1038/s41598-017-06236-6
95. Jakubzick CV, Randolph GJ, Henson PM. Monocyte differentiation and antigen-presenting functions. *Nat Rev Immunol*. Jun 2017;17(6):349-362. doi:10.1038/nri.2017.28
96. Jakubzick C, Gautier EL, Gibbings SL, et al. Minimal differentiation of classical monocytes as they survey steady-state tissues and transport antigen to lymph nodes. *Immunity*. Sep 19 2013;39(3):599-610. doi:10.1016/j.immuni.2013.08.007
97. Leirião P, del Fresno C, Ardavín C. Monocytes as effector cells: activated Ly-6C(high) mouse monocytes migrate to the lymph nodes through the lymph and cross-present antigens to CD8+ T cells. *Eur J Immunol*. Aug 2012;42(8):2042-51. doi:10.1002/eji.201142166

98. Palframan RT, Jung S, Cheng G, et al. Inflammatory chemokine transport and presentation in HEV: a remote control mechanism for monocyte recruitment to lymph nodes in inflamed tissues. *J Exp Med*. Nov 5 2001;194(9):1361-73. doi:10.1084/jem.194.9.1361
99. Shi C, Pamer EG. Monocyte recruitment during infection and inflammation. *Nat Rev Immunol*. Oct 10 2011;11(11):762-74. doi:10.1038/nri3070
100. Groom JR. Regulators of T-cell fate: Integration of cell migration, differentiation and function. *Immunol Rev*. May 2019;289(1):101-114. doi:10.1111/imr.12742
101. Woodruff MC, Heesters BA, Herndon CN, et al. Trans-nodal migration of resident dendritic cells into medullary interfollicular regions initiates immunity to influenza vaccine. *J Exp Med*. Jul 28 2014;211(8):1611-21. doi:10.1084/jem.20132327
102. Grassmann S, Mihatsch L, Mir J, et al. Early emergence of T central memory precursors programs clonal dominance during chronic viral infection. *Nat Immunol*. Dec 2020;21(12):1563-1573. doi:10.1038/s41590-020-00807-y
103. Buchholz VR, Flossdorf M, Hensel I, et al. Disparate individual fates compose robust CD8+ T cell immunity. *Science*. May 03 2013;340(6132):630-5. doi:10.1126/science.1235454
104. Gerlach C, Rohr JC, Perié L, et al. Heterogeneous differentiation patterns of individual CD8+ T cells. *Science*. May 03 2013;340(6132):635-9. doi:10.1126/science.1235487
105. Plumlee CR, Sheridan BS, Cicek BB, Lefrançois L. Environmental cues dictate the fate of individual CD8+ T cells responding to infection. *Immunity*. Aug 22 2013;39(2):347-56. doi:10.1016/j.immuni.2013.07.014
106. Annunziato F, Romagnani C, Romagnani S. The 3 major types of innate and adaptive cell-mediated effector immunity. *J Allergy Clin Immunol*. Mar 2015;135(3):626-35. doi:10.1016/j.jaci.2014.11.001
107. Gause WC, Wynn TA, Allen JE. Type 2 immunity and wound healing: evolutionary refinement of adaptive immunity by helminths. *Nat Rev Immunol*. Aug 2013;13(8):607-14. doi:10.1038/nri3476
108. Spellberg B, Edwards JE. Type 1/Type 2 immunity in infectious diseases. *Clin Infect Dis*. Jan 2001;32(1):76-102. doi:10.1086/317537
109. Yip HC, Karulin AY, Tary-Lehmann M, et al. Adjuvant-guided type-1 and type-2 immunity: infectious/noninfectious dichotomy defines the class of response. *J Immunol*. Apr 01 1999;162(7):3942-9.
110. Liu H, Moynihan KD, Zheng Y, et al. Structure-based programming of lymph-node targeting in molecular vaccines. *Nature*. Mar 27 2014;507(7493):519-22. doi:10.1038/nature12978
111. Langlet C, Tamoutounour S, Henri S, et al. CD64 expression distinguishes monocyte-derived and conventional dendritic cells and reveals their distinct role during intramuscular immunization. *J Immunol*. Feb 15 2012;188(4):1751-60. doi:10.4049/jimmunol.1102744
112. Plantinga M, Guilliams M, Vanheerswynghels M, et al. Conventional and monocyte-derived CD11b(+) dendritic cells initiate and maintain T helper 2 cell-mediated immunity to house dust mite allergen. *Immunity*. Feb 21 2013;38(2):322-35. doi:10.1016/j.immuni.2012.10.016
113. Lämmermann T, Kastenmüller W. Concepts of GPCR-controlled navigation in the immune system. *Immunol Rev*. May 2019;289(1):205-231. doi:10.1111/imr.12752
114. Förster R, Schubel A, Breitfeld D, et al. CCR7 coordinates the primary immune response by establishing functional microenvironments in secondary lymphoid organs. *Cell*. Oct 01 1999;99(1):23-33. doi:10.1016/s0092-8674(00)80059-8

115. Ohl L, Mohaupt M, Czeloth N, et al. CCR7 governs skin dendritic cell migration under inflammatory and steady-state conditions. *Immunity*. Aug 2004;21(2):279-88. doi:10.1016/j.immuni.2004.06.014
116. Calabro S, Liu D, Gallman A, et al. Differential Intrasplenic Migration of Dendritic Cell Subsets Tailors Adaptive Immunity. *Cell Rep*. Aug 30 2016;16(9):2472-85. doi:10.1016/j.celrep.2016.07.076
117. De Becker G, Moulin V, Pajak B, et al. The adjuvant monophosphoryl lipid A increases the function of antigen-presenting cells. *Int Immunol*. Jun 2000;12(6):807-15. doi:10.1093/intimm/12.6.807
118. De Trez C, Pajak B, Brait M, et al. TLR4 and Toll-IL-1 receptor domain-containing adapter-inducing IFN-beta, but not MyD88, regulate Escherichia coli-induced dendritic cell maturation and apoptosis in vivo. *J Immunol*. Jul 15 2005;175(2):839-46. doi:10.4049/jimmunol.175.2.839
119. Li J, Lu E, Yi T, Cyster JG. EBI2 augments Tfh cell fate by promoting interaction with IL-2-quenching dendritic cells. *Nature*. May 5 2016;533(7601):110-4. doi:10.1038/nature17947
120. Meredith MM, Liu K, Darrasse-Jeze G, et al. Expression of the zinc finger transcription factor zDC (Zbtb46, Btbd4) defines the classical dendritic cell lineage. *J Exp Med*. Jun 04 2012;209(6):1153-65. doi:10.1084/jem.20112675
121. Itano AA, McSorley SJ, Reinhardt RL, et al. Distinct dendritic cell populations sequentially present antigen to CD4 T cells and stimulate different aspects of cell-mediated immunity. *Immunity*. Jul 2003;19(1):47-57. doi:10.1016/s1074-7613(03)00175-4
122. Shi C, Jia T, Mendez-Ferrer S, et al. Bone marrow mesenchymal stem and progenitor cells induce monocyte emigration in response to circulating toll-like receptor ligands. *Immunity*. Apr 22 2011;34(4):590-601. doi:10.1016/j.immuni.2011.02.016
123. Nourshargh S, Alon R. Leukocyte migration into inflamed tissues. *Immunity*. Nov 20 2014;41(5):694-707. doi:10.1016/j.immuni.2014.10.008
124. Girard JP, Moussion C, Förster R. HEVs, lymphatics and homeostatic immune cell trafficking in lymph nodes. *Nat Rev Immunol*. Nov 2012;12(11):762-73. doi:10.1038/nri3298
125. Woodfin A, Voisin MB, Beyrau M, et al. The junctional adhesion molecule JAM-C regulates polarized transendothelial migration of neutrophils in vivo. *Nat Immunol*. Jun 26 2011;12(8):761-9. doi:10.1038/ni.2062
126. Zhang HH, Song K, Rabin RL, et al. CCR2 identifies a stable population of human effector memory CD4+ T cells equipped for rapid recall response. *J Immunol*. Dec 01 2010;185(11):6646-63. doi:10.4049/jimmunol.0904156
127. Zigmond E, Varol C, Farache J, et al. Ly6C hi monocytes in the inflamed colon give rise to proinflammatory effector cells and migratory antigen-presenting cells. *Immunity*. Dec 14 2012;37(6):1076-90. doi:10.1016/j.immuni.2012.08.026
128. Bosteels C, Neyt K, Vanheerswynghels M, et al. Inflammatory Type 2 cDCs Acquire Features of cDC1s and Macrophages to Orchestrate Immunity to Respiratory Virus Infection. *Immunity*. Jun 16 2020;52(6):1039-1056.e9. doi:10.1016/j.immuni.2020.04.005
129. Krishnamoorthy V, Kannanganat S, Maienschein-Cline M, et al. The IRF4 Gene Regulatory Module Functions as a Read-Write Integrator to Dynamically Coordinate T Helper Cell Fate. *Immunity*. Sep 19 2017;47(3):481-497.e7. doi:10.1016/j.immuni.2017.09.001
130. Man K, Miasari M, Shi W, et al. The transcription factor IRF4 is essential for TCR affinity-mediated metabolic programming and clonal expansion of T cells. *Nat Immunol*. Nov 2013;14(11):1155-65. doi:10.1038/ni.2710

131. Schreiber HA, Loschko J, Karssemeijer RA, et al. Intestinal monocytes and macrophages are required for T cell polarization in response to Citrobacter rodentium. *J Exp Med*. Sep 23 2013;210(10):2025-39. doi:10.1084/jem.20130903
132. Martínez-López M, Iborra S, Conde-Garrosa R, Sancho D. Batf3-dependent CD103+ dendritic cells are major producers of IL-12 that drive local Th1 immunity against Leishmania major infection in mice. *Eur J Immunol*. Jan 2015;45(1):119-29. doi:10.1002/eji.201444651
133. Mashayekhi M, Sandau MM, Dunay IR, et al. CD8α(+) dendritic cells are the critical source of interleukin-12 that controls acute infection by Toxoplasma gondii tachyzoites. *Immunity*. Aug 26 2011;35(2):249-59. doi:10.1016/j.immuni.2011.08.008
134. Reinhardt RL, Hong S, Kang SJ, Wang ZE, Locksley RM. Visualization of IL-12/23p40 in vivo reveals immunostimulatory dendritic cell migrants that promote Th1 differentiation. *J Immunol*. Aug 1 2006;177(3):1618-27. doi:10.4049/jimmunol.177.3.1618
135. Conejero L, Khouili SC, Martínez-Cano S, Izquierdo HM, Brandi P, Sancho D. Lung CD103+ dendritic cells restrain allergic airway inflammation through IL-12 production. *JCI Insight*. May 18 2017;2(10)doi:10.1172/jci.insight.90420
136. Everts B, Tussiwand R, Dreesen L, et al. Migratory CD103+ dendritic cells suppress helminth-driven type 2 immunity through constitutive expression of IL-12. *J Exp Med*. Jan 11 2016;213(1):35-51. doi:10.1084/jem.20150235
137. Borges da Silva H, Wang H, Qian LJ, Hogquist KA, Jameson SC. ARTC2.2/P2RX7 Signaling during Cell Isolation Distorts Function and Quantification of Tissue-Resident CD8. *J Immunol*. Apr 01 2019;202(7):2153-2163. doi:10.4049/jimmunol.1801613
138. Steinert EM, Schenkel JM, Fraser KA, et al. Quantifying Memory CD8 T Cells Reveals Regionalization of Immunosurveillance. *Cell*. May 07 2015;161(4):737-49. doi:10.1016/j.cell.2015.03.031
139. Curtsinger JM, Mescher MF. Inflammatory cytokines as a third signal for T cell activation. *Curr Opin Immunol*. Jun 2010;22(3):333-40. doi:10.1016/j.coi.2010.02.013
140. Zhu J, Yamane H, Paul WE. Differentiation of effector CD4 T cell populations (*). *Annu Rev Immunol*. 2010;28:445-89. doi:10.1146/annurev-immunol-030409-101212
141. Mempel TR, Henrickson SE, Von Andrian UH. T-cell priming by dendritic cells in lymph nodes occurs in three distinct phases. *Nature*. Jan 08 2004;427(6970):154-9. doi:10.1038/nature02238
142. Bajaña S, Roach K, Turner S, Paul J, Kovats S. IRF4 promotes cutaneous dendritic cell migration to lymph nodes during homeostasis and inflammation. *J Immunol*. Oct 01 2012;189(7):3368-77. doi:10.4049/jimmunol.1102613
143. Krishnaswamy JK, Gowthaman U, Zhang B, et al. Migratory CD11b(+) conventional dendritic cells induce T follicular helper cell-dependent antibody responses. *Sci Immunol*. Dec 1 2017;2(18)doi:10.1126/sciimmunol.aam9169
144. Vander Lugt B, Khan AA, Hackney JA, et al. Transcriptional programming of dendritic cells for enhanced MHC class II antigen presentation. *Nat Immunol*. Feb 2014;15(2):161-7. doi:10.1038/ni.2795
145. Igyártó BZ, Haley K, Ortner D, et al. Skin-resident murine dendritic cell subsets promote distinct and opposing antigen-specific T helper cell responses. *Immunity*. Aug 26 2011;35(2):260-72. doi:10.1016/j.immuni.2011.06.005
146. Lee HK, Zamora M, Linehan MM, et al. Differential roles of migratory and resident DCs in T cell priming after mucosal or skin HSV-1 infection. *J Exp Med*. Feb 16 2009;206(2):359-70. doi:10.1084/jem.20080601

147. Levin C, Bonduelle O, Nuttens C, et al. Critical Role for Skin-Derived Migratory DCs and Langerhans Cells in T_{FH} and GC responses after intradermal immunization. *J Invest Dermatol*. Sep 2017;137(9):1905-1913. doi:10.1016/j.jid.2017.04.016
148. Allan RS, Waithman J, Bedoui S, et al. Migratory dendritic cells transfer antigen to a lymph node-resident dendritic cell population for efficient CTL priming. *Immunity*. Jul 2006;25(1):153-62. doi:10.1016/j.immuni.2006.04.017
149. Kohli K, Janssen A, Förster R. Plasmacytoid dendritic cells induce tolerance predominantly by cargoing antigen to lymph nodes. *Eur J Immunol*. Nov 2016;46(11):2659-2668. doi:10.1002/eji.201646359
150. Srivastava S, Ernst JD. Cell-to-cell transfer of M. tuberculosis antigens optimizes CD4 T cell priming. *Cell Host Microbe*. Jun 11 2014;15(6):741-52. doi:10.1016/j.chom.2014.05.007
151. Hutchison S, Benson RA, Gibson VB, Pollock AH, Garside P, Brewer JM. Antigen depot is not required for alum adjuvanticity. *FASEB J*. Mar 2012;26(3):1272-9. doi:10.1096/fj.11-184556
152. Schudel A, Francis DM, Thomas SN. Material design for lymph node drug delivery. *Nat Rev Mater*. Jun 2019;4(6):415-428. doi:10.1038/s41578-019-0110-7
153. Gautier EL, Shay T, Miller J, et al. Gene-expression profiles and transcriptional regulatory pathways that underlie the identity and diversity of mouse tissue macrophages. *Nat Immunol*. Nov 2012;13(11):1118-28. doi:10.1038/ni.2419
154. Miller JC, Brown BD, Shay T, et al. Deciphering the transcriptional network of the dendritic cell lineage. *Nat Immunol*. Sep 2012;13(9):888-99. doi:10.1038/ni.2370
155. Villani AC, Satija R, Reynolds G, et al. Single-cell RNA-seq reveals new types of human blood dendritic cells, monocytes, and progenitors. *Science*. Apr 21 2017;356(6335)doi:10.1126/science.aah4573
156. Blecher-Gonen R, Bost P, Hilligan KL, et al. Single-Cell Analysis of Diverse Pathogen Responses Defines a Molecular Roadmap for Generating Antigen-Specific Immunity. *Cell Syst*. Feb 27 2019;8(2):109-121.e6. doi:10.1016/j.cels.2019.01.001
157. Longhi MP, Trumpfheller C, Idoyaga J, et al. Dendritic cells require a systemic type I interferon response to mature and induce CD4+ Th1 immunity with poly IC as adjuvant. *J Exp Med*. Jul 06 2009;206(7):1589-602. doi:10.1084/jem.20090247
158. Spörri R, Reis e Sousa C. Inflammatory mediators are insufficient for full dendritic cell activation and promote expansion of CD4+ T cell populations lacking helper function. *Nat Immunol*. Feb 2005;6(2):163-70. doi:10.1038/ni1162
159. Hochrein H, Shortman K, Vremec D, Scott B, Hertzog P, O'Keeffe M. Differential production of IL-12, IFN-alpha, and IFN-gamma by mouse dendritic cell subsets. *J Immunol*. May 01 2001;166(9):5448-55. doi:10.4049/jimmunol.166.9.5448
160. Reis e Sousa C, Hieny S, Scharton-Kersten T, et al. In vivo microbial stimulation induces rapid CD40 ligand-independent production of interleukin 12 by dendritic cells and their redistribution to T cell areas. *J Exp Med*. Dec 01 1997;186(11):1819-29. doi:10.1084/jem.186.11.1819
161. Crotty S. Follicular helper CD4 T cells (TFH). *Annu Rev Immunol*. 2011;29:621-63. doi:10.1146/annurev-immunol-031210-101400
162. Groom JR, Richmond J, Murooka TT, et al. CXCR3 chemokine receptor-ligand interactions in the lymph node optimize CD4+ T helper 1 cell differentiation. *Immunity*. Dec 14 2012;37(6):1091-103. doi:10.1016/j.immuni.2012.08.016

163. Lehmann CH, Heger L, Heidkamp GF, et al. Direct Delivery of Antigens to Dendritic Cells via Antibodies Specific for Endocytic Receptors as a Promising Strategy for Future Therapies. *Vaccines (Basel)*. Mar 28 2016;4(2)doi:10.3390/vaccines4020008
164. Moyer TJ, Zmolek AC, Irvine DJ. Beyond antigens and adjuvants: formulating future vaccines. *J Clin Invest*. Mar 01 2016;126(3):799-808. doi:10.1172/JCI81083
165. Guilliams M, van de Laar L. A Hitchhiker's Guide to Myeloid Cell Subsets: Practical Implementation of a Novel Mononuclear Phagocyte Classification System. *Front Immunol*. 2015;6:406. doi:10.3389/fimmu.2015.00406
166. Hohl TM, Rivera A, Lipuma L, et al. Inflammatory monocytes facilitate adaptive CD4 T cell responses during respiratory fungal infection. *Cell Host Microbe*. Nov 19 2009;6(5):470-81. doi:10.1016/j.chom.2009.10.007
167. Smith KD, Andersen-Nissen E, Hayashi F, et al. Toll-like receptor 5 recognizes a conserved site on flagellin required for protofilament formation and bacterial motility. *Nat Immunol*. Dec 2003;4(12):1247-53. doi:10.1038/ni1011
168. Nadjsombati MS, McGinty JW, Lyons-Cohen MR, et al. Detection of Succinate by Intestinal Tuft Cells Triggers a Type 2 Innate Immune Circuit. *Immunity*. Jul 17 2018;49(1):33-41.e7. doi:10.1016/j.immuni.2018.06.016
169. Mack M, Cihak J, Simonis C, et al. Expression and characterization of the chemokine receptors CCR2 and CCR5 in mice. *J Immunol*. Apr 01 2001;166(7):4697-704. doi:10.4049/jimmunol.166.7.4697
170. Anderson KG, Mayer-Barber K, Sung H, et al. Intravascular staining for discrimination of vascular and tissue leukocytes. *Nat Protoc*. Jan 2014;9(1):209-22. doi:10.1038/nprot.2014.005
171. Fletcher AL, Malhotra D, Acton SE, et al. Reproducible isolation of lymph node stromal cells reveals site-dependent differences in fibroblastic reticular cells. *Front Immunol*. 2011;2:35. doi:10.3389/fimmu.2011.00035
172. Sokol CL, Camire RB, Jones MC, Luster AD. The Chemokine Receptor CCR8 Promotes the Migration of Dendritic Cells into the Lymph Node Parenchyma to Initiate the Allergic Immune Response. *Immunity*. Sep 18 2018;49(3):449-463.e6. doi:10.1016/j.immuni.2018.07.012
173. Carrasco YR, Batista FD. B cells acquire particulate antigen in a macrophage-rich area at the boundary between the follicle and the subcapsular sinus of the lymph node. *Immunity*. Jul 2007;27(1):160-71. doi:10.1016/j.immuni.2007.06.007
174. Junt T, Moseman EA, Iannacone M, et al. Subcapsular sinus macrophages in lymph nodes clear lymph-borne viruses and present them to antiviral B cells. *Nature*. Nov 1 2007;450(7166):110-4. doi:10.1038/nature06287
175. Phan TG, Grigorova I, Okada T, Cyster JG. Subcapsular encounter and complement-dependent transport of immune complexes by lymph node B cells. *Nat Immunol*. Sep 2007;8(9):992-1000. doi:10.1038/ni1494
176. Phan TG, Green JA, Gray EE, Xu Y, Cyster JG. Immune complex relay by subcapsular sinus macrophages and noncognate B cells drives antibody affinity maturation. *Nat Immunol*. Jul 2009;10(7):786-93. doi:10.1038/ni.1745
177. Farrell HE, Bruce K, Lawler C, Cardin RD, Davis-Poynter NJ, Stevenson PG. Type 1 Interferons and NK Cells Limit Murine Cytomegalovirus Escape from the Lymph Node Subcapsular Sinus. *PLoS Pathog*. Dec 2016;12(12):e1006069. doi:10.1371/journal.ppat.1006069
178. Iannacone M, Moseman EA, Tonti E, et al. Subcapsular sinus macrophages prevent CNS invasion on peripheral infection with a neurotropic virus. *Nature*. Jun 24 2010;465(7301):1079-83. doi:10.1038/nature09118

179. Moseman EA, Iannacone M, Bosurgi L, et al. B cell maintenance of subcapsular sinus macrophages protects against a fatal viral infection independent of adaptive immunity. *Immunity*. Mar 23 2012;36(3):415-26. doi:10.1016/j.immuni.2012.01.013
180. Sagoo P, Garcia Z, Breart B, et al. In vivo imaging of inflammasome activation reveals a subcapsular macrophage burst response that mobilizes innate and adaptive immunity. *Nat Med*. Jan 2016;22(1):64-71. doi:10.1038/nm.4016
181. Bogoslowski A, Butcher EC, Kubes P. Neutrophils recruited through high endothelial venules of the lymph nodes via PNAd intercept disseminating Staphylococcus aureus. *Proc Natl Acad Sci U S A*. Mar 6 2018;115(10):2449-2454. doi:10.1073/pnas.1715756115
182. Lämmermann T, Afonso PV, Angermann BR, et al. Neutrophil swarms require LTB4 and integrins at sites of cell death in vivo. *Nature*. Jun 20 2013;498(7454):371-5. doi:10.1038/nature12175
183. Kienle K, Glaser KM, Eickhoff S, et al. Neutrophils self-limit swarming to contain bacterial growth in vivo. *Science*. Jun 18 2021;372(6548)doi:10.1126/science.abe7729
184. Sung JH, Zhang H, Moseman EA, et al. Chemokine guidance of central memory T cells is critical for antiviral recall responses in lymph nodes. *Cell*. Sep 14 2012;150(6):1249-63. doi:10.1016/j.cell.2012.08.015
185. Guarda G, Hons M, Soriano SF, et al. L-selectin-negative CCR7- effector and memory CD8+ T cells enter reactive lymph nodes and kill dendritic cells. *Nat Immunol*. Jul 2007;8(7):743-52. doi:10.1038/ni1469
186. Lian J, Ozga AJ, Sokol CL, Luster AD. Targeting Lymph Node Niches Enhances Type 1 Immune Responses to Immunization. *Cell Rep*. May 26 2020;31(8):107679. doi:10.1016/j.celrep.2020.107679
187. Duckworth BC, Lafouresse F, Wimmer VC, et al. Effector and stem-like memory cell fates are imprinted in distinct lymph node niches directed by CXCR3 ligands. *Nat Immunol*. Apr 2021;22(4):434-448. doi:10.1038/s41590-021-00878-5
188. Hilligan KL, Tang SC, Hyde EJ, et al. Dermal IRF4+ dendritic cells and monocytes license CD4+ T helper cells to distinct cytokine profiles. *Nat Commun*. 11 06 2020;11(1):5637. doi:10.1038/s41467-020-19463-9
189. Mendoza A, Yewdell WT, Hoyos B, et al. Assembly of a spatial circuit of T-bet-expressing T and B lymphocytes is required for antiviral humoral immunity. *Sci Immunol*. Jun 11 2021;6(60)doi:10.1126/sciimmunol.abi4710
190. Alexandre YO, Ghilas S, Sanchez C, Le Bon A, Crozat K, Dalod M. XCR1+ dendritic cells promote memory CD8+ T cell recall upon secondary infections with Listeria monocytogenes or certain viruses. *J Exp Med*. Jan 11 2016;213(1):75-92. doi:10.1084/jem.20142350
191. Askenase MH, Han SJ, Byrd AL, et al. Bone-Marrow-Resident NK Cells Prime Monocytes for Regulatory Function during Infection. *Immunity*. Jun 16 2015;42(6):1130-42. doi:10.1016/j.immuni.2015.05.011
192. Goldszmid RS, Caspar P, Rivollier A, et al. NK cell-derived interferon-γ orchestrates cellular dynamics and the differentiation of monocytes into dendritic cells at the site of infection. *Immunity*. Jun 29 2012;36(6):1047-59. doi:10.1016/j.immuni.2012.03.026
193. Ghilas S, Ambrosini M, Cancel JC, et al. Natural killer cells and dendritic epidermal γδ T cells orchestrate type 1 conventional DC spatiotemporal repositioning toward CD8(+) T cells. *iScience*. Sep 24 2021;24(9):103059. doi:10.1016/j.isci.2021.103059

194. Lee AJ, Chen B, Chew MV, et al. Inflammatory monocytes require type I interferon receptor signaling to activate NK cells via IL-18 during a mucosal viral infection. *J Exp Med*. Apr 3 2017;214(4):1153-1167. doi:10.1084/jem.20160880
195. Askew D, Su CA, Barkauskas DS, et al. Transient Surface CCR5 Expression by Naive CD8+ T Cells within Inflamed Lymph Nodes Is Dependent on High Endothelial Venule Interaction and Augments Th Cell-Dependent Memory Response. *J Immunol*. May 1 2016;196(9):3653-64. doi:10.4049/jimmunol.1501176
196. Castellino F, Huang AY, Altan-Bonnet G, Stoll S, Scheinecker C, Germain RN. Chemokines enhance immunity by guiding naive CD8+ T cells to sites of CD4+ T cell-dendritic cell interaction. *Nature*. Apr 13 2006;440(7086):890-5. doi:10.1038/nature04651
197. Hickman HD, Li L, Reynoso GV, et al. Chemokines control naive CD8+ T cell selection of optimal lymph node antigen presenting cells. *J Exp Med*. Nov 21 2011;208(12):2511-24. doi:10.1084/jem.20102545
198. Hugues S, Scholer A, Boissonnas A, et al. Dynamic imaging of chemokine-dependent CD8+ T cell help for CD8+ T cell responses. *Nat Immunol*. Sep 2007;8(9):921-30. doi:10.1038/ni1495
199. Castellino F, Germain RN. Chemokine-guided CD4+ T cell help enhances generation of IL-6RalphahighIL-7Ralpha high prememory CD8+ T cells. *J Immunol*. Jan 15 2007;178(2):778-87. doi:10.4049/jimmunol.178.2.778
200. Hilligan KL, Ronchese F. Antigen presentation by dendritic cells and their instruction of CD4+ T helper cell responses. *Cell Mol Immunol*. Jun 2020;17(6):587-599. doi:10.1038/s41423-020-0465-0
201. Levin C, Bonduelle O, Nuttens C, et al. Critical Role for Skin-Derived Migratory DCs and Langerhans Cells in T. *J Invest Dermatol*. 09 2017;137(9):1905-1913. doi:10.1016/j.jid.2017.04.016
202. Kashem SW, Haniffa M, Kaplan DH. Antigen-Presenting Cells in the Skin. *Annu Rev Immunol*. 04 26 2017;35:469-499. doi:10.1146/annurev-immunol-051116-052215
203. Kedl RM, Lindsay RS, Finlon JM, Lucas ED, Friedman RS, Tamburini BAJ. Migratory dendritic cells acquire and present lymphatic endothelial cell-archived antigens during lymph node contraction. *Nat Commun*. Dec 11 2017;8(1):2034. doi:10.1038/s41467-017-02247-z
204. Tamburini BA, Burchill MA, Kedl RM. Antigen capture and archiving by lymphatic endothelial cells following vaccination or viral infection. *Nat Commun*. Jun 6 2014;5:3989. doi:10.1038/ncomms4989
205. Walsh SM, Sheridan RM, Lucas ED, et al. Molecular tracking devices quantify antigen distribution and archiving in the murine lymph node. *Elife*. Apr 12 2021;10doi:10.7554/eLife.62781
206. Pape KA, Catron DM, Itano AA, Jenkins MK. The humoral immune response is initiated in lymph nodes by B cells that acquire soluble antigen directly in the follicles. *Immunity*. Apr 2007;26(4):491-502. doi:10.1016/j.immuni.2007.02.011
207. Reynoso GV, Weisberg AS, Shannon JP, et al. Lymph node conduits transport virions for rapid T cell activation. *Nat Immunol*. 05 2019;20(5):602-612. doi:10.1038/s41590-019-0342-0
208. Acton SE, Onder L, Novkovic M, Martinez VG, Ludewig B. Communication, construction, and fluid control: lymphoid organ fibroblastic reticular cell and conduit networks. *Trends Immunol*. Sep 2021;42(9):782-794. doi:10.1016/j.it.2021.07.003
209. Gretz JE, Norbury CC, Anderson AO, Proudfoot AE, Shaw S. Lymph-borne chemokines and other low molecular weight molecules reach high endothelial venules via specialized conduits

while a functional barrier limits access to the lymphocyte microenvironments in lymph node cortex. *J Exp Med*. Nov 20 2000;192(10):1425-40. doi:10.1084/jem.192.10.1425
210. Rantakari P, Auvinen K, Jäppinen N, et al. The endothelial protein PLVAP in lymphatics controls the entry of lymphocytes and antigens into lymph nodes. *Nat Immunol*. Apr 2015;16(4):386-96. doi:10.1038/ni.3101
211. Sixt M, Kanazawa N, Selg M, et al. The conduit system transports soluble antigens from the afferent lymph to resident dendritic cells in the T cell area of the lymph node. *Immunity*. Jan 2005;22(1):19-29. doi:10.1016/j.immuni.2004.11.013
212. Baekkevold ES, Yamanaka T, Palframan RT, et al. The CCR7 ligand elc (CCL19) is transcytosed in high endothelial venules and mediates T cell recruitment. *J Exp Med*. May 7 2001;193(9):1105-12. doi:10.1084/jem.193.9.1105
213. Ohtani O, Ohtani Y, Carati CJ, Gannon BJ. Fluid and cellular pathways of rat lymph nodes in relation to lymphatic labyrinths and Aquaporin-1 expression. *Arch Histol Cytol*. Aug 2003;66(3):261-72. doi:10.1679/aohc.66.261
214. Baptista AP, Gola A, Huang Y, et al. The Chemoattractant Receptor Ebi2 Drives Intranodal Naive CD4. *Immunity*. 05 2019;50(5):1188-1201.e6. doi:10.1016/j.immuni.2019.04.001
215. Misslitz AC, Bonhagen K, Harbecke D, Lippuner C, Kamradt T, Aebischer T. Two waves of antigen-containing dendritic cells in vivo in experimental Leishmania major infection. *Eur J Immunol*. Mar 2004;34(3):715-725. doi:10.1002/eji.200324391
216. Tomura M, Hata A, Matsuoka S, et al. Tracking and quantification of dendritic cell migration and antigen trafficking between the skin and lymph nodes. *Sci Rep*. Aug 12 2014;4:6030. doi:10.1038/srep06030
217. Ballesteros-Tato A, Randall TD, Lund FE, Spolski R, Leonard WJ, León B. T Follicular Helper Cell Plasticity Shapes Pathogenic T Helper 2 Cell-Mediated Immunity to Inhaled House Dust Mite. *Immunity*. Feb 16 2016;44(2):259-73. doi:10.1016/j.immuni.2015.11.017
218. Perez-Shibayama C, Islander U, Lütge M, et al. Type I interferon signaling in fibroblastic reticular cells prevents exhaustive activation of antiviral CD8(+) T cells. *Sci Immunol*. Sep 11 2020;5(51)doi:10.1126/sciimmunol.abb7066
219. Chtanova T, Schaeffer M, Han SJ, et al. Dynamics of neutrophil migration in lymph nodes during infection. *Immunity*. Sep 19 2008;29(3):487-96. doi:10.1016/j.immuni.2008.07.012
220. Prat-Luri B, Neal C, Passelli K, et al. The C5a-C5aR1 complement axis is essential for neutrophil recruitment to draining lymph nodes via high endothelial venules in cutaneous leishmaniasis. *Cell Rep*. May 03 2022;39(5):110777. doi:10.1016/j.celrep.2022.110777
221. Huang JY, Lyons-Cohen MR, Gerner MY. Information flow in the spatiotemporal organization of immune responses. *Immunol Rev*. Mar 2022;306(1):93-107. doi:10.1111/imr.13046
222. Ugur M, Labios RJ, Fenton C, et al. Lymph node medulla regulates the spatiotemporal unfolding of resident dendritic cell networks. *Immunity*. Aug 08 2023;56(8):1778-1793.e10. doi:10.1016/j.immuni.2023.06.020
223. Andrews DM, Estcourt MJ, Andoniou CE, et al. Innate immunity defines the capacity of antiviral T cells to limit persistent infection. *J Exp Med*. Jun 07 2010;207(6):1333-43. doi:10.1084/jem.20091193
224. Yang CW, Strong BS, Miller MJ, Unanue ER. Neutrophils influence the level of antigen presentation during the immune response to protein antigens in adjuvants. *J Immunol*. Sep 01 2010;185(5):2927-34. doi:10.4049/jimmunol.1001289

225. Waggoner SN, Cornberg M, Selin LK, Welsh RM. Natural killer cells act as rheostats modulating antiviral T cells. *Nature*. Nov 20 2011;481(7381):394-8. doi:10.1038/nature10624
226. Yang CW, Unanue ER. Neutrophils control the magnitude and spread of the immune response in a thromboxane A2-mediated process. *J Exp Med*. Feb 11 2013;210(2):375-87. doi:10.1084/jem.20122183
227. Kamenyeva O, Boularan C, Kabat J, et al. Neutrophil recruitment to lymph nodes limits local humoral response to Staphylococcus aureus. *PLoS Pathog*. Apr 2015;11(4):e1004827. doi:10.1371/journal.ppat.1004827
228. Waggoner SN, Reighard SD, Gyurova IE, et al. Roles of natural killer cells in antiviral immunity. *Curr Opin Virol*. Feb 2016;16:15-23. doi:10.1016/j.coviro.2015.10.008
229. Sammicheli S, Kuka M, Di Lucia P, et al. Inflammatory monocytes hinder antiviral B cell responses. *Sci Immunol*. Oct 21 2016;1(4)doi:10.1126/sciimmunol.aah6789
230. Dasoveanu DC, Park HJ, Ly CL, et al. Lymph node stromal CCL2 limits antibody responses. *Sci Immunol*. Mar 20 2020;5(45)doi:10.1126/sciimmunol.aaw0693
231. McCarthy MK, Reynoso GV, Winkler ES, et al. MyD88-dependent influx of monocytes and neutrophils impairs lymph node B cell responses to chikungunya virus infection via Irf5, Nos2 and Nox2. *PLoS Pathog*. Jan 2020;16(1):e1008292. doi:10.1371/journal.ppat.1008292
232. Lok LSC, Clatworthy MR. Neutrophils in secondary lymphoid organs. *Immunology*. Dec 2021;164(4):677-688. doi:10.1111/imm.13406
233. Ali A, Canaday LM, Feldman HA, et al. Natural killer cell immunosuppressive function requires CXCR3-dependent redistribution within lymphoid tissues. *J Clin Invest*. Sep 15 2021;131(18)doi:10.1172/JCI146686
234. Biram A, Liu J, Hezroni H, et al. Bacterial infection disrupts established germinal center reactions through monocyte recruitment and impaired metabolic adaptation. *Immunity*. Mar 08 2022;55(3):442-458.e8. doi:10.1016/j.immuni.2022.01.013
235. Özcan A, Collado-Diaz V, Egholm C, et al. CCR7-guided neutrophil redirection to skin-draining lymph nodes regulates cutaneous inflammation and infection. *Sci Immunol*. Feb 04 2022;7(68):eabi9126. doi:10.1126/sciimmunol.abi9126
236. Potter EL, Gideon HP, Tkachev V, et al. Measurement of leukocyte trafficking kinetics in macaques by serial intravascular staining. *Sci Transl Med*. Jan 13 2021;13(576)doi:10.1126/scitranslmed.abb4582
237. Shanahan SL, Kunder N, Inaku C, et al. Longitudinal Intravascular Antibody Labeling Identified Regulatory T Cell Recruitment as a Therapeutic Target in a Mouse Model of Lung Cancer. *J Immunol*. Sep 15 2024;213(6):906-918. doi:10.4049/jimmunol.2400268
238. Fang V, Chaluvadi VS, Ramos-Perez WD, et al. Gradients of the signaling lipid S1P in lymph nodes position natural killer cells and regulate their interferon-γ response. *Nat Immunol*. Jan 2017;18(1):15-25. doi:10.1038/ni.3619
239. Lok LSC, Dennison TW, Mahbubani KM, Saeb-Parsy K, Chilvers ER, Clatworthy MR. Phenotypically distinct neutrophils patrol uninfected human and mouse lymph nodes. *Proc Natl Acad Sci U S A*. Sep 17 2019;116(38):19083-19089. doi:10.1073/pnas.1905054116
240. Bogoslowski A, Wijeyesinghe S, Lee WY, et al. Neutrophils Recirculate through Lymph Nodes to Survey Tissues for Pathogens. *J Immunol*. May 01 2020;204(9):2552-2561. doi:10.4049/jimmunol.2000022
241. Vollmann EH, Rattay K, Barreiro O, et al. Specialized transendothelial dendritic cells mediate thymic T-cell selection against blood-borne macromolecules. *Nat Commun*. Oct 28 2021;12(1):6230. doi:10.1038/s41467-021-26446-x

242. Wu Y, Huang JY, Conlon MT, et al. Distal Immunization and Systemic Cytokines Establish a Transient Immune Alert State in the Intestine. *J Immunol*. Jun 17 2024;doi:10.4049/jimmunol.2400209
243. Li W, Germain RN, Gerner MY. Multiplex, quantitative cellular analysis in large tissue volumes with clearing-enhanced 3D microscopy (C. *Proc Natl Acad Sci U S A*. Aug 29 2017;114(35):E7321-E7330. doi:10.1073/pnas.1708981114
244. Proebstl D, Voisin MB, Woodfin A, et al. Pericytes support neutrophil subendothelial cell crawling and breaching of venular walls in vivo. *J Exp Med*. Jun 04 2012;209(6):1219-34. doi:10.1084/jem.20111622
245. Hyun YM, Choe YH, Park SA, Kim M. LFA-1 (CD11a/CD18) and Mac-1 (CD11b/CD18) distinctly regulate neutrophil extravasation through hotspots I and II. *Exp Mol Med*. Apr 09 2019;51(4):1-13. doi:10.1038/s12276-019-0227-1
246. Choe K, Moon J, Lee SY, et al. Stepwise transmigration of T- and B cells through a perivascular channel in high endothelial venules. *Life Sci Alliance*. Aug 2021;4(8)doi:10.26508/lsa.202101086
247. Prizant H, Patil N, Negatu S, et al. $CXCL10^{+}$ peripheral activation niches couple preferred sites of Th1 entry with optimal APC encounter. *Cell Rep*. Aug 10 2021;36(6):109523. doi:10.1016/j.celrep.2021.109523
248. Satpathy AT, KC W, Albring JC, et al. Zbtb46 expression distinguishes classical dendritic cells and their committed progenitors from other immune lineages. *J Exp Med*. Jun 04 2012;209(6):1135-52. doi:10.1084/jem.20120030
249. Tittel AP, Heuser C, Ohliger C, et al. Functionally relevant neutrophilia in CD11c diphtheria toxin receptor transgenic mice. *Nat Methods*. Feb 26 2012;9(4):385-90. doi:10.1038/nmeth.1905
250. Jiao J, Dragomir AC, Kocabayoglu P, et al. Central role of conventional dendritic cells in regulation of bone marrow release and survival of neutrophils. *J Immunol*. Apr 01 2014;192(7):3374-82. doi:10.4049/jimmunol.1300237
251. Abtin A, Jain R, Mitchell AJ, et al. Perivascular macrophages mediate neutrophil recruitment during bacterial skin infection. *Nat Immunol*. Jan 2014;15(1):45-53. doi:10.1038/ni.2769
252. Kim ND, Luster AD. The role of tissue resident cells in neutrophil recruitment. *Trends Immunol*. Sep 2015;36(9):547-55. doi:10.1016/j.it.2015.07.007
253. De Giovanni M, Tam H, Valet C, Xu Y, Looney MR, Cyster JG. GPR35 promotes neutrophil recruitment in response to serotonin metabolite 5-HIAA. *Cell*. Mar 03 2022;185(5):815-830.e19. doi:10.1016/j.cell.2022.01.010
254. Webster B, Ekland EH, Agle LM, Chyou S, Ruggieri R, Lu TT. Regulation of lymph node vascular growth by dendritic cells. *J Exp Med*. Aug 07 2006;203(8):1903-13. doi:10.1084/jem.20052272
255. Tzeng TC, Chyou S, Tian S, et al. CD11c(hi) dendritic cells regulate the re-establishment of vascular quiescence and stabilization after immune stimulation of lymph nodes. *J Immunol*. Apr 15 2010;184(8):4247-57. doi:10.4049/jimmunol.0902914
256. Martín-Fontecha A, Thomsen LL, Brett S, et al. Induced recruitment of NK cells to lymph nodes provides IFN-gamma for T(H)1 priming. *Nat Immunol*. Dec 2004;5(12):1260-5. doi:10.1038/ni1138

257. Kang SJ, Liang HE, Reizis B, Locksley RM. Regulation of hierarchical clustering and activation of innate immune cells by dendritic cells. *Immunity*. Nov 14 2008;29(5):819-33. doi:10.1016/j.immuni.2008.09.017
258. Girbl T, Lenn T, Perez L, et al. Distinct Compartmentalization of the Chemokines CXCL1 and CXCL2 and the Atypical Receptor ACKR1 Determine Discrete Stages of Neutrophil Diapedesis. *Immunity*. Dec 18 2018;49(6):1062-1076.e6. doi:10.1016/j.immuni.2018.09.018
259. David BA, Kubes P. Exploring the complex role of chemokines and chemoattractants in vivo on leukocyte dynamics. *Immunol Rev*. May 2019;289(1):9-30. doi:10.1111/imr.12757
260. Rawat K, Tewari A, Li X, et al. CCL5-producing migratory dendritic cells guide CCR5+ monocytes into the draining lymph nodes. *J Exp Med*. Jun 05 2023;220(6)doi:10.1084/jem.20222129
261. Katakai T, Habiro K, Kinashi T. Dendritic cells regulate high-speed interstitial T cell migration in the lymph node via LFA-1/ICAM-1. *J Immunol*. Aug 01 2013;191(3):1188-99. doi:10.4049/jimmunol.1300739
262. Bajaña S, Turner S, Paul J, Ainsua-Enrich E, Kovats S. IRF4 and IRF8 Act in CD11c+ Cells To Regulate Terminal Differentiation of Lung Tissue Dendritic Cells. *J Immunol*. Feb 15 2016;196(4):1666-77. doi:10.4049/jimmunol.1501870
263. Hildner K, Edelson BT, Purtha WE, et al. Batf3 deficiency reveals a critical role for CD8alpha+ dendritic cells in cytotoxic T cell immunity. *Science*. Nov 14 2008;322(5904):1097-100. doi:10.1126/science.1164206
264. Del Fresno C, Saz-Leal P, Enamorado M, et al. DNGR-1 in dendritic cells limits tissue damage by dampening neutrophil recruitment. *Science*. Oct 19 2018;362(6412):351-356. doi:10.1126/science.aan8423
265. Gargaro M, Scalisi G, Manni G, et al. Indoleamine 2,3-dioxygenase 1 activation in mature cDC1 promotes tolerogenic education of inflammatory cDC2 via metabolic communication. *Immunity*. Jun 14 2022;55(6):1032-1050.e14. doi:10.1016/j.immuni.2022.05.013
266. Chang YH, Wang KC, Chu KL, et al. Dichotomous Expression of TNF Superfamily Ligands on Antigen-Presenting Cells Controls Post-priming Anti-viral CD4. *Immunity*. Nov 21 2017;47(5):943-958.e9. doi:10.1016/j.immuni.2017.10.014
267. Tewari A, Prabagar MG, Gibbings SL, Rawat K, Jakubzick CV. LN Monocytes Limit DC-Poly I:C Induced Cytotoxic T Cell Response. *Front Immunol*. 2021;12:763379. doi:10.3389/fimmu.2021.763379
268. Baeyens A, Bracero S, Chaluvadi VS, Khodadadi-Jamayran A, Cammer M, Schwab SR. Monocyte-derived S1P in the lymph node regulates immune responses. *Nature*. Apr 2021;592(7853):290-295. doi:10.1038/s41586-021-03227-6
269. Sun L, Zhang C, Jiao A, et al. $CCR2^{+}$ monocytes promote memory $CD8^{+}$ T-cell differentiation via membrane-bound TGF- β. *Cell Mol Immunol*. Aug 2025;22(8):869-888. doi:10.1038/s41423-025-01299-2
270. Ozga AJ, Chow MT, Lopes ME, et al. CXCL10 chemokine regulates heterogeneity of the $CD8^{+}$ T cell response and viral set point during chronic infection. *Immunity*. Jan 11 2022;55(1):82-97.e8. doi:10.1016/j.immuni.2021.11.002
271. Bangs DJ, Tsitsiklis A, Steier Z, et al. CXCR3 regulates stem and proliferative CD8+ T cells during chronic infection by promoting interactions with DCs in splenic bridging channels. *Cell Rep*. Jan 18 2022;38(3):110266. doi:10.1016/j.celrep.2021.110266

272. Garcia Z, Lemaître F, van Rooijen N, et al. Subcapsular sinus macrophages promote NK cell accumulation and activation in response to lymph-borne viral particles. *Blood*. Dec 06 2012;120(24):4744-50. doi:10.1182/blood-2012-02-408179
273. Coombes JL, Han SJ, van Rooijen N, Raulet DH, Robey EA. Infection-induced regulation of natural killer cells by macrophages and collagen at the lymph node subcapsular sinus. *Cell Rep*. Jul 26 2012;2(1):124-35. doi:10.1016/j.celrep.2012.06.001
274. Bajénoff M, Granjeaud S, Guerder S. The strategy of T cell antigen-presenting cell encounter in antigen-draining lymph nodes revealed by imaging of initial T cell activation. *J Exp Med*. Sep 01 2003;198(5):715-24. doi:10.1084/jem.20030167
275. Tatsumi N, Codrington AL, El-Fenej J, Phondge V, Kumamoto Y. Effective CD4 T cell priming requires repertoire scanning by CD301b. *Sci Immunol*. Dec 10 2021;6(66):eabg0336. doi:10.1126/sciimmunol.abg0336
276. Lyons-Cohen MR, Shamskhou EA, Gerner MY. Site-specific regulation of Th2 differentiation within lymph node microenvironments. *J Exp Med*. Apr 01 2024;221(4)doi:10.1084/jem.20231282
277. Willart MA, Jan de Heer H, Hammad H, et al. The lung vascular filter as a site of immune induction for T cell responses to large embolic antigen. *J Exp Med*. Nov 23 2009;206(12):2823-35. doi:10.1084/jem.20082401
278. Janela B, Patel AA, Lau MC, et al. A Subset of Type I Conventional Dendritic Cells Controls Cutaneous Bacterial Infections through VEGFα-Mediated Recruitment of Neutrophils. *Immunity*. Apr 16 2019;50(4):1069-1083.e8. doi:10.1016/j.immuni.2019.03.001
279. Scholer A, Hugues S, Boissonnas A, Fetler L, Amigorena S. Intercellular adhesion molecule-1-dependent stable interactions between T cells and dendritic cells determine CD8+ T cell memory. *Immunity*. Feb 2008;28(2):258-70. doi:10.1016/j.immuni.2007.12.016
280. Chow MT, Ozga AJ, Servis RL, et al. Intratumoral Activity of the CXCR3 Chemokine System Is Required for the Efficacy of Anti-PD-1 Therapy. *Immunity*. Jun 18 2019;50(6):1498-1512.e5. doi:10.1016/j.immuni.2019.04.010
281. Di Pilato M, Kfuri-Rubens R, Pruessmann JN, et al. CXCR6 positions cytotoxic T cells to receive critical survival signals in the tumor microenvironment. *Cell*. Aug 19 2021;184(17):4512-4530.e22. doi:10.1016/j.cell.2021.07.015
282. Meiser P, Knolle MA, Hirschberger A, et al. A distinct stimulatory cDC1 subpopulation amplifies $CD8^+$ T cell responses in tumors for protective anti-cancer immunity. *Cancer Cell*. Aug 14 2023;41(8):1498-1515.e10. doi:10.1016/j.ccell.2023.06.008
283. Sapoznikov A, Kozlovski S, Levi N, et al. Dendritic cell ICAM-1 strengthens synapses with CD8 T cells but is not required for their early differentiation. *Cell Rep*. Aug 29 2023;42(8):112864. doi:10.1016/j.celrep.2023.112864
284. Lim K, Kim TH, Trzeciak A, et al. In situ neutrophil efferocytosis shapes T cell immunity to influenza infection. *Nat Immunol*. Sep 2020;21(9):1046-1057. doi:10.1038/s41590-020-0746-x
285. Espinosa V, Dutta O, Heung LJ, et al. Cutting Edge: Neutrophils License the Maturation of Monocytes into Effective Antifungal Effectors. *J Immunol*. Nov 15 2022;209(10):1827-1831. doi:10.4049/jimmunol.2200430
286. Bardou M, Postat J, Loaec C, et al. Quorum sensing governs collective dendritic cell activation in vivo. *Embo j*. Aug 2 2021;40(15):e107176. doi:10.15252/embj.2020107176
287. Simmons S, Sasaki N, Umemoto E, et al. High-endothelial cell-derived S1P regulates dendritic cell localization and vascular integrity in the lymph node. *Elife*. Oct 01 2019;8doi:10.7554/eLife.41239

288. Segel GB, Halterman MW, Lichtman MA. The paradox of the neutrophil's role in tissue injury. *J Leukoc Biol*. Mar 2011;89(3):359-72. doi:10.1189/jlb.0910538
289. Brandes M, Klauschen F, Kuchen S, Germain RN. A systems analysis identifies a feedforward inflammatory circuit leading to lethal influenza infection. *Cell*. Jul 03 2013;154(1):197-212. doi:10.1016/j.cell.2013.06.013
290. Uderhardt S, Martins AJ, Tsang JS, Lämmermann T, Germain RN. Resident Macrophages Cloak Tissue Microlesions to Prevent Neutrophil-Driven Inflammatory Damage. *Cell*. Apr 18 2019;177(3):541-555.e17. doi:10.1016/j.cell.2019.02.028
291. Aroca-Crevillén A, Vicanolo T, Ovadia S, Hidalgo A. Neutrophils in Physiology and Pathology. *Annu Rev Pathol*. Jan 24 2024;19:227-259. doi:10.1146/annurev-pathmechdis-051222-015009
292. Fonseca DM, Hand TW, Han SJ, et al. Microbiota-Dependent Sequelae of Acute Infection Compromise Tissue-Specific Immunity. *Cell*. Oct 08 2015;163(2):354-66. doi:10.1016/j.cell.2015.08.030
293. McCarthy MK, Davenport BJ, Reynoso GV, et al. Chikungunya virus impairs draining lymph node function by inhibiting HEV-mediated lymphocyte recruitment. *JCI Insight*. Jul 12 2018;3(13)doi:10.1172/jci.insight.121100
294. Mazzoni A, Bronte V, Visintin A, et al. Myeloid suppressor lines inhibit T cell responses by an NO-dependent mechanism. *J Immunol*. Jan 15 2002;168(2):689-95. doi:10.4049/jimmunol.168.2.689
295. Giordano D, Li C, Suthar MS, et al. Nitric oxide controls an inflammatory-like Ly6C(hi)PDCA1+ DC subset that regulates Th1 immune responses. *J Leukoc Biol*. Mar 2011;89(3):443-55. doi:10.1189/jlb.0610329
296. Lukacs-Kornek V, Malhotra D, Fletcher AL, et al. Regulated release of nitric oxide by nonhematopoietic stroma controls expansion of the activated T cell pool in lymph nodes. *Nat Immunol*. Sep 18 2011;12(11):1096-104. doi:10.1038/ni.2112
297. Hernansanz-Agustín P, Izquierdo-Álvarez A, García-Ortiz A, Ibiza S, Serrador JM, Martínez-Ruiz A. Nitrosothiols in the immune system: signaling and protection. *Antioxid Redox Signal*. Jan 20 2013;18(3):288-308. doi:10.1089/ars.2012.4765
298. Giordano D, Draves KE, Li C, Hohl TM, Clark EA. Nitric oxide regulates BAFF expression and T cell-independent antibody responses. *J Immunol*. Aug 01 2014;193(3):1110-20. doi:10.4049/jimmunol.1303158
299. Baratin M, Simon L, Jorquera A, et al. T Cell Zone Resident Macrophages Silently Dispose of Apoptotic Cells in the Lymph Node. *Immunity*. Aug 15 2017;47(2):349-362.e5. doi:10.1016/j.immuni.2017.07.019
300. Koup RA, Douek DC. Vaccine design for CD8 T lymphocyte responses. *Cold Spring Harb Perspect Med*. Sep 2011;1(1):a007252. doi:10.1101/cshperspect.a007252
301. Pennock ND, Kedl JD, Kedl RM. T Cell Vaccinology: Beyond the Reflection of Infectious Responses. *Trends Immunol*. Mar 2016;37(3):170-180. doi:10.1016/j.it.2016.01.001
302. Irvine DJ, Aung A, Silva M. Controlling timing and location in vaccines. *Adv Drug Deliv Rev*. 2020;158:91-115. doi:10.1016/j.addr.2020.06.019
303. Kastenmüller K, Wille-Reece U, Lindsay RW, et al. Protective T cell immunity in mice following protein-TLR7/8 agonist-conjugate immunization requires aggregation, type I IFN, and multiple DC subsets. *J Clin Invest*. May 2011;121(5):1782-96. doi:10.1172/jci45416

304. Lynn GM, Laga R, Darrah PA, et al. In vivo characterization of the physicochemical properties of polymer-linked TLR agonists that enhance vaccine immunogenicity. *Nat Biotechnol*. Nov 2015;33(11):1201-10. doi:10.1038/nbt.3371
305. Baharom F, Ramirez-Valdez RA, Tobin KKS, et al. Intravenous nanoparticle vaccination generates stem-like TCF1(+) neoantigen-specific CD8(+) T cells. *Nat Immunol*. Jan 2021;22(1):41-52. doi:10.1038/s41590-020-00810-3
306. Darrah PA, Zeppa JJ, Maiello P, et al. Prevention of tuberculosis in macaques after intravenous BCG immunization. *Nature*. Jan 2020;577(7788):95-102. doi:10.1038/s41586-019-1817-8